

Helsinki University of Technology
Department of Mechanical Engineering
Laboratory of Engineering Materials

**EFFECTS OF NON-METALLIC INCLUSIONS
ON
FATIGUE PROPERTIES
OF
CALCIUM TREATED STEELS**

Pekko Juvonen

Dissertation for the degree of Doctor of Science in Technology to be presented with due permission for public examination and debate in Micronova (Large seminar room) at Helsinki University of Technology (Espoo, Finland) on the 10th of December, 2004, at 12 o'clock noon.

Espoo 2004

Distribution:

Helsinki University of Technology
Laboratory of Engineering Materials
P.O.Box 4200
FIN-02015 HUT

ISBN 951-22-7422-1 (print)

ISBN 951-22-7423-X (pdf, available at <http://lib.hut.fi/Diss/2004/isbn951227423X>)

ISSN 1456-3576

Otamedia Oy

Espoo 2004

JUVONEN, Pekko. **Effects of Non-metallic Inclusions on Fatigue Properties of Calcium Treated Steels**. Espoo 2004, Helsinki University of Technology.

Keywords: fatigue strength, nonmetallic inclusions, calcium treated steel, statistical analysis, statistics of extremes, ultrasonic testing, machinability

ABSTRACT

Fatigue behaviour of 22 industrial test charges of AISI 8620 carburizing steel with two different calcium treatment levels was studied. The research work consisted mainly of rotating bending fatigue tests, residual stress and surface roughness measurements, electron microscopy, different steel cleanliness level and statistical inclusion size estimation methods.

There were no significant differences between the σ_w/R_m ratios of the casts with the large amount of calcium injection and the casts with the small amount of calcium injection. In the casts with the large amount of calcium injection, the fatigue cracks initiated mostly from the surface and interior inclusions. In the casts with the small amount of calcium injection, the fatigue cracks initiated mostly from the surface discontinuities. The inclusions responsible for fatigue crack initiation were in the most cases calcium aluminates encapsulated in calcium sulfide containing small amounts of magnesia and/or silica. The fatigue crack initiation from cracked and non-cracked inclusions resulted in similar fatigue life on the same ΔK level. The fatigue strength scatter was larger in the casts with the large amount of calcium injection. In rotating bending fatigue the σ_w/R_m ratio was almost independent of inclusion size in the average fatigue crack initiating inclusion size region smaller than $\sim 70\text{-}90\ \mu\text{m}$.

The results of DIN 50 602 and SFS-ENV 10247 inclusion rating methods and ultrasonic tests in immersion did not correlate with the inclusions that were responsible for fatigue failure in these steels. The results may, however, suggest guidelines for the fatigue properties and the machinability of these steels when the contents of certain alloying elements are taken into account. Ultrasonic tests in immersion provide more relevant information about the fatigue properties and machinability of these steels than the conventional inclusion rating methods do, but its resolution capability still needs improvement.

In most casts the maximum inclusion sizes predicted by the statistics of extreme value method were much smaller than the size of the inclusions found at the fatigue crack initiation sites of the fatigue specimens. The studied steels seemed to have two different inclusion size distributions, i.e., the inclusions detected at the polished microsections and the inclusions at the fatigue crack initiation sites. Both distributions had similar morphology and chemical composition, which was contrary to the earlier findings of the bilinear nature of inclusion distribution in some steels. The successful application of the Murakami-Endo model with these steels requires quite a large inspection area, approximately $8400\ \text{mm}^2$ at least, to enable the detection of the population of the largest inclusions, which are responsible for fatigue failure.

PREFACE

The research work presented in this thesis was accomplished during The Graduate School of Metallurgy financed by the Finnish Academy. The financial support of Imatra Steel Oy Ab, Research Foundation of Helsinki University of Technology and the Walter Ahlström Foundation are also gratefully acknowledged.

I wish to express my gratitude to the supervisor of my thesis, professor Hannu Hänninen, for his patient guidance and advice. Dr. Tech. Vesa Ollilainen from Imatra Steel Oy Ab I would like to thank for providing me motivation to finish this thesis. I would also like to thank Mr. Ari Anonen from Imatra Steel Oy Ab for providing me necessary information concerning the experimental part of this thesis and Mrs. Lotta Ruottinen from Imatra Steel Oy Ab for the ultrasonic testing in immersion. I am also grateful for everyone at Imatra steel plant whose work contribution assisted me in this thesis, as well as for the whole personnel of the Laboratory of Engineering Materials for offering help in this work when needed.

I especially want to thank my dear Anissa for her patience and support.

Otaniemi, February 2004

Pekko Juvonen

CONTENTS

ABSTRACT	2
PREFACE	3
CONTENTS	4
LIST OF SYMBOLS	6
ORIGINAL FEATURES	9
1 INTRODUCTION	10
1.1 Inclusions in steels	10
1.2 Calcium treated steels	11
1.3 Steel cleanliness level estimation methods	12
1.4 Inclusion properties affecting fatigue properties	12
1.5 Fatigue crack initiation and crack growth	17
1.6 Stress concentration and fatigue notch effect	19
1.7 Non-propagating cracks	24
1.8 Small crack growth	26
1.9 Size effect	29
1.10 Models describing the effects of defects on fatigue strength	30
1.11 Murakami-Endo model	34
2 AIMS OF THE STUDY	39
3 EXPERIMENTAL METHODS	40
3.1 Materials	40
3.2 Fatigue tests	42
3.3 Residual stress measurements	44
3.4 Surface roughness measurements	45
3.5 Inclusion analyses	46
3.6 Ultrasonic testing in immersion	47
3.7 SEM and EDS investigations	47
3.8 Statistics of extreme value evaluation and application of the Murakami-Endo model	48
4 RESULTS	49
4.1 Fatigue tests	49
4.2 Residual stress measurements	50
4.3 Surface roughness measurements	51
4.4 Inclusion analyses	53
4.5 Ultrasonic testing in immersion	54
4.6 SEM and EDS investigations	56
4.7 Statistics of extreme value evaluation and application of the Murakami-Endo model	62
4.8 Multiple linear regression	67
5 DISCUSSION	70
5.1 Fatigue tests	70

5.2	Residual stress measurements	72
5.3	Surface roughness measurements	73
5.4	Inclusion analyses	73
5.5	Ultrasonic testing in immersion	74
5.6	SEM and EDS investigations.....	76
5.7	Statistics of extreme value evaluation and application of the Murakami-Endo model	81
6	CONCLUSIONS	82
	REFERENCES	84
	APPENDIX 1. Fatigue test graphs	91
	APPENDIX 2. Fatigue crack initiating inclusion data	94
	APPENDIX 3. Statistics of extreme value graphs	97
	APPENDIX 4. Lower and upper bound estimate graphs for the fatigue strength 100	

LIST OF SYMBOLS

a	Depth or half of the length of a crack
a ₁	Threshold value for crack size in the Kitagawa-Takahashi diagram
a ₂	Threshold value for crack size in the Kitagawa-Takahashi diagram
A	Elongation to fracture (%)
\sqrt{area}	Parameter expressing the defect dimension (μm)
$\sqrt{area_{max}}$	Parameter expressing the maximum defect dimension (μm)
$\sqrt{area_{init.}}$	Parameter expressing the inclusion dimension in fracture surface (μm)
$\sqrt{area_{init.max}}$	Parameter expressing the maximum inclusion dimension in fracture surface (μm)
$\sqrt{area_{init.mean}}$	Parameter expressing the mean inclusion dimension in fracture surface (μm)
$\sqrt{area_1}$	Size parameter for surface inclusions (μm)
$\sqrt{area_2}$	Size parameter for surface inclusions (μm)
$\sqrt{area_R}$	Equivalent defect size for surface roughness (μm)
2b	Pitch of a surface roughness profile (μm)
C	Inclusion location dependent constant for the Murakami-Endo model
C'	Material constant for Peterson's equation
C _F	Constant for the Frost model
C _{KN}	Constant for the Kobayashi-Nakazawa model
C _{ME}	Constant for the Murakami-Endo model
C _P	Parameter for the Paris law
E	Young's modulus (GPa)
F	Cumulative distribution function
GPD	Generalized Pareto distribution
h	Distance of a fatigue crack initiating inclusion from the specimen surface (μm)
h ₀	Estimated thickness of the standard control volume (μm)
h _s	Control depth for prospective fatigue failure (μm)
k _f	Fatigue notch factor
k _t	Stress concentration factor
K	Stress intensity factor ($\text{MPa}\sqrt{m}$)
K _I	Stress intensity factor for Mode I loading ($\text{MPa}\sqrt{m}$)
K _{max}	Maximum value of stress intensity factor ($\text{MPa}\sqrt{m}$)
K _{min}	Minimum value of stress intensity factor ($\text{MPa}\sqrt{m}$)
K _{I,max}	Maximum value of stress intensity factor, mode I ($\text{MPa}\sqrt{m}$)
K _{op}	Opening level of stress intensity factor ($\text{MPa}\sqrt{m}$)
ΔK	Stress intensity factor range, K _{max} -K _{min} ($\text{MPa}\sqrt{m}$)
ΔK_{th}	Threshold stress intensity factor range ($\text{MPa}\sqrt{m}$)
$\Delta K_{th lc}$	Threshold stress intensity factor range for long cracks ($\text{MPa}\sqrt{m}$)
$\Delta K_{th sc}$	Threshold stress intensity factor range for small cracks ($\text{MPa}\sqrt{m}$)
ΔK_{eff}	Effective stress intensity factor range ($\text{MPa}\sqrt{m}$)

l	Depth or half of the length of a crack
m	Parameter for the Paris law
n	Number of standard inspection areas in the SEV procedure
N	Number of cycles
N_f	Number of cycles to failure
p	Characteristic material parameter for Peterson's equation
q	Notch sensitivity factor
r	Distance from the crack tip
R	Stress ratio, $\sigma_{\min}/\sigma_{\max}$
$R_{p0,2}$	Yield strength (MPa)
R_m	Ultimate tensile strength (MPa)
R_a	Average surface roughness (μm)
R_z	Surface roughness parameter; mean peak-to-valley height (μm)
R_{\max}	Surface roughness parameter; maximum individual peak-to-valley height (μm)
S	Area of prediction (mm^2)
S_0	Standard inspection area (mm^2)
S_{crit}	Critical value of standard inspection area (mm^2)
SEV	Statistics of extreme value
T	Return period
V	Volume of prediction (mm^3)
V_0	Standard control volume (mm^3)
V_s	Control volume for prospective fatigue failure (mm^3)
v_{15}	Cutting speed corresponding to a tool life of 15 min (m/min)
y	Reduced variate of the statistics of extreme distribution
Z	Reduction of area (%)
α	Coefficient of thermal expansion ($1/^\circ\text{C}$)
α_{ME}	Parameter for the Murakami-Endo model
χ	Nondimensional stress gradient
δ	Scale parameter of the statistics of extreme distribution
ε_0	Distance from the notch root in the Isibasi model
λ	Location parameter of the statistics of extreme distribution
ν	Poisson's ratio
ρ	Notch root radius
σ	Stress (MPa)
σ'	Stress at inclusion (MPa)
σ_m	Mean stress (MPa)
σ_{\max}	Maximum stress (MPa)
σ_{\min}	Minimum stress (MPa)
σ_{res}	Residual stress (MPa)
σ_t	Residual stress component tangential to the specimen axis (MPa)
σ_U	Ultimate tensile strength (MPa)
σ_w	Fatigue limit (MPa)
σ_w'	Estimated fatigue limit (MPa)
σ_{w0}	Fatigue strength of an unnotched specimen, i.e., ideal fatigue strength (MPa)
σ_{wi}	Critical stress for fatigue crack initiation (MPa)

σ_{wl}	Lower bound of fatigue limit (MPa)
σ_{wU}	Upper bound of fatigue limit (MPa)
σ_x	Residual stress component longitudinal to the specimen axis (MPa)
σ_{x0}	Uniaxial remote tensile stress in the x-direction (MPa)
σ_θ	Tangential stress (MPa)

ORIGINAL FEATURES

The experimental data and analyses of this thesis describe the effects of calcium treatment on the properties of a carburizing steel. The following features and observations are believed to be original in this thesis:

1. The fatigue properties of AISI 8620 carburizing steel were studied on two different calcium treatment levels with a large number of industrial test charges.
2. There were no significant differences between the values of the σ_w/R_m ratio of the casts with the large amount of calcium injection and the casts with the small amount of calcium injection. On average fatigue crack initiating inclusion sizes smaller than $\sim 70\text{-}90\ \mu\text{m}$ the σ_w/R_m ratio in rotating bending fatigue appeared almost independent of inclusion size. The fatigue strength scatter was larger in the casts with the large amount of calcium injection.
3. On both calcium treatment levels, inclusions, which were mainly calcium aluminates encapsulated in calcium sulfide containing small amounts of magnesia and/or silica, caused fatigue crack initiation. In the casts with the small amount of calcium injection, fatigue cracks initiated mostly from the surface discontinuities.
4. There was no good correlation between either DIN 50 602 and SFS-ENV 10247 inclusion rating methods or ultrasonic testing in immersion and inclusions that are responsible for fatigue failure in these steels. The results of the inclusion analysis methods combined with certain alloying elements, especially calcium, oxygen, sulfur and insoluble aluminium, however, showed statistically significant correlation with v_{15} and the σ_w/R_m ratio despite the small variance between the casts. Ultrasonic testing in immersion provides more relevant information about the fatigue properties and machinability of these steels than the conventional inclusion rating methods do, but its resolution capability needs improvement.
5. On the same ΔK level the fatigue crack initiation both from cracked and non-cracked inclusions resulted in similar fatigue life. Fatigue crack initiation took place at the cracked calcium aluminates with irregular shapes at lower ΔK levels than in the case of cracked calcium aluminates with globular shapes. However, no difference between the fatigue lives of the two cases was observed at the same ΔK levels.
6. The studied steels seemed to have two different inclusion size distributions, which, however, contrary to the earlier findings of the bilinear nature of inclusion distributions in some steels, had similar morphology and chemical composition. Application of the Murakami-Endo model with these steels requires a larger standard inspection area, approximately $8400\ \text{mm}^2$ at least, to enable the detection of the population of the largest inclusions, which are responsible for fatigue failure. The casts with the small amount of calcium injection require larger inspection areas.

1 INTRODUCTION

In steels there always exists a large number of inclusions which can have a degrading effect on their fatigue properties. Inclusions do not only cause a reduction in fatigue strength of steels but also a considerable scatter in the fatigue data. The presence of large non-metallic inclusions and pores etc. especially caused considerable scatter in fatigue data of steels in the early fatigue studies when steelmaking technology was not as advanced as it is nowadays. The degrading effect of the inclusions on the fatigue strength is pronounced on hard steels and proportional to the strength level of the steel. Correlations between various inclusion rating methods which are used in several countries and fatigue strength have been investigated, but the results have not always been satisfactory (e.g., Monnot et al., 1988).

Non-metallic inclusions can have a beneficial effect on the machinability of steel (Kießling, 1978). In calcium treated steels the shape and composition of non-metallic inclusions (oxides and sulphides) are modified to improve machinability. Inclusion size itself does not have any significant effect on machinability as it does on degradation of fatigue strength but the quantity of inclusions is important. Thus, the preferred inclusion size distribution and quantity combination in calcium treated steels is a large number of small inclusions.

Nowadays, when the steel industry is manufacturing cleaner and cleaner steels, the inclusion problem is generally associated with the high strength steels. The effect of inclusions on fatigue strength of high strength steels can be estimated with quantitative statistical methods. However, inclusions in calcium treated steels and inclusions of external origin may cause problems with fatigue also in steels with a lower strength level. The applicability of the quantitative statistical methods to steels with lower strength levels is not clear, yet.

1.1 Inclusions in steels

Non-metallic inclusions in steels can be divided into two groups, those of indigenous and those of exogenous origin. The former group contains inclusions occurring as a result of the reactions taking place in the molten or solidifying steel, whereas the latter contains the inclusions resulting from mechanical incorporation of slags, refractories or other materials with which the molten steel comes into contact (Kießling, 1978). Exogenous inclusions are usually larger than the indigenous inclusions and, thus, non-metallic inclusions can also be divided into microinclusions and macroinclusions. Macroinclusions are more detrimental when their effects on the properties of steel, and especially fatigue properties, are considered (e.g., Cheng et al., 2003).

With the concept "clean steel" a steel with a low number of inclusions is usually meant. The development of the steelmaking methods has over the years decreased the undesirable elements in steel. Normally these undesirable elements are oxygen,

sulphur, phosphorus and hydrogen. Oxygen and sulphur are present as oxides and sulphides in steel and attempts on steel cleanliness level improvements have usually concentrated on the methods to decrease the levels of oxygen and sulphur. The oxygen content of the steel should be as low as possible because low oxygen content decreases the probability of large oxide inclusions which are always unwanted (Kiessling, 1980). However, low oxygen content is not necessarily related to high fatigue strength if also the size of oxides is not decreased concurrently. The oxygen and sulphur contents give a useful but not full characterization of the steel cleanliness.

1.2 Calcium treated steels

The use of calcium alloys in steel production dates back to the period 1950-60 (Kiessling, 1989). Calcium is a strong deoxidizer and desulphurizer in steels. Calcium treatment can be used for steels to lower the sulfur and oxygen contents as well as to lower the number of inclusions and to modify the inclusion morphology (e.g., Wilson, 1982; Kiessling, 1989, Saleil et al., 1989). Calcium treatment modifies oxide and sulfide inclusion chemistry and morphology so that elongated inclusions become globular. Aluminum oxides, which normally are hard and angular and very detrimental to machinability, and often appear in clusters, are reduced in number or completely eliminated being replaced by complex CaO-Al₂O₃ or CaO-Al₂O₃-SiO₂ inclusions. Also silicates are eliminated and replaced by CaO-Al₂O₃-SiO₂ inclusions. According to Kiessling (1978), inclusions which form a protective layer on the cutting tool, e.g., manganese sulfides and calcium aluminates surrounded by a sulfide shell, are beneficial to the machinability of the steel. It is also noteworthy that the duplex inclusions, i.e., calcium aluminates surrounded by a sulfide shell, unlike manganese sulfides, do not deform during hot rolling and during machining their deformability is also poor, but they still form a protective layer on the cutting tool, i.e., a good deformability of inclusions is not a prerequisite for their ability to protective layer formation during machining as it was commonly believed earlier (Helle et al., 1993).

The result of a calcium treatment depends not only on the amount of calcium injected but also on the amounts of oxygen, sulfur and aluminum in the steel. Unlike in clean steels, in calcium treated steels with improved machinability the oxygen content has to be above a certain value, since otherwise the calcium treatment will not be successful. For improved machinability also a certain minimum sulfur content is required and for improved mechanical properties the sulfur content needs to be lower than a certain allowed maximum value. As the sulfur content increases, the size and number of inclusions in the steel tends to increase (Hetzner & Pint, 1988) resulting, thus, usually in improved machinability but impaired transverse mechanical properties (Pickett et al., 1985). Lu et al. (1994) reported of a considerable enhancement in calcium absorption by higher sulphur and oxygen contents in steel. The average inclusion size has been reported to increase in the calcium treated steels as a result of coagulation of the smaller inclusions into bigger ones opposite to untreated steels (e.g., Meredith & Moore,

1981; Carlsson & Helle, 1985). Generally, the occurrence of large globular inclusions in a calcium treated steel is considered as the result of an uncontrolled calcium treatment (Gustafsson et al., 1981).

Duplex inclusions containing calcium and aluminium, such as $\text{CaO}(\text{Al}_2\text{O}_3)$ and $\text{CaO}(\text{Al}_2\text{O}_3(2\text{SiO}_2))$ are thought to be most detrimental to the fatigue strength and the reason for this is mainly because they are much larger in size than oxide inclusions, e.g., Al_2O_3 , and titanium nitrides (Cogne et al., 1987; Lund & Akesson, 1988). On the other hand, calcium treatment can eliminate the anisotropic fatigue properties of wrought steels, i.e., poor fatigue properties in transverse direction resulting from elongated sulfide inclusions. According to Collins & Michal (1995) the calcium treatment enhanced the transverse fatigue properties of an AISI 4140 steel and the enhancement was due to the inclusion shape control.

1.3 Steel cleanliness level estimation methods

Various inclusion rating methods have been proposed and used in many countries but these methods most often do not show any sound correlation with the fatigue strength of the steel. Monnot et al. (1988) pointed out that conventional inclusion cleanliness rating methods do not have scientific proof, and that steels with high cleanliness rating results may have even lower fatigue strengths than those of steels with lower cleanliness rating results. One reason for this non-correlation is that these inclusion rating methods usually take into account also the small inclusions which do not necessarily have any effect on the fatigue properties of the steel. Fatigue and fatigue crack initiation are so-called weakest link phenomena, i.e., the fatigue crack usually initiates from the largest defect in the whole material volume (e.g., Murakami & Usuki, 1989; Murakami et al., 1994). The inclusion distribution determined from material areas examined by conventional inclusion rating methods does not necessarily relate to the fatigue strength as, for example, inclusions appearing at the fatigue crack initiation sites in the fatigue test specimens do. Inclusions are not evenly distributed within the steel and therefore it is also possible that quite different results may be obtained from the samples of the same steel charge, ingot or even billet, caused by differences in inclusion concentration and type in the different parts of the ingot. The inspection areas or volumes used in the traditional inclusion rating methods are also usually much smaller than the material volume in real components where fatigue failure may take place, i.e., the inspection area may not give the right picture of the inclusion distribution in the material, because the largest inclusions in the steel are not sufficiently taken into consideration.

1.4 Inclusion properties affecting fatigue properties

The effect of an inclusion on the fatigue properties depends on its size, shape, thermal and elastic properties and its adhesion to the matrix. These factors are

related to the stress concentration factor and the stress distribution around the inclusion. Inclusion size has the major effect on the fatigue strength. Other inclusion properties affecting the stress concentration factor may influence the critical stress for fatigue crack initiation and, thus, fatigue life, but they are not the major factors when fatigue limit is considered. The relative harmfulness of the various types of inclusions on fatigue life according to Cogne et al. (1987) is presented in Figure 1.

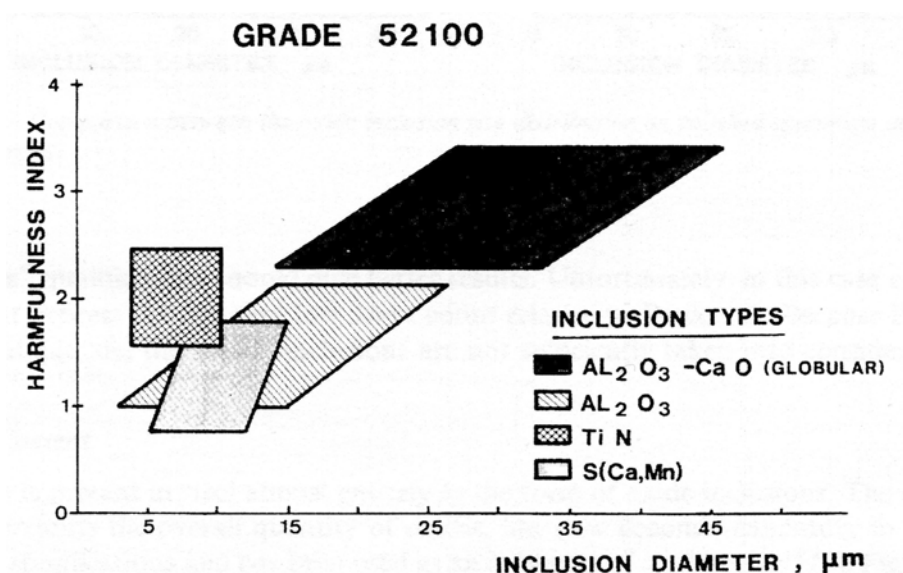


Figure 1. Relative harmfulness of various types of inclusions on fatigue life of a bearing steel (Cogne et al., 1987).

Inclusion size

Inclusion size has the major effect on the fatigue properties. The distribution of inclusions in metals is expected to be nearly exponential (Murakami et al., 1994). Over the years of fatigue research attempts have been made to determine the critical inclusion size under which inclusions do not have an effect on the fatigue strength. Critical inclusion size is dependent on the strength and hardness of the material. In the investigations of Duckworth & Ineson (1963), where artificially introduced Al_2O_3 inclusions were used, the critical inclusion size for an inclusion located just below the surface was found to be $10 \mu m$. In the investigations of Nishijima et al. (1984) on standard Japanese tempered martensitic steels in the tensile strength range of 700-1300 MPa from several different companies it was statistically analyzed that the critical size of inclusions was $\sim 45 \mu m$ in the rotating bending fatigue tests. It has to be noted, that in the investigations of Nishijima et al. (1984) also inclusions smaller than $45 \mu m$ caused fatigue fracture, but only in the steels which had inclusions larger than that there was a decrease in the values of the relationship between the fatigue strength and the material hardness. Melander & Ölund (1999) reported that Ti(C,N) inclusions and alumina inclusions as small as $3 \mu m$ and $17 \mu m$ in size, respectively, were found on the fracture surfaces of rotating bending fatigue test specimens of bearing steels. It was also

concluded that Ti(C,N) inclusions were as detrimental to fatigue life as oxide inclusions of approximately three times their size.

Inclusion shape

Inclusions with an irregular shape and sharp edges cause larger stress concentrations around the inclusions than inclusions with a smooth shape which make it easier for a fatigue crack to initiate. For example, TiN-inclusions having a sharp angular shape cause earlier crack initiation than the globular inclusions which have the same size resulting, thus, in the lower fatigue life at a stress level higher than the fatigue limit, see Figure 1.

Thermal properties

Differences in the thermal expansion coefficients of the inclusion and the matrix can generate internal stresses around inclusions. During the hot rolling of the steel the stresses between inclusions and the steel matrix are relaxed. During the cooling that follows the hot rolling, tensile residual stresses are generated around an inclusion, i.e., tessellated stresses, if the coefficient of thermal expansion of an inclusion is smaller than the coefficient of thermal expansion of the matrix. When the coefficient of thermal expansion of an inclusion is larger than that of the matrix, e.g., for MnS and CaS, detrimental tensile residual stresses are not generated. A generally accepted view is that the oxide inclusions are detrimental because they cause tensile residual stresses, and the sulfide inclusions, such as MnS, are not detrimental, or are perhaps useful. According to Kiessling (1989), calcium aluminates are most dangerous, especially in rolling contact fatigue. However, in the duplex inclusions, i.e., oxide inclusions surrounded by sulfide shells, the sulfide shell which has a larger coefficient of thermal expansion than that of the oxide may compensate for the detrimental residual stresses resulting from the oxide part of the duplex inclusion. In Figure 2 the tendency for forming internal stresses around the inclusions due to differences in the coefficients of thermal expansion of the inclusion and the matrix is presented for different inclusion types in a bearing steel (Brooksbank & Andrews, 1972).

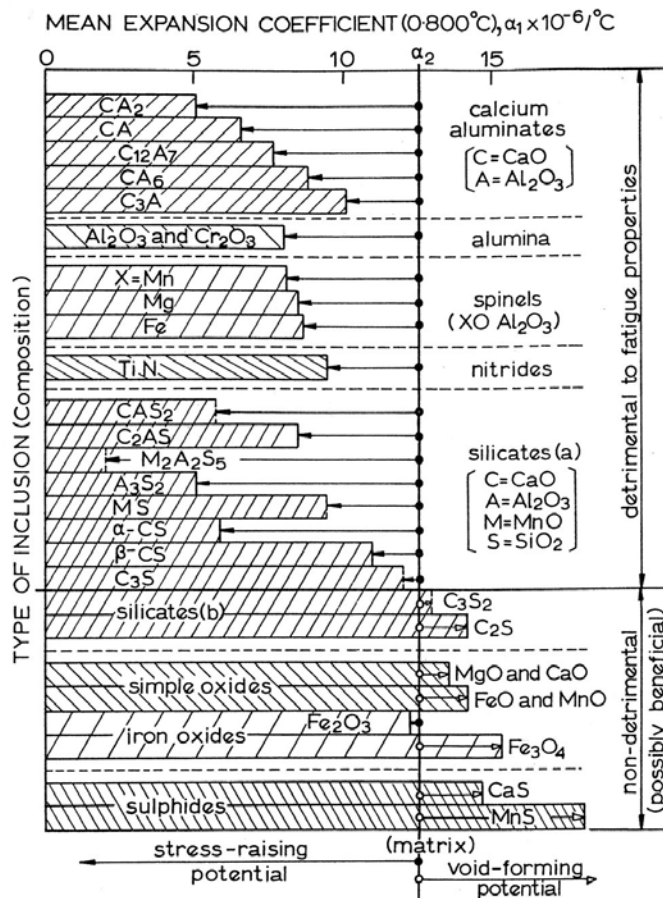


Figure 2. Stress-raising properties of various inclusion types in 1% C-Cr-bearing steel (Brooksbank & Andrews, 1972).

It can be seen in Figure 2 that sulfides give rise to voids at the interface between inclusion and matrix, whereas most oxides cause dilatational stresses. These stresses may greatly alter the properties of the matrix and localized yielding may occur.

Elastic properties

When the Young's modulus of an inclusion is greater than the Young's modulus of the matrix, e.g., for TiC, Al₂O₃ and calcium aluminates, a stress concentration is generated around the inclusion under a tensile stress. Young's modulus of the sulfides is usually lower than that of the matrix which makes sulfides relatively harmless. Hard inclusions with low deformability may cause microcrack formation at the interface between the inclusion and the matrix when the steel is hot rolled, which may make it possible for a fatigue crack to initiate from these microcracks. Thermal and elastic properties of various inclusion types are presented in Table 1 (Brooksbank & Andrews, 1968; 1969; 1972; Brooksbank, 1970).

Table 1. Values of coefficients of thermal expansion, α , Young's modulus, E, and Poisson's ratio, ν , for various inclusion types (Brooksbank & Andrews, 1968; 1969; 1972; Brooksbank, 1970).

Inclusion type	Inclusion	$\alpha \times 10^{-6}/^{\circ}\text{C}$ (0 ~ 800 °C)	E (GPa)	ν
Sulphides	MnS	18,1	(69-138)	(0,3)
	CaS	14,7		
Calcium aluminates	CaS·6Al ₂ O ₃	8,8	(113)	(0,234)
	CaS·2Al ₂ O ₃	5,0		
	CaO·Al ₂ O ₃	6,5		
	12CaO·7Al ₂ O ₃	7,6		
	3CaO·Al ₂ O ₃	10,0		
Spinels	MgO·Al ₂ O ₃	8,4	271	0,260
	MnO·Al ₂ O ₃	8,0		
	FeO·Al ₂ O ₃	8,6		
Alumina	Al ₂ O ₃	8,0	389	0,250
	Cr ₂ O ₃	7,9		
Nitrides	TiN	9,4	(317)	(0,192)
Oxides	MnO	14,1	(178)	(0,306)
	MgO	13,5	306	0,178
	CaO	13,5	183	0,21
	FeO	14,2		
(Matrix) 1% C, 1.5% Cr	(850 °C -> Ms)	(23,0) (10,0)		
	(M _f -> R.T.) γ -> α' (850 °C -> R.T.)	12,5	206	0,290

Adhesion to the matrix

The adhesion of the inclusion to the matrix is not always perfect, which may make it easy for a fatigue crack to initiate from the interface between the inclusion and the matrix. Fatigue crack may also initiate through the inclusion, i.e., the inclusion cracks, or it may initiate from the interface between the different phases of the inclusion. The fatigue crack initiation is usually faster in the cases where a crack initiates from a cracked inclusion than in the cases where a crack initiates from the interface between the inclusion and the matrix. In investigations of Melander & Gustavsson (1996) and Melander & Ölund (1999) FEM calculations revealed that the driving forces for small cracks which initiated at alumina inclusions with internal cracks were significantly higher than the driving forces for small cracks which initiated at alumina inclusions without internal cracks, and that increasing coefficient of friction on the interface between inclusion and matrix leads to reduced driving force for crack growth in cases where debonding and sliding can occur on the interface.

Many efforts have been made to evaluate quantitatively the stress concentration factors for inclusions by assuming that their shapes are spherical or ellipsoidal, but these assumptions have led only to rough estimates, because slight deviations from the assumed geometry can greatly affect the stress concentration factor (Murakami

et al., 1989). It must also be noted that irrespective of the Young's modulus of the inclusion and its adhesion to the matrix, the maximum stress at some point in the vicinity of an inclusion is always greater than the remote stress.

1.5 Fatigue crack initiation and crack growth

Fatigue failure can be divided into three phases: crack initiation, crack propagation, and final fracture. The stress field in the vicinity of a fatigue crack is described in linear elastic fracture mechanics with the help of a parameter called the stress intensity factor, K . The driving force for the crack growth in two specimens of different shape and at different nominal stress is the same when K is the same. The general form of the stress intensity factor can be written as a function of crack depth a and applied load σ (e.g., Hertzberg, 1996):

$$K = f(\sigma, a) \quad (1)$$

where the functionality depends on the configuration of the cracked component and the manner in which the loads are applied. Stress intensity factor solutions for various crack configurations have been collected in handbooks (e.g., Murakami, 1987).

In cyclic loading, the stress intensity factor range, $\Delta K = K_{\max} - K_{\min}$, is the critical factor for the fatigue crack propagation. If the stress intensity factor range, ΔK , is less than a certain critical value, no crack propagation is observed. This critical value is called the threshold stress intensity factor range, ΔK_{th} . During the crack initiation period, substructural and microstructural changes which cause nucleation of permanent damage take place and visible microscopic cracks are created. These microscopic cracks may grow and coalesce to form dominant cracks, which may eventually lead to a final fracture.

In Figure 3 the three distinct regimes of the fatigue crack growth are shown. In regime A, which is associated with the existence of a threshold stress intensity factor range, ΔK_{th} , the average growth increment per cycle is smaller than the lattice spacing. Regime B is known as the Paris regime and it exhibits a linear dependence of $\log da/dN$ with $\log \Delta K$ according to equation 2, which is known as the *Paris law*:

$$\frac{da}{dN} = C_p (\Delta K)^m \quad (2)$$

where C_p and m are empirical constants which are functions of the material properties and microstructure, fatigue frequency, mean stress or load ratio, environment, loading mode, stress state and test temperature (Suresh, 1992).

In regime C the ΔK values are high and the crack growth rates increase rapidly being significantly higher than those observed in the Paris regime causing fast catastrophic failure. The sensitivity of the crack growth to microstructure, load ratio and stress state is also very pronounced.

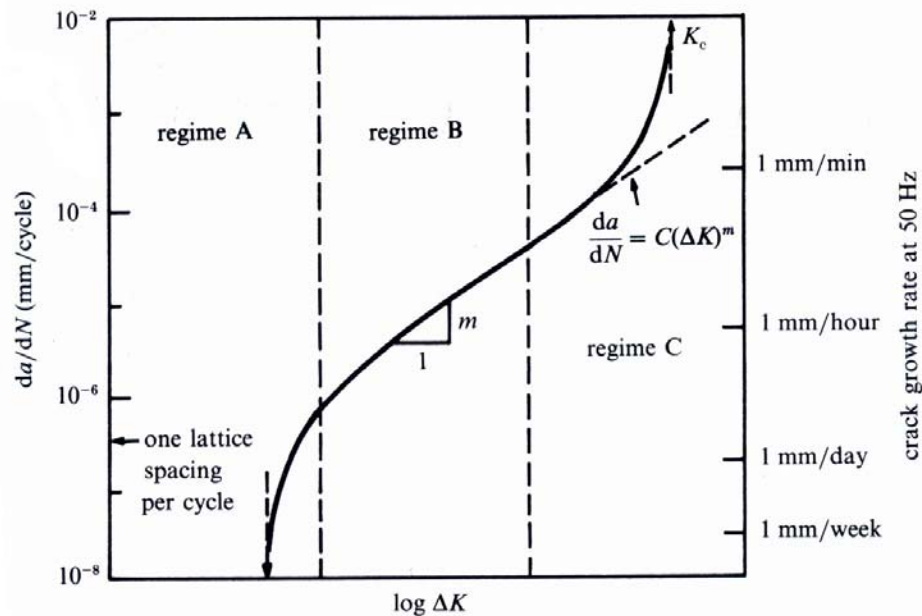


Figure 3. Different regimes of stable fatigue crack propagation (Suresh, 1992).

In high-cycle fatigue, i.e., when the load amplitudes are near the fatigue limit, the material deforms primarily elastically and the failure time or the number of cycles to failure under such high-cycle fatigue conditions has traditionally been characterized in terms of the stress range. In high-cycle fatigue most of the fatigue life is spent in the crack initiation phase. In low-cycle fatigue, i.e., when the load amplitudes are generally high enough to cause appreciable plastic deformation prior to failure, the fatigue life is characterized in terms of the strain range. In low-cycle fatigue the crack initiation takes place in a relatively short time and most of the fatigue life is spent in the crack propagation phase.

Fatigue crack initiation usually takes place in the surface of the material, because the restraint on cyclic slip is relatively low at the surface (Schijve, 1984). Cyclic deformation results in the roughening of the surface of the material, which is manifested as sharp microscopic peaks and valleys, known as extrusions and intrusions, see Figure 4. The cyclic slip is accumulated along certain bands, which are oriented parallel to the maximum shear stress. In defect-free materials, the fatigue cracks are usually initiated from these favourably oriented bands known as *persistent slip bands*. Depending on the material, persistent slip bands are formed at a stress level 5-10 % lower than the ideal fatigue strength, σ_{w0} , of a defect-free material, see section 1.10 for empirical equations for σ_{w0} (Murakami, 2002).

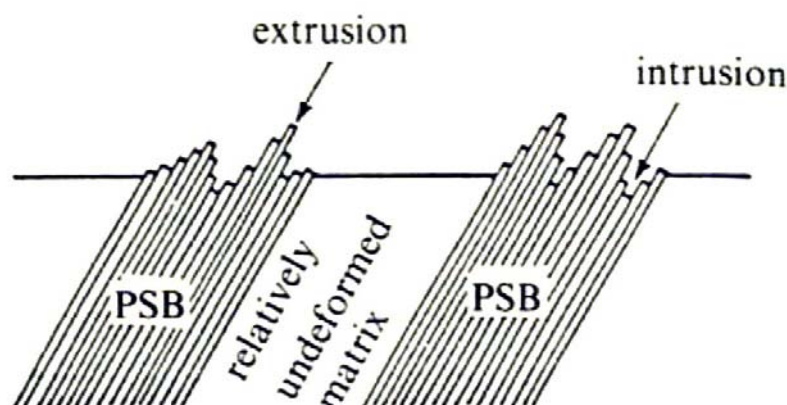


Figure 4. Persistent slip bands produced in the material surface by cyclic deformation (Suresh, 1992).

Fatigue cracks may also initiate from material inhomogeneities such as grain boundaries, precipitates or non-metallic inclusions. Fatigue crack may initiate from the interface between the inclusion and the matrix or the inclusion itself may crack. Fatigue crack initiation is a so-called weakest link phenomenon, i.e., fatigue crack initiates from the largest defect present. Fatigue crack initiation is dependent on the stress concentration factor of the defect. During cyclic loading local plastic flow can take place under the influence of stress concentration which can lead to fatigue crack initiation. When defects having the same size but different shape are compared, fatigue cracks initiate earlier from a sharp crack, than, for example, a round hole, which usually means that the fatigue life is shorter, when the fatigue crack initiates from a sharp crack. When an internal inclusion becomes a fracture origin a white circular area, which is nowadays called a “fish eye”, is formed in the vicinity of the inclusion. Duckworth & Ineson (1963) reported that a fracture due to an internal inclusion has a longer fatigue life than a fracture due to a surface inclusion.

1.6 Stress concentration and fatigue notch effect

The stress at the edge of a hole, or at a notch root, has a higher value than stresses at the other places in the structure have. This phenomenon is called stress concentration. However, the characteristics of stress concentration at a crack tip are quite different from those at holes and notches. Figure 5 shows a circular hole in an infinite plate under a uniaxial remote tensile stress, σ_{x0} , in the x-direction. The tangential stress, σ_{θ} , at points A and C is three times larger than σ_{x0} , that is $\sigma_{\theta} = 3\sigma_{x0}$, i.e., the stress concentration factor $k_t = 3$.

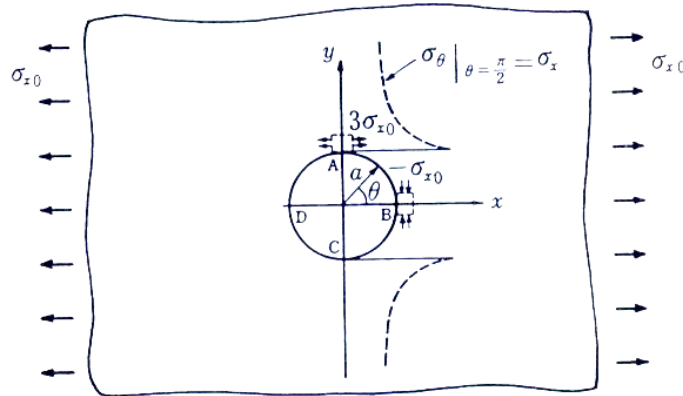


Figure 5. Stress concentration at a circular hole: $\sigma_{xA} = 3\sigma_{x0}$, $\sigma_{yB} = -\sigma_{x0}$ (Murakami, 2002).

When a spherical inclusion is considered, the value and the location of the maximum stress depend on the values of Young's modulus, E , and Poisson's ratio, ν , of the inclusion and of the matrix (Murakami, 2002). Stress concentration values for various notches under various boundary conditions have been collected in handbooks (e.g., Peterson, 1974; Pilkey, 1997). Notches having geometrically similar shape have the same value of stress concentration factor regardless of the difference in size.

A crack has a sharp tip whose root radius ρ is zero. In elastic analysis, a crack is defined as "the limiting shape of an extremely slender ellipse". The stress concentration ahead of an extremely slender elliptical hole, i.e., at the crack tip, thus, becomes infinite regardless of the length of the crack. Therefore, it is not appropriate to compare the maximum stresses at the tips of various cracks as a measure of their stress concentration. The stress concentration solution for a crack was presented by Irwin (1950) as a stress intensity factor, which was defined as the parameter describing the intensity of the singular stress field in the vicinity of a crack tip. The stresses in the vicinity of a crack tip have a singularity of $r^{-1/2}$, where r is the distance from the crack tip. Figure 6 shows a crack of length $2a$ in the x -direction in a wide plate under a uniaxial tensile stress, σ_0 , in the y -direction. The stress intensity factor describes the singular stress distribution in the vicinity of the crack tip, and for Mode I loading, i.e., opening or tensile mode, where the crack surfaces move directly apart, it is written as:

$$K_I = \sigma_0 \sqrt{\pi a} \quad (3)$$

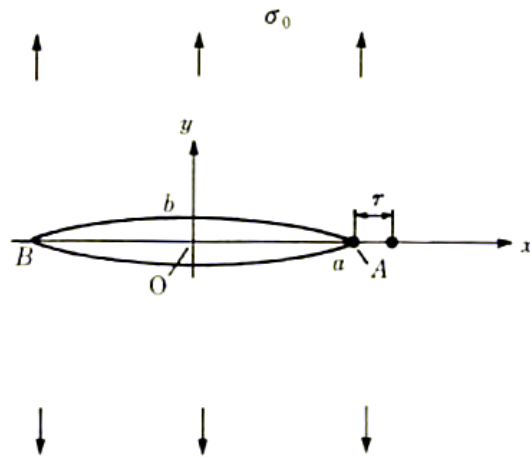


Figure 6. Two dimensional crack of length $2a$ (Murakami, 2002).

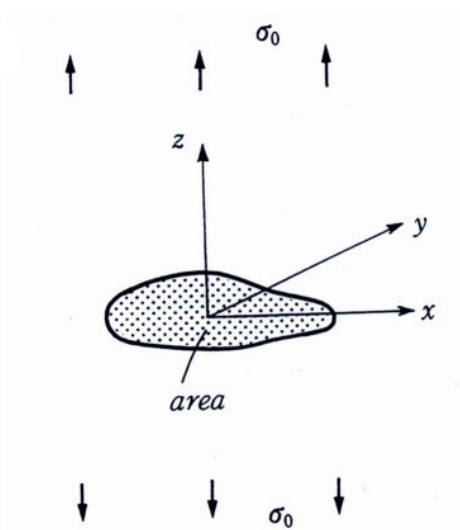
Using K_I , the normal stress, σ_y , near the crack tip on the x-axis can be expressed approximately by:

$$\sigma_y = \frac{K_I}{\sqrt{2\pi r}} \quad (4)$$

It has to be noted that once a crack emanates from a stress concentration site, the problem must be treated from the viewpoint of the mechanics of the crack, not as a problem of stress concentration at a hole or a notch. Like stress concentration solutions, many stress intensity factor solutions have been collected in handbooks (e.g., Murakami, 1987).

Figure 7 shows an internal crack on the x-y plane of an infinite solid, which is under a uniform remote tensile stress, σ_0 , in the z-direction. If the area of this crack is denoted by *area*, then, according to Murakami (2002), the maximum value, $K_{I_{max}}$, of the stress intensity factor along the crack front is given approximately by equation 5:

$$K_{I_{max}} = 0,5\sigma_0\sqrt{\pi\sqrt{area}} \quad (5)$$

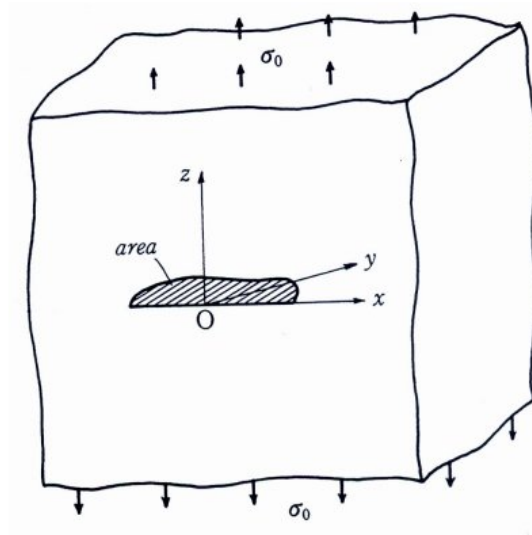


$$K_{\text{max}} = 0,5\sigma_0\sqrt{\pi\sqrt{\text{area}}}$$

Figure 7. Stress intensity factor for an arbitrarily shaped 3D internal crack (Murakami, 2002).

For a surface crack as shown in Figure 8, K_{Imax} is given approximately by equation 6:

$$K_{\text{Imax}} = 0,65\sigma_0\sqrt{\pi\sqrt{\text{area}}} \quad (6)$$



$$K_{\text{Imax}} = 0,65\sigma_0\sqrt{\pi\sqrt{\text{area}}}$$

Figure 8. Stress intensity factor for an arbitrarily shaped 3D surface crack (Murakami, 2002).

Almost 100 % of the fatigue cracks start from the sites of stress concentrations at structural discontinuities such as holes, notches, cracks, defects and scratches. The maximum stress at a stress concentration is not the only factor controlling the crack initiation. The phenomenon of decrease in the fatigue strength due to stress concentration is called the fatigue notch effect and it is described by the so-called fatigue notch factor, k_f , i.e., the relationship between the fatigue limit of an unnotched bar and the endurance limit of a notched bar. The fatigue limit of a notched component is higher than expected when looking at the maximum stress at the notch root, i.e., the fatigue limit calculated with the stress concentration factor k_t is higher than the fatigue limit obtained from tests carried out with smooth specimens. This phenomenon is called notch sensitivity and a number of theories and formulas have been developed to describe it. Notch sensitivity factor expresses the relationship between the observed fatigue notch factor and the theoretical stress concentration factor (Peterson, 1974):

$$q = \frac{1}{1 + p/\rho} = \frac{k_f - 1}{k_t - 1} \quad (7)$$

where q = notch sensitivity factor, where $0 \leq q \leq 1$

k_t = stress concentration factor

k_f = fatigue notch factor

p = characteristic material parameter

ρ = radius of the notch root

If only the local stresses at the notch root were responsible for the height of the fatigue limit and no plasticity occurs, the fatigue notch factor k_f should be identical with the stress concentration factor k_t . In reality, the fatigue notch factor is usually smaller than the stress concentration factor:

$$1 \leq k_f \leq k_t \quad (8)$$

Isibasi's (1948) model, which is presented, e.g., in Murakami & Endo (1994), proposed that a notched specimen reaches its fatigue limit when the stress at a distance ε_0 from the notch root is equal to the fatigue limit, σ_{w0} , of an unnotched specimen, and ε_0 is a material constant. For a two-dimensional crack of length $2l$ in a wide plate, Isibasi's model can be reduced to the following form:

$$\sigma_w = \sigma_{w0} \frac{\sqrt{2l\varepsilon_0 + \varepsilon_0^2}}{l + \varepsilon_0} \quad (9)$$

Siebel & Stieler (1955) proposed a method which can be used to evaluate the notch effect by using the nondimensional stress gradient, χ , which is calculated from the stress distribution normalised by the maximum stress, σ_{\max} , at a notch root. χ is given by the following equation (e.g., Murakami, 2002):

$$\chi = \left. \frac{d\sigma^*}{dx} \right|_{x=0} \quad (10)$$

where

$$\sigma^* = \frac{\sigma_y}{\sigma_{\max}} \quad (11)$$

The notch root radius, ρ , has the major influence on χ , regardless of the notch depth. Investigations of Nisitani (1968), which are presented, e.g., in Murakami (2002), extended the concept of Siebel & Stieler (1955), and made clear that the root radius, ρ , has also an effect on the non-dimensional stress distribution. Nisitani discussed on two separate threshold conditions in terms of χ : the critical stress for crack initiation at a notch root, and the threshold stress for non-propagation of a crack emanating from a notch. These two critical stresses play a very important role in structures containing initial cracks.

1.7 Non-propagating cracks

Several experiments have shown that when the specimens are fatigued with the load amplitudes just under the fatigue limit, fatigue cracks have initiated but stopped after growing some distance. It was first shown by Frost & Dugdale (1957) and Frost (1960) that the fatigue cracks emanating from the notches can arrest completely after growing some distance. These so-called non-propagating cracks indicate that the fatigue limit is not the threshold stress for crack initiation as it was believed in the early times of metal fatigue research, but it is related to the materials ability to resist the propagation of an initiated fatigue crack. When a crack is initiated at the interface between an inclusion and the matrix or a crack originates through cracking of an inclusion, the stresses within the inclusion are relieved, and the inclusion domain may be regarded as mechanically equivalent to a stress-free defect or pore. The critical stress for crack initiation, which is usually denoted by σ_{wi} , is usually 2-3 % lower than σ_{w0} (Murakami, 2002), see section 1.10 for empirical equations for σ_{w0} .

Some experiments on crack initiation at notch tips have shown that the arrest of the fatigue cracks occurs only ahead of sharp notches having the value of k_t above a certain critical value (e.g., Frost & Dugdale, 1957; Frost et al., 1974), see Figure 9. A crack initiated from a sharp notch has to reach a certain length before it can grow under its own driving force, whereas the required crack length for a blunt notch is smaller than that of a sharp notch. However, experiments with geometrically similar specimens of Nisitani (1968), which are presented, e.g., in Murakami (2002), showed that larger specimens did not have non-propagating cracks at a value of k_t , whereas smaller specimens did have non-propagating cracks at the same value of k_t .

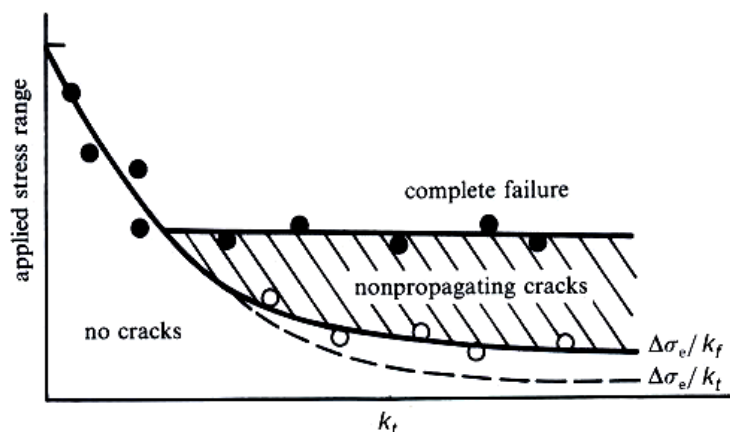


Figure 9. Threshold stress range for crack initiation at a notch tip, characterized by the unnotched fatigue limit $\Delta\sigma_e$ divided by k_f or k_t and plotted as a function of k_t (Frost et al., 1974).

A fatigue crack is likely to show the non-propagating behaviour in soft materials, whereas with hard steels, non-propagating cracks occur only within a narrow range of stress amplitude and they are usually very short (e.g., Murakami & Endo, 1981; Murakami, 2002). The length of the non-propagating cracks, which are observed in fatigue test specimens near the fatigue limit, has a tendency to decrease with increasing hardness, and is related to a critical inclusion size under which inclusions do not have an effect on the fatigue limit, i.e., inclusions which are smaller than the largest size of non-propagating cracks observed at the fatigue limit of a plain specimen do not exhibit undesirable effects on the fatigue strength. Fatigue experiments on many specimens at a stress level close to the fatigue limit have shown that the maximum size of the non-propagating cracks is always larger than the grain size. Fatigue limit is, thus, controlled by the average strength properties of the microstructure, and the grain size itself has an indirect influence on the fatigue limit.

Several theories have been proposed to explain the phenomenon of the non-propagating cracks. These theories have connections with theories of mechanisms of crack closure such as oxide-induced crack closure, roughness-induced crack closure and plasticity-induced crack closure. The plasticity-induced crack closure theory of Elber (1971), which is presented, e.g., in Murakami (2002), is considered as the most crucial and rational theory to explain the phenomenon of the non-propagating fatigue cracks. Elber (1971) proposed that the fatigue crack might be partially closed during part of the loading cycle, even when $R > 0$, and that the crack growth rates are not only influenced by the conditions ahead of the crack tip, but also by the nature of crack face contact behind the crack tip, see Figure 10.

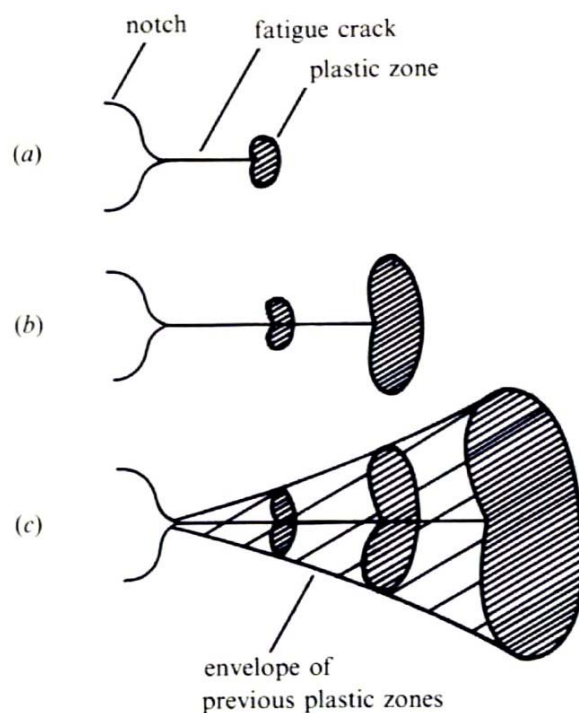


Figure 10. The development of an envelope of prior plastic zones around an advancing fatigue crack (Elber, 1971).

The residual tensile displacements, resulting from the plastic damage of fatigue crack extension, interfere along the crack surface in the wake of the advancing crack front and cause the fatigue crack to close above the minimum load level. The fatigue crack is partially closed for a portion of the loading cycle and it opens fully only after a certain opening level of K , K_{op} , is applied, i.e., the effective stress intensity factor range ΔK_{eff} is denoted by the opening ΔK level $K_{max} - K_{op}$, rather than by the applied ΔK level $K_{max} - K_{min}$.

1.8 Small crack growth

Characterization of the growth of the fatigue cracks based on the fracture mechanics primarily relies on the laboratory fatigue tests on specimens containing cracks which are typically tens of millimeters in length. However, in a number of fatigue-critical engineering components an understanding on the propagation characteristics of the fatigue cracks of significantly smaller dimensions is required. Geometric and structural discontinuities, such as grain boundaries, inclusions, precipitates, which have a small impact on the growth of a long fatigue crack, can affect the path and the rate of the advance of the small fatigue cracks because their size scale may be comparable to that of a microstructurally small flaw.

Small cracks behave differently as compared to the long cracks and the similitude concept of the linear elastic fracture mechanics, i.e., that cracks with the same

crack tip condition, e.g., ΔK , will propagate at the same rate, does not hold for physically short cracks. There are two main differences between the growth of the short and long fatigue cracks: the short fatigue cracks can grow at up to 100 times faster rates than the long cracks when subjected to the same nominal driving force, i.e., the same nominal stress intensity factor range, ΔK , Figure 11, and short fatigue cracks propagate at the nominal stress intensity factor levels below the threshold stress intensity factor range $\Delta K_{th\ lc}$ for the long cracks. Thus, when a material contains small cracks, the fatigue life predictions based on the linear elastic fracture mechanics may give nonconservative values. The first reported observations of this kind of behaviour were made by Pearson (1975).

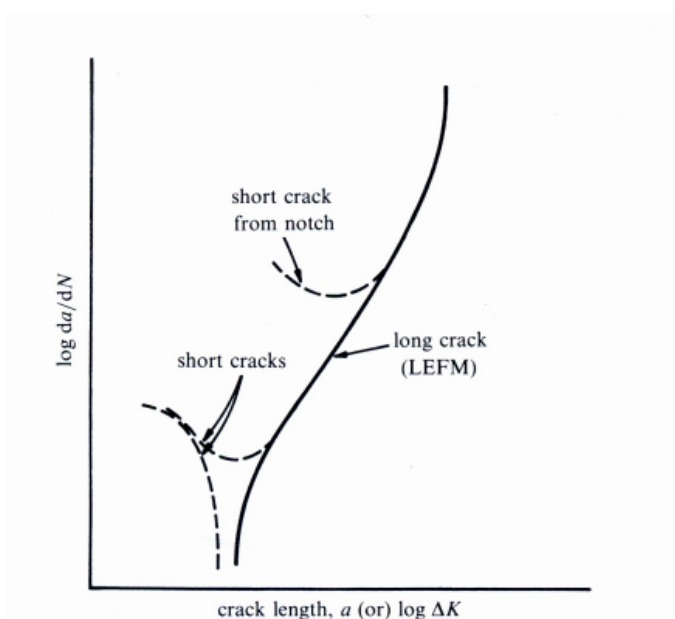


Figure 11. Schematic presentation of the typical fatigue crack growth behaviours of long and short cracks at constant values of imposed cyclic stress intensity factor range and load ratio (Suresh, 1992).

The short crack regime and the relation between the propagating and the non-propagating cracks can be presented with a diagram similar to that developed by Kitagawa & Takahashi (1976), who demonstrated that there exists a critical crack size below which ΔK_{th} decreases with the decreasing crack length. The three regimes of crack growth are presented by a modified Kitagawa-Takahashi diagram (Ellyin, 1997) in Figure 12.

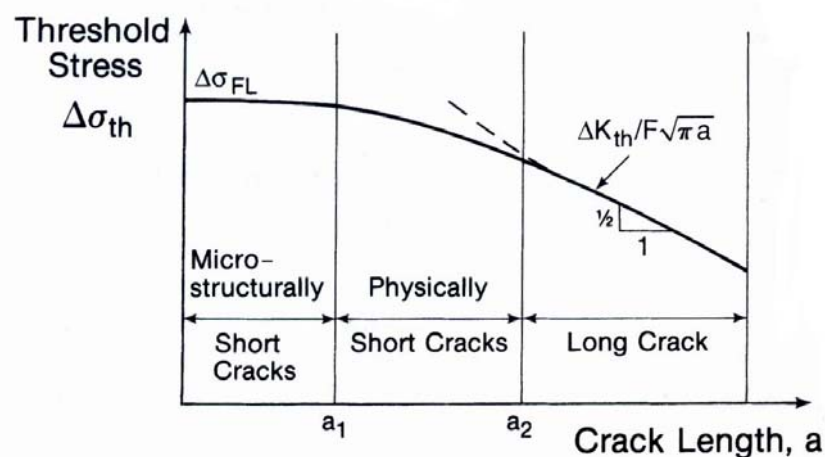


Figure 12. Three regimes of crack growth (Ellyin, 1997).

Cracks which are longer than a_2 are called "long cracks" and their growth follows the linear elastic fracture mechanics (Taylor & Knott, 1981; Taylor, 1986) and can be presented by Paris law, i.e. by equation 2. Cracks which are shorter than a_1 require a stress amplitude higher than the fatigue limit of the unnotched specimen, σ_{w0} , of the material, to be able to propagate.

Suresh & Ritchie (1984) suggested the following definitions by which the short cracks can be broadly classified:

- 1) Microstructurally small cracks; crack size is comparable to the scale of the characteristic microstructural dimension such as grain size. In this regime the crack growth is strongly affected by the microstructure and crack growth at the stress levels below the fatigue limit of the material is generally stopped at the microstructural barriers and the crack size is generally less than 0,1 mm.
- 2) Mechanically small cracks; crack size is comparable to the near-tip plasticity or crack is engulfed by the plastic strain field of a notch.
- 3) Physically small cracks; crack size is significantly larger than the characteristic microstructural dimension and the local plasticity, but is merely physically small with a length typically smaller than a millimeter or two.
- 4) Chemically small cracks; cracks which are nominally amenable to the linear elastic fracture mechanics analyses, but exhibit apparent anomalies in the propagation rates below a certain crack size as a consequence of the dependence of the environmental corrosion fatigue effects on the crack dimensions.

Non-metallic inclusions in steel can be expected to behave in the same way as the small cracks when their effect on the fatigue strength of a steel is considered. Since the effects of small defects and non-metallic inclusions are essentially the small crack problem, the problems with non-metallic inclusions can only be solved in a unified form from the small crack fracture mechanics point of view.

1.9 Size effect

Real structures, which are larger in size than the specimens of the laboratory fatigue tests, have considerably lower fatigue strengths. This phenomenon is called the size effect. Engineering handbooks often present this effect in the form of the design curves, which have been determined by the fatigue tests on the specimens with the same geometries but different sizes. Some formulas have been proposed both for the smooth and the notched specimens and for different loading conditions (e.g., Makkonen, 1999), e.g., a formula of Roark presented by Shigley & Mischke (1986):

$$S_e = (S_e)_{d_0} \cdot \left(1 - \frac{d - d_0}{D_0}\right) \quad (12)$$

where $d_0 = 0,3$ (inches)
 $D_0 = 15$ (inches)
 $(S_e)_{d_0}$ = fatigue limit of the 0,3 inch diameter specimen
 S_e = fatigue limit of specimen of diameter d

Kuguel (1961) proposed a size effect relation, where the fatigue limit of structures is related to the highly stressed volumes:

$$\frac{\sigma_1}{\sigma_2} = \left[\frac{V_1}{V_2} \right]^{-0,034} \quad (13)$$

where σ_1 and σ_2 are the fatigue limits
 V_1 and V_2 are the material volumes stressed to more than 95% of the maximum stress

Basically there are two reasons for the size effect (Murakami, 2002):

- 1) differences in the stress distribution for the different sizes, and
- 2) statistical scatter of strength and microstructure at the critical part under cyclic loading.

Differences in the stress distribution for the different sizes is basically similar to the notch effect. The stress concentration factor, k_t , for two geometrically similar specimens with different sizes, under the same nominal stress is the same and the values of the maximum elastic stresses at the notch tips of both specimens are also the same, but the stress gradient, χ , is smaller for the larger specimen, and accordingly the critical condition for the larger specimen is more severe than that for the smaller specimen.

Statistical scatter of strength and microstructure at the critical part under cyclic loading is not only very important for the high strength steels but also for the low strength steels containing various types of defects and, e.g., cast irons having complex microstructures. Especially in cast irons containing graphite nodules surrounded by ferrite phase in pearlite matrix, i.e., the bull's eye structure, the hardness of the microstructure is not uniform. When the defects, e.g., the non-metallic inclusions become the fatigue fracture origin, in a volume of material subjected to the same cyclic stress, the fatigue failure occurs at the largest defect that is present in the volume, i.e., fatigue fracture is a so-called weakest link phenomenon. The fatigue strength is, thus, controlled by the extreme values of the population of defects. The size of the maximum defect in the population of defects can be estimated by the statistical methods such as statistics of extreme value (SEV) method.

1.10 Models describing the effects of defects on fatigue strength

When inclusions or any other kind of material impurities do not affect fatigue crack initiation, fatigue crack initiates from slip bands which are formed on the material surface and there exists a linear relationship between material strength or hardness and fatigue limit. The following empirical equations have been used previously for the approximation of the ideal fatigue strength σ_{w0} :

$$\sigma_{w0} \cong 0,5\sigma_U \quad (13)$$

$$\sigma_{w0} \cong 1,6HV \pm 0,1HV \quad (14)$$

where σ_U is the ultimate tensile strength (MPa) and HV is the Vickers hardness (kgf/mm^2).

Equation 14 is valid for $HV < 400$, but non-conservative for $HV > 400$. This approximation does not depend on the microstructure, such as ferrite, pearlite or martensite, according to Chalant & Suyitno (1991), or on the steel type meaning that changing the microstructure by metallurgical processes or by heat treatments affects the fatigue strength only through the hardness value. Microstructure itself may have an effect on fatigue crack growth rate but not on fatigue limit. Theoretically equation 14, which predicts the upper limit of fatigue strength, i.e., the ideal fatigue strength, is also valid for steels with higher hardness or strength and free from inclusions or any other material defects larger than the critical size, i.e., in the case when the slip bands in the microstructure become the origins of the fatigue fracture. In other words, fatigue strength degradation in high strength steels is caused by the presence of inclusions or other material defects larger than the critical size, which is a function of Vickers hardness. The large scatter of fatigue strength values of hard steels is caused by the variety of shapes and locations of inclusions. Garwood et al. (1951) reported the relationship between the fatigue

strength and Vickers hardness for a wide range of steels with different hardness values, see Figure 13.

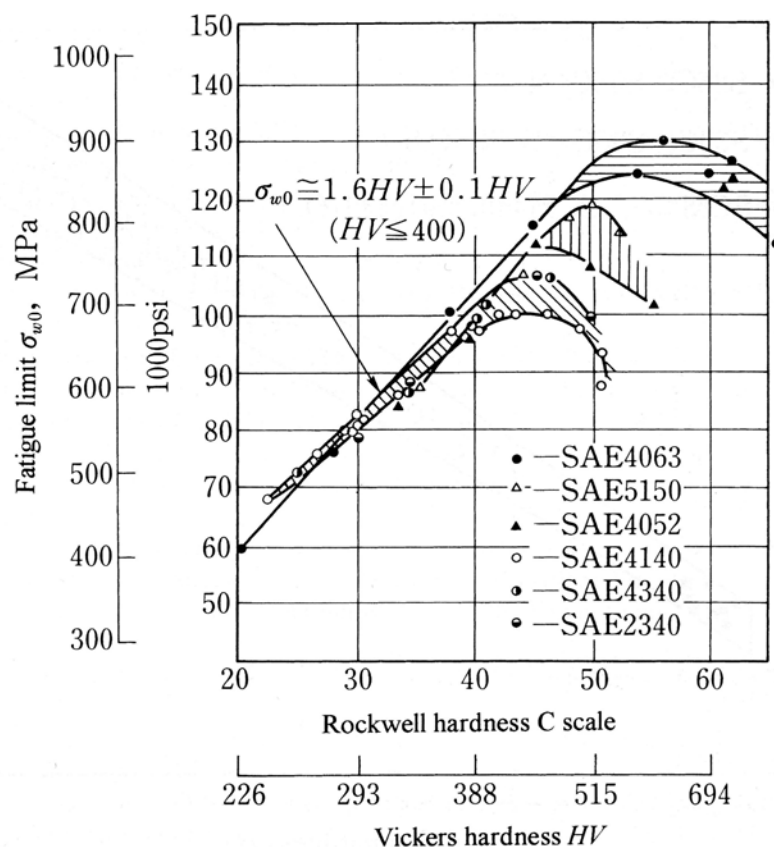


Figure 13. Relationship between hardness and fatigue limit (Garwood et al., 1951).

It has to be noted that the exact relationship between the fatigue limit and hardness cannot be derived from the average hardness of a specimen because it is the hardness of the microstructure in the vicinity of the crack initiation site that determines the fatigue limit.

If it is accepted that the fatigue limit of a material containing small defects or cracks is the threshold condition for non-propagating cracks, then it is rational to first consider ΔK_{th} , rather than to immediately consider the fatigue limit stress, σ_w . Today it is well known that ΔK_{th} for small cracks depends in general on crack size, and decreases with decreasing crack size (Kitagawa & Takahashi, 1976). For long cracks the values of ΔK_{th} are a material constant. Figure 14 presents the relationship between ΔK_{th} and defect or crack size, in which data for fatigue limits of specimens containing either a small defect or a small crack have been collected from the literature (Murakami & Endo, 1994).

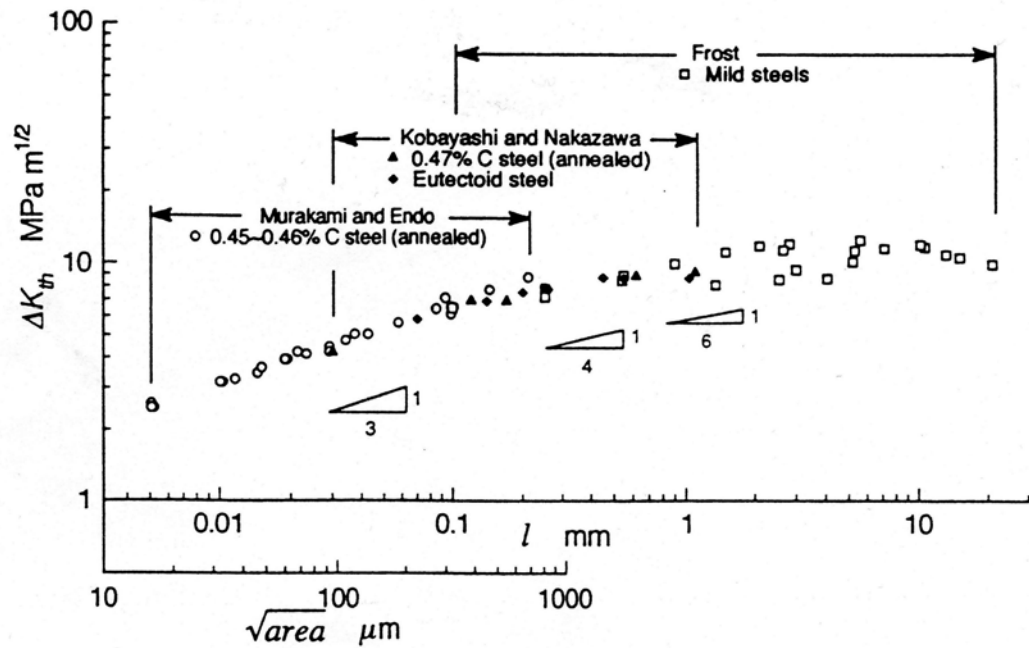


Figure 14. Dependence of ΔK_{th} on crack or defect size (square root of the projection area of a defect) from different research data (Murakami & Endo, 1994).

In Murakami & Endo (1994), models predicting the effects of defects, inclusions and inhomogeneities on the fatigue strength of metals are reviewed and classified into the following groups:

Frost's model and other similar models

Frost (e.g., Frost & Dixon, 1967) investigated the relationship between the fatigue limit σ_w and the crack depth l and presented an empirical equation of the form:

$$\sigma_w^3 l = C_F \quad (15)$$

In Frost's experiments cracks and notches with depths $l = 100-20900 \mu\text{m}$ were investigated. Kobayashi & Nakazawa (1969) conducted a similar study on cracks and notches with $l = 30-1100 \mu\text{m}$ and modified Frost's model to $\sigma_w^4 l = C_{KN}$ (Murakami & Endo, 1994). Murakami & Endo (1983) investigated smaller cracks, $10 \mu\text{m} < \sqrt{\text{area}} < 1000 \mu\text{m}$, and proposed the equation:

$$\sigma_w^6 \sqrt{\text{area}} = C_{ME} \quad (16)$$

where $\sqrt{\text{area}}$ is the square root of the projection area of a defect. According to Murakami & Endo (1994), the change in exponents in the equations above is due to the difference in size ranges of the defects investigated in the studies.

Approaches based on fatigue notch factor

In studies by Mitchell (1977; 1979), which are presented in Murakami & Endo (1994), and Nordberg (1981), Peterson's equation (1959), which was originally proposed for large notches, was applied to small cracks, small defects and non-metallic inclusions:

$$\sigma_w = \frac{\sigma_{w0}}{1 + (k_t - 1)/(1 + C' / \rho)} \quad (17)$$

where σ_{w0} = fatigue strength of a defect-free specimen
 k_t = elastic stress concentration factor
 ρ = tip radius of a geometric discontinuity
 $C' = 0,0254(2070/R_m)^{1,8}$ or $C' = 0,0254(600/HB)^{1,8}$

The disadvantage for practical use of this model lies in the difficulty of obtaining the exact value of k_t of non-metallic inclusions having various irregular shapes, because a slight deviation in inclusion geometry changes significantly the value of k_t . In order to avoid this problem, Mitchell (1979) assumed all defects to be equivalent to hemispherical pit with $k_t = 2,5$. Nordberg (1981) used $0,52 \cdot R_m$ as an approximate for σ_{w0} and $k_t = 2,0$ for spherical inclusions.

Fracture mechanics approaches

The fracture mechanics approaches to small crack problems began with Kitagawa & Takahashi's study (1976). These approaches may be classified into that based on ΔK_{th} and that centred on the cyclic plastic zone size calculation based on the Dugdale model. Concerning ΔK_{th} , it has been agreed that the value of $\Delta K_{th\ sc}$ for short cracks or small cracks is smaller than that of $\Delta K_{th\ lc}$ for long cracks. These models are based on ΔK_{th} generally expressed as a function of $\Delta K_{th\ lc}$, the fatigue limit σ_{w0} of smooth, i.e., unnotched specimens, the fictitious crack length l_0 or the non-damaging crack length l_i and so on. In these models, researchers employ their own hypotheses on fracture-mechanics-like concepts.

Existing models cover mostly two-dimensional cracks or two-dimensional notches only. However, in few models an equation covering three-dimensional cracks or defects is presented, and its applicability is verified by experiments on various materials.

The use of stress concentration factors, k_t , for estimating the fatigue strength of steels has been noticed to be not only unreasonable but also impractical. The inclusions and other small defects have various shapes which are far from spherical or ellipsoidal and any slight deviation from these roughly estimated geometries can greatly affect the stress concentration factor. (Murakami & Endo, 1994).

1.11 Murakami-Endo model

The effect of non-metallic inclusions on the fatigue strength has been investigated for a long time and it has been proposed that the effects of non-metallic inclusions must be analysed from the small defects or small cracks point of view (e.g., Murakami & Endo, 1981), because the threshold condition at the fatigue limit is not that for the crack initiation but that for the non-propagation of a crack emanating from defects or inclusions. The concept of the \sqrt{area} model suggests that the inclusion shape does not have an effect on the fatigue strength if the values of \sqrt{area} of two inclusions are identical. This prediction is in agreement with the studies by Duckworth & Ineson (1963), who artificially introduced spherical and angular alumina particles into ingots and found no definite difference based on the effect of inclusion shapes.

The model proposed by Murakami & Endo (1983), i.e., equation 16, was revised by Murakami & Endo (1986) and it can be presented by the following equations:

$$\Delta K_{th} = 3,3 \times 10^{-3} (HV + 120) (\sqrt{area})^{1/3} \quad (18)$$

where ΔK_{th} is in $\text{MPa}\sqrt{m}$ and \sqrt{area} is in μm , and

$$\sigma_w = C(HV + 120) / (\sqrt{area})^{1/6} \quad (19)$$

Equation 19 was revised by Murakami et al. (1990) and an equation which takes the residual stresses of the specimens into account was proposed:

$$\sigma_w = C(HV + 120) / (\sqrt{area})^{1/6} \cdot [(1 - R) / 2]^{\alpha_{ME}} \quad (20)$$

where $C=1,43$ for a surface inclusion, $C=1,56$ for an internal inclusion and $C=1,41$ for an inclusion in touch with the free surface, see Figure 15.

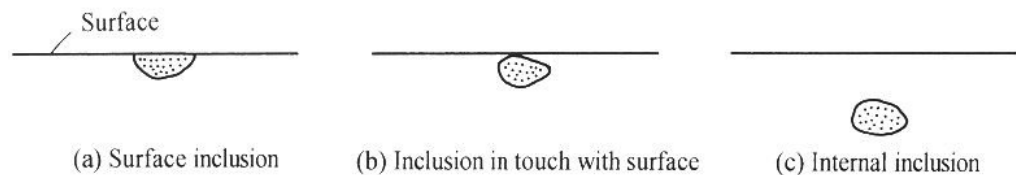


Figure 15. Classification of inclusions by location (Murakami et al., 1991).

The units are: \sqrt{area} (the square root of the projection area of inclusion), μm ; HV, kgf/mm^2 ; and σ_w , MPa. R (stress ratio at inclusion) = $\sigma_{\min} + \sigma_{\text{res}} / \sigma_{\max} + \sigma_{\text{res}}$ (σ_{res} = residual stress at inclusion) and $\alpha_{ME} = 0,226 + HV \times 10^{-4}$. σ_w is the fatigue limit, i.e., the critical stress under which fatigue cracks emanating from an initial crack stop propagating. Since an inclusion is most detrimental when it exists just in

touch with the free surface of a specimen, i.e., $C=1,41$, the lower bound of the fatigue limit, σ_{wl} , is the fatigue limit for the maximum inclusion, $\sqrt{area_{max}}$, that exists in a material volume to be examined. It was concluded from more than 100 experimental data that the prediction error of equation 19 is mostly less than $\sim 10\%$ for notched and cracked specimens having \sqrt{area} less than $1000 \mu\text{m}$ and for Vickers hardness, HV, ranging from 70 to 720. The prediction error of equation 19 was reported to be less than $\sim 15\%$ for HV ranging from 100 to 740. Equations 18 and 19 are reported to be valid over a \sqrt{area} range, which is dependent on material. The valid upper limit of \sqrt{area} is considered to be $\sim 1000 \mu\text{m}$. If the predicted value of σ_w for a \sqrt{area} exceeds the ideal upper bound of the fatigue limit $\sigma_{wU} \approx 1,6\text{HV}$, the defect having such a small \sqrt{area} should be regarded as non-detrimental.

When a fixed number of sets of data following some basic distribution, such as normal distribution, exponential distribution, log-normal distribution etc., is chosen, the maxima and minima of each of these sets also follow a distribution. The extreme value type I distribution has two forms, one based on the smallest extreme and the other based on the largest extreme. The extreme value type I distribution is also referred to as the *Gumbel distribution* (Gumbel, 1958). The distribution of inclusions in metals is expected to be nearly exponential which makes its extreme distribution doubly exponential. Statistics of extreme value method can be used to predict the value of $\sqrt{area_{max}}$ of inclusions that exist in a certain material volume. The statistical distribution of extreme values of \sqrt{area} can be used as a guideline for the control of inclusion size in the steelmaking processes and, for example, for comparisons between the cleanliness level estimations of the steels with different cleanliness or oxygen levels.

The largest inclusion expected to exist in a material volume is estimated with the statistics of extreme value method. The details of this method are presented by Murakami et al. (1994) and basically the procedure is as follows, see Figure 16:

- (1) A section perpendicular to the maximum principal stress is cut from the specimen.
- (2) A standard inspection area S_0 (mm^2) is fixed. In the area S_0 the inclusion of maximum size is selected and this operation is repeated n times.
- (3) The values of $\sqrt{area_{max,j}}$ are classified, starting from the smallest, and indexed from $j=1 \dots n$. The cumulative distribution function $F_j(\%)$, and the reduced variates y_j are then calculated from the equations:

$$F_j = j \times 100/(n+1) (\%) \quad (21)$$

$$y_j = -\ln[-\ln(j/(n+1))] \quad (22)$$

(4) The obtained data are plotted on a probability paper the abscissa being $\sqrt{area_{max,j}}$ and the ordinate either F_j or y_j .

(5) The reduced variates y_j plotted against $\sqrt{area_{max,j}}$ give a straight line and the linear distribution of the maximum size of inclusions can be expressed by equation:

$$\sqrt{area_{max}} = a \times y + b, \text{ where} \quad (23)$$

$$y = -\ln[-\ln((T-1)/T)] \text{ and} \quad (24)$$

$$T = (S+S_0)/S_0 \quad (25)$$

T represents the return period and S the area of prediction. When $S \gg S_0$, instead of equation 25, the following approximate equation may be used:

$$T = S/S_0 \quad (26)$$

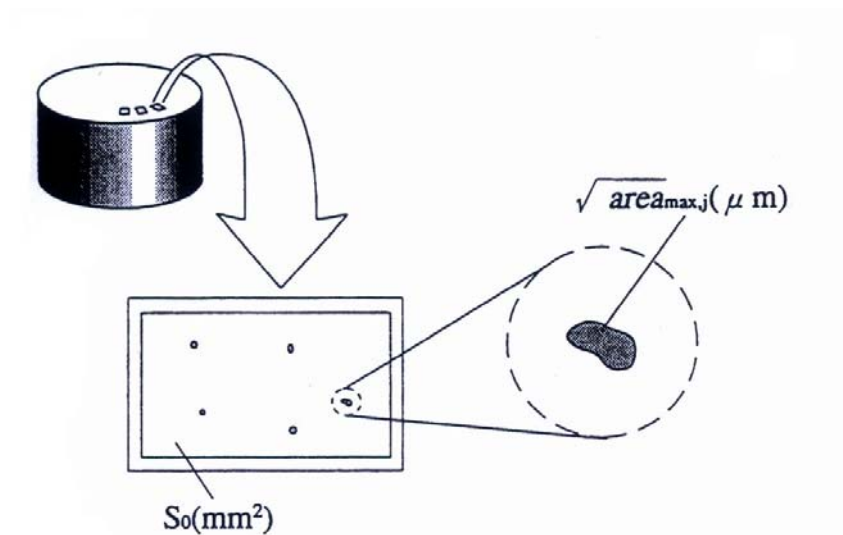


Figure 16. A practical procedure of the inclusion rating by statistics of extreme values (Murakami et al., 1994).

The method described can be applied to 2D problems and the exact value of $\sqrt{area_{max}}$ in a volume cannot be directly predicted with this 2D method. In the method described a thickness h_0 is added to S_0 and the standard inspection volume is then defined by:

$$V_0 = h_0 \times S_0 \quad (27)$$

where h_0 is the average value of $\sqrt{area_{max,j}}$, i.e.:

$$h_0 = (\Sigma \sqrt{area_{max,j}}) / n \quad (28)$$

and

$$T = (V + V_0) / V_0 \quad (29)$$

and when $V \gg V_0$

$$T = V / V_0 \quad (30)$$

In Zhou et al. (2002) a polishing method was proposed to estimate the 3D extreme value distribution of the inclusions contained in a small inspection volume V_0 . It was discovered that the 2D method, i.e., the standard inspection area S_0 method described above results with a negligible error when compared with the 3D method if the inclusions detected by both methods are of the same type. This supports the use of equation 27 as a practical formula to estimate the standard inspection volume.

It has to be remembered, that in the statistics of extreme value evaluation the extrapolation to a large volume is usually performed from a very small area, and, thus, the accuracy of the evaluation may become questionable. If two different data sets of maximum inclusions are detected with two different standard inspection volumes V_a and V_b (or with two different standard inspection areas S_0 and S_b) with $V_b = t \cdot V_a$ the relationship between the distributions of maximum defects can be derived from equation 31:

$$F_{V_b}(x) = [F_{V_a}(x)]^t \quad (31)$$

where $F_{V_a}(x)$ is the cumulative distribution function for standard volume V_a and $F_{V_b}(x)$ is the cumulative distribution function for standard volume V_b . Equation 31 can be used for plotting two data sets of inclusions detected with two different standard inspection volumes V_a and V_b in terms of an equivalent distribution. It was shown by Beretta & Murakami (2001) that in some cases the statistics of extreme graph of two data sets obtained with different control volumes or areas may have a bilinear shape caused by the presence of two defect types. The cumulative distribution of extreme inclusions can then be described as a mixture of two different extreme value distributions:

$$F_{mix}(x) = (1-P) \cdot F_1(x, \lambda_1, \delta_1) + P \cdot F_2(x, \lambda_2, \delta_2) \quad (32)$$

where P is the fraction of type 2 inclusions and F_1 is the largest extreme value cumulative distribution of type 1 particles with parameters λ_1 and δ_1 . Maximum likelihood method is used in estimating the parameters of $F_{\text{mix}}(x)$ fitting a given data set of inclusions sampled on different control areas. According to Beretta & Murakami (1998), the maximum likelihood method results in smaller standard error in SEV evaluation than, e.g., the least squares method. The minimum control volume or area needed for detecting the second (larger) type of defects can be estimated by the intersection of the two lines corresponding to the two extreme value distributions of the two original data sets.

Another method based on a different branch of the extreme value theory, termed as the generalised Pareto distribution (GPD) method, was developed by Shi et al. (1999). As opposed to the SEV method, GPD method makes use of all inclusions which are over a certain threshold size. Another difference between these two methods is that under certain conditions, the predictions with the GPD method are directed to an upper limit of the maximum inclusion size, which is more in accord with the expectations from steelmaking practice (Shi et al., 1999; Anderson et al., 2000; Atkinson, et al., 2000).

2 AIMS OF THE STUDY

The inclusion oriented fatigue problem is nowadays generally associated with the high strength steels. In calcium treated steels large globular inclusions may cause fatigue problems also at lower strength levels. The conventional inclusion rating methods, which are used by steel industry, and some of which have been adopted as the standards in particular countries, most often do not show any consistent correlation with the fatigue strength of steels. The main reason for this is that these inclusion rating methods take into account also the small inclusions, which are not involved in the fatigue failure. Fatigue crack initiates most likely from the largest inclusion in the material volume, and the size of this largest inclusion can be evaluated using the statistics of extreme value (SEV) method, which has numerous industrial applications (e.g., Murakami, 1996; Beretta et al., 1997).

The aims of the present work are:

- To clarify the differences between the fatigue behaviour (fatigue limit, fatigue crack origins, scatter of fatigue life etc.) of a calcium treated carburizing steel with two different calcium treatment levels;
- To study the relationship between cleanliness level estimates obtained by conventional inclusion rating methods and ultrasonic testing in immersion, and fatigue behaviour of these steels;
- To study the applicability of statistics of extreme value method and the Murakami-Endo model to the fatigue behaviour estimation of these steels;
- To determine the critical sizes of inclusions in these steels by fatigue tests and the expected maximum inclusion sizes by statistics of extreme value method. Expected maximum inclusion sizes can be used to predict the fatigue limit of the steel and as a database for the reduction of inclusion size in the steelmaking process.

3 EXPERIMENTAL METHODS

22 industrial test charges of a carburizing steel with different calcium treatment levels were studied. Rotating bending fatigue tests were performed. The surface roughness and the residual stress profiles of the fatigue test specimens were measured before the fatigue tests. The fracture surfaces of the fatigue test specimens were investigated with a scanning electron microscope (SEM) and energy dispersive X-ray spectroscopy (EDS). The cleanliness level and inclusion distribution of the materials were characterized by standard inclusion analyses, statistics of extreme value evaluation and ultrasonic tests in immersion. The applicability of the Murakami-Endo model to these steels was evaluated.

3.1 Materials

22 industrial test charges of AISI 8620 carburizing steel with two different calcium treatment levels were studied. Calcium treatment is usually performed to enhance the castability of the steel and to modify the hard oxide inclusions into softer calcium aluminates and elongated sulfide inclusions into a globular form.

The melts had undergone vacuum and injection treatment for the inclusion modification and alloying after which they were cast into 350×280 mm blooms followed by soaking at 1280 °C and hot rolling into 135×135 mm slabs. The final phase was hot rolling into 90 mm diameter bars. After the hot rolling the materials had ferritic-pearlitic microstructure and their average grain size was about $20 \mu\text{m}$, see Figure 17. 18 of the casts were injected with a large amount of calcium and 4 of the casts were injected with a small amount of calcium.

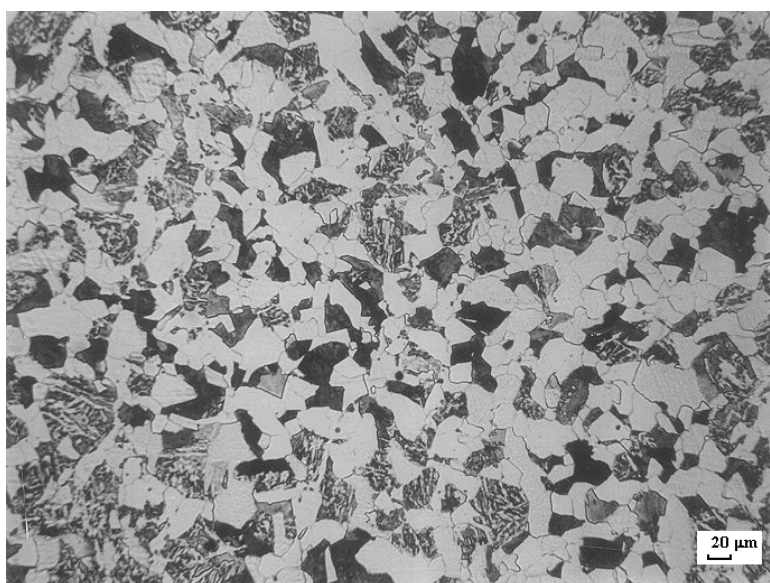


Figure 17. Optical micrograph of AISI 8620 carburizing steel in the as-rolled condition.

The chemical compositions, i.e., the cast analyses and the codes (used hereafter to identify the melts) of the studied materials are shown in Table 2.

The machinability of the studied materials tested by single point turning tests according to ISO 3685 standard and material hardnesses are presented in Table 3. The turning tests were carried out in the as-rolled condition with 45 mm diameter bars 350 mm in length which were cut from hot rolled bars 90 mm in diameter and 350 in length. Sandvik Coromant SNUN 120408 GC415 tools without cutting fluids were used in the turning tests, which were carried out by a two-axial Voest Alpine Weipert WNC-500 turning machine. The feed was 0,4 mm/r and the cutting depth was 2,5 mm. The variable indicating the machinability of the studied steels in Table 3 is the cutting speed, v_{15} (m/min), corresponding to a tool life of 15 min.

Table 2. The chemical compositions (cast analyses) of the studied materials.

Cast code	C	Si	Mn	P	S	Ca	Al _{tot}	Al _{sol}	O
A1	0,2270	0,2490	0,8720	0,0110	0,0330	0,0029	0,0190	0,0150	0,0030
A2	0,2180	0,2370	0,8710	0,0150	0,0300	0,0025	0,0190	0,0140	0,0048
A3	0,2200	0,2430	0,8280	0,0160	0,0330	0,0020	0,0220	0,0180	0,0039
A4	0,2220	0,2750	0,8420	0,0130	0,0300	0,0023	0,0210	0,0160	0,0038
A5	0,2310	0,2650	0,8340	0,0150	0,0360	0,0025	0,0180	0,0130	0,0029
A6	0,2140	0,2280	0,8680	0,0080	0,0260	0,0025	0,0200	0,0160	0,0025
A7	0,2160	0,2530	0,8740	0,0160	0,0290	0,0027	0,0170	0,0130	0,0025
A8	0,2200	0,2770	0,8620	0,0140	0,0310	0,0019	0,0200	0,0170	0,0028
A9	0,2310	0,2690	0,8650	0,0100	0,0320	0,0025	0,0200	0,0140	0,0025
A10	0,2220	0,2350	0,8600	0,0120	0,0270	0,0031	0,0190	0,0130	0,0033
A11	0,2000	0,2730	0,8710	0,0140	0,0300	0,0025	0,0220	0,0210	0,0038
A12	0,2140	0,2930	0,8510	0,0230	0,0280	0,0025	0,0190	0,0160	0,0030
A13	0,2090	0,2460	0,8750	0,0270	0,0280	0,0022	0,0180	0,0150	0,0017
A14	0,2370	0,2740	0,8360	0,0120	0,0310	0,0021	0,0180	0,0130	0,0035
A15	0,2270	0,2760	0,8550	0,0120	0,0350	0,0026	0,0190	0,0190	0,0029
A16	0,2310	0,2540	0,8740	0,0120	0,0290	0,0020	0,0170	0,0140	0,0040
A17	0,2100	0,2830	0,8260	0,0210	0,0330	0,0047	0,0200	0,0150	0,0024
A18	0,2160	0,2610	0,8580	0,0080	0,0270	0,0035	0,0200	0,0120	0,0028
B1	0,2580	0,2450	0,8020	0,0100	0,0270	0,0013	0,0240	0,0210	0,0017
B2	0,2540	0,2350	0,8170	0,0140	0,0310	0,0010	0,0250	0,0220	0,0021
B3	0,2380	0,2320	0,8130	0,0070	0,0280	0,0013	0,0200	0,0180	0,0048
B4	0,2440	0,2640	0,8290	0,0130	0,0270	0,0009	0,0220	0,0200	0,0015

A1, A2 etc. = Casts with the large amount of calcium injection

B1, B2 etc. = Casts with the small amount of calcium injection

Table 3. Machinability (v_{15}) and hardness of the studied materials in the as-rolled condition.

Cast code	v_{15} (m/min)	HB
A1	464	175
A2	501	177
A3	494	176
A4	455	177
A5	436	182
A6	471	179
A7	453	177
A8	387	177
A9	412	180
A10	441	177
A11	506	169
A12	420	176
A13	411	175
A14	504	187
A15	441	186
A16	437	172
A17	425	179
A18	407	178
B1	354	193
B2	359	181
B3	362	176
B4	366	184

3.2 Fatigue tests

The fatigue tests were carried out by using Schenck PUPN rotating bending fatigue test machines. The operating frequency was 2400 rpm, i.e., 40 Hz and the stress ratio R was -1 . A staircase method was used with a step of 25 MPa and the test was interrupted if the test specimen endured more than 10^7 cycles. Fatigue limits with 50 % failure probability were determined by a method described by Collins (1981), and fatigue test graphs were plotted for each heat.

The fatigue test specimen billets were cut from 90 mm diameter hot rolled bars after which they were hardened at 925 °C, oil quenched to 60 °C and tempered at 200 °C. After that the billets were turned and longitudinally ground into fatigue test specimens. Thus, the fatigue test specimens had a microstructure of tempered martensite, see Figure 18. The mechanical properties of the studied materials in the hardened and tempered condition are shown in Table 4. The dimensions of the fatigue test specimens are shown in Figure 19. The location of the fatigue test specimen billets cut from the hot rolled bars is shown in Figure 20.

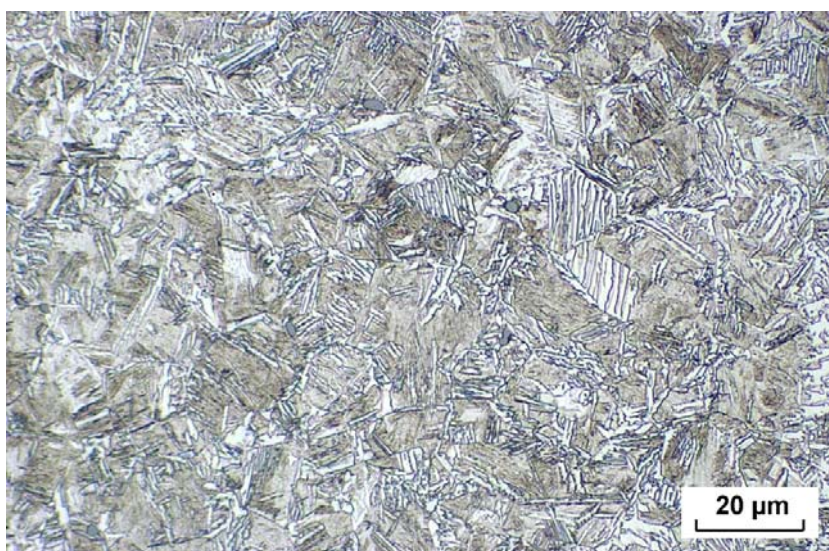


Figure 18. Microstructure of the fatigue test specimens.

Table 4. The mechanical properties of the studied materials in the hardened and tempered condition.

Cast code	R_{p0,2} (Mpa)	R_m (Mpa)	A (%)	Z (%)	HV30
A1	534	782	20,1	59	306 ± 5
A2	567	794	18,1	42	340 ± 7
A3	488	787	20,0	46	280 ± 5
A4	500	787	21,3	57	276 ± 6
A5	538	809	20,9	56	311 ± 9
A6	548	792	19,7	54	310 ± 8
A7	556	795	20,6	53	302 ± 4
A8	529	781	21,3	62	297 ± 5
A9	563	815	20,6	58	314 ± 7
A10	555	794	19,4	55	302 ± 8
A11	531	770	21,6	60	292 ± 4
A12	574	816	18,7	53	325 ± 4
A13	546	789	20,0	54	321 ± 3
A14	542	795	18,5	45	369 ± 10
A15	548	791	20,1	53	306 ± 3
A16	557	802	20,8	57	316 ± 13
A17	582	816	20,6	51	342 ± 11
A18	556	798	20,9	55	327 ± 6
B1	580	826	19,9	60	333 ± 11
B2	591	844	19,6	56	337 ± 9
B3	557	796	19,8	59	329 ± 14
B4	586	829	20,1	55	328 ± 16

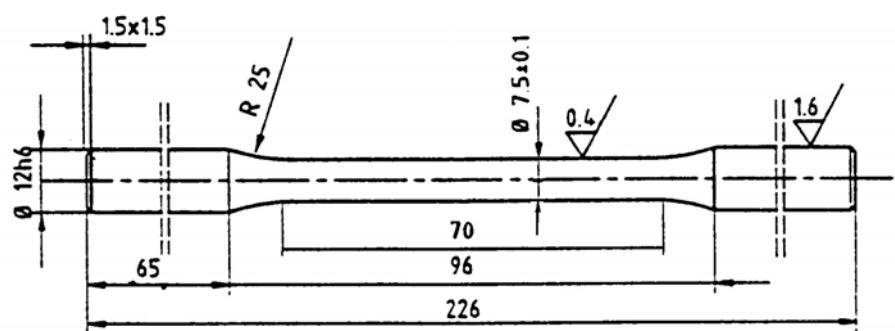


Figure 19. Fatigue test specimen geometry (dimensions in mm).

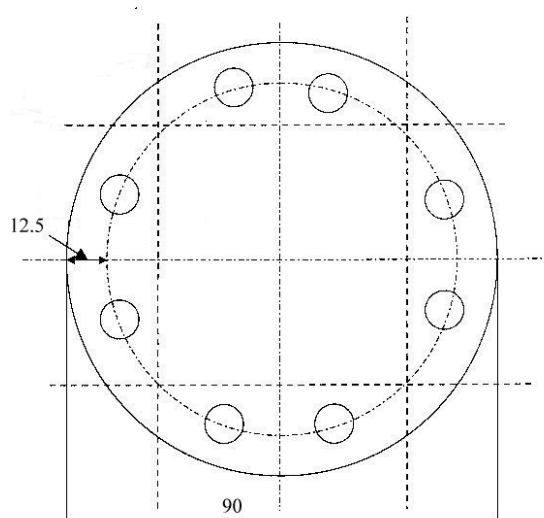


Figure 20. Locations of the billets of the fatigue test specimens cut from the hot rolled bars (dimensions in mm).

The mean value of the Vickers microhardness at three points near the fatigue crack initiation site was measured and it was used in the Murakami-Endo model. A weight of 200 g was used in the Vickers microhardness measurements.

3.3 Residual stress measurements

Different manufacturing methods, e.g., turning and grinding, usually produce residual stresses into the surface layer of the machined products. The residual stresses of the fatigue test specimens were measured with a portable X-ray diffraction unit XSTRESS3000. The measurements were performed employing Cr-K α radiation and a collimator with a diameter of 3 mm. The residual stresses were measured in four points in three different sections in the fatigue test specimens, i.e., in twelve points in each fatigue test specimen. The residual stress measurement points on the surface of a fatigue test specimen are presented in

Figure 21. Material removal of the surface layer of the specimens was carried out with a portable electrolytic polishing unit Struers Movipol and an electrolyte Struers A2 to determine the residual stress depth profiles of the specimens. Two residual stress components, σ_x and σ_t , which stand for the longitudinal and the tangential stress of the specimen, respectively, were measured. The residual stress component longitudinal to the specimen axis, σ_x , has major effect on the results of the rotating bending fatigue tests. Thus, only σ_x was taken into account in the calculations.

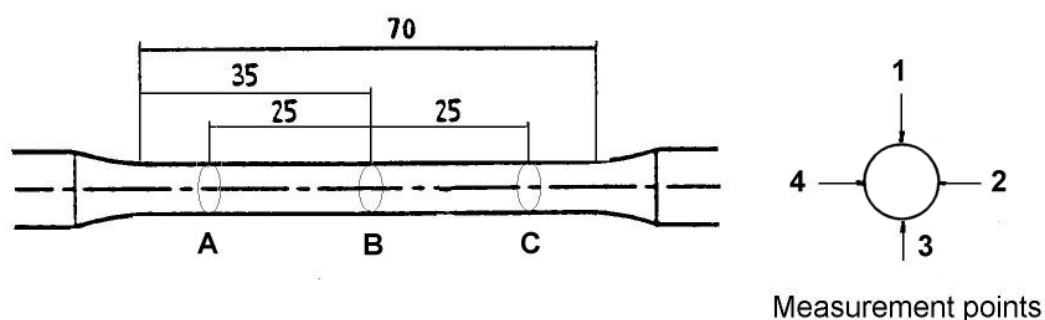


Figure 21. The residual stress measurement points on the surface of a fatigue test specimen.

All the fatigue test specimens were manufactured with the same machinery by the same technician. It was, thus, assumed that there are no large differences between the residual stress distributions of the different specimens. Residual stress measurements were performed also on ran out specimens, i.e., specimens which endured more than 10^7 cycles, to clarify the possible relaxation of the residual stresses resulting from the fatigue tests.

3.4 Surface roughness measurements

In rotating bending fatigue testing, the surface quality of the fatigue test specimens is very important, because the fatigue cracks tend to initiate from the specimen surface where the loading stress is the highest. The increase of surface roughness enhances the stress concentration at the bottom of scratch marks, resulting, thus, in a decrease in fatigue life. In surface-related fatigue fracture, cracks tend to initiate at the bottom of scratch marks (e.g., Murakami, 2002; Itoga et al., 2003), i.e., surface roughness acts as a small notch. However, existence of non-propagating cracks at the bottom of scratch marks has indicated that the fatigue limit of a specimen with surface roughness is the threshold condition for non-propagation of a crack initiated at a notch root, i.e., surface roughness has to be considered as a crack problem rather than as a notch problem.

Surface roughness values of the fatigue test specimens were measured with a portable Perthometer M4P device. All the fatigue test specimens were

manufactured with the same machinery by the same technician and, thus, the surface quality of the different specimens was assumed to be similar. Surface roughness measurements were carried out in the longitudinal direction of the specimens with a sampling length of 10 mm. 10 measurements were made for each measured specimen. R_a , R_z and R_{max} values according to the standard ISO 4287 were measured and their mean and standard deviation were calculated. Average roughness, R_a , is the average distance between the peaks and valleys and the deviation from the mean line on the entire surface within the sampling length. Mean roughness depth, R_z , is the average distance between the five highest peaks and the five deepest valleys within the sampling length. Maximum roughness amplitude, R_{max} , is the distance between the highest peak and the lowest valley within the sample length.

3.5 Inclusion analyses

Inclusion analyses according to DIN 50 602, which is based on Stahl-Eisen-Prüfplatt (SEP) 1570, and SFS-ENV 10247 inclusion analysis methods, which are used in the steel industry for steel cleanliness level determination were performed for each melt. In both methods, a total inspection area of 300 mm^2 ($20 \times 15 \text{ mm}$) was examined. The location of the analysis microsections cut from 90 mm diameter hot rolled bars is shown in Figure 22. In DIN 50 602 method two parameters, K_{O3} and K_{O4} , which stand for the measure of oxide inclusions of smaller (K_{O3}) and bigger (K_{O4}) sizes were calculated. In SFS-ENV 10247 method, the number of globular inclusions in different size categories ($3 \dots 5,5 \text{ } \mu\text{m}$, $\dots 11 \text{ } \mu\text{m}$, $\dots 22 \text{ } \mu\text{m}$, $\dots 44 \text{ } \mu\text{m}$, $\dots 88 \text{ } \mu\text{m}$, $\dots 176 \text{ } \mu\text{m}$) were counted.

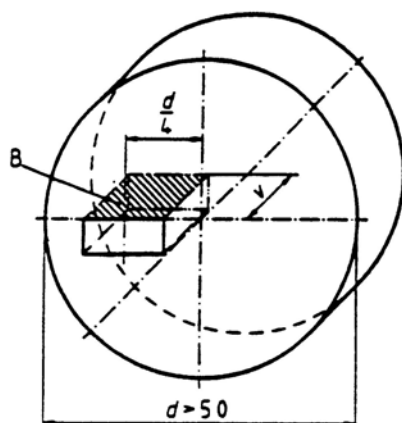


Figure 22. Location of the analysis microsections cut from the bars, i.e., plane B (dimensions in mm).

The details of these methods are described in Stahl-Eisen-Prüfblatt 1570 (1971) and SFS-ENV 10247 (1998).

3.6 Ultrasonic testing in immersion

Ultrasonic testing in immersion enables the investigation of much larger material volumes than the conventional microsection analysis based steel cleanliness level determination methods. 61-63 × 61-63 × 210 mm ultrasonic testing samples were cut from 135 × 135 mm slabs and all 4 sides of them were scanned with PAC Ultrawin II device which was equipped with Ultrawin computer program. The 4 sides of the samples were scanned both in the longitudinal and transverse directions. The location of the testing sample cut from the slab and the measurement of the sample are presented in Figure 23.

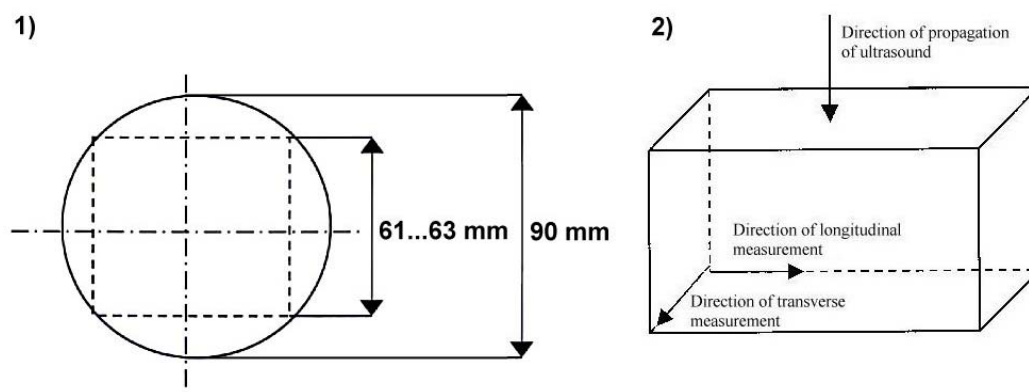


Figure 23. Location of 1) the 61...63 × 61...63 mm ultrasonic testing sample cut from the 90 mm diameter bar and 2) the principle of the scanning of the sample.

The number of inclusions (elongated and globular) in different size categories were counted. Inclusions detected were divided into two groups: linear inclusions being > 3 mm in length and globular inclusions being < 3 mm in length. The globular inclusions were divided into three categories: C1 (diameter between 40...100 μm), C2 (diameter between 100...200 μm) and C3 (diameter > 200 μm).

3.7 SEM and EDS investigations

The fracture surfaces of the fatigue test specimens were investigated with a scanning electron microscope (SEM). Zeiss DMS 962 scanning electron microscope was equipped with an energy dispersive X-ray spectroscopy (EDS) Link ISIS system. The fatigue crack initiation sites were examined and the size (\sqrt{area}), location and chemical composition of the fatigue crack initiating

inclusions were determined. ImageTool program was used in determining the values of \sqrt{area} for the fatigue crack initiation sites.

For the globular surface inclusions, i.e., globular inclusions which were cut by the fatigue test specimen surface, two values for \sqrt{area} were calculated: $\sqrt{area_1}$ being the square root of the projected area of the remainings of the inclusion on a plane perpendicular to the maximum principal stress, and $\sqrt{area_2}$ being the square root of the visually estimated whole inclusion, see Figure 24.

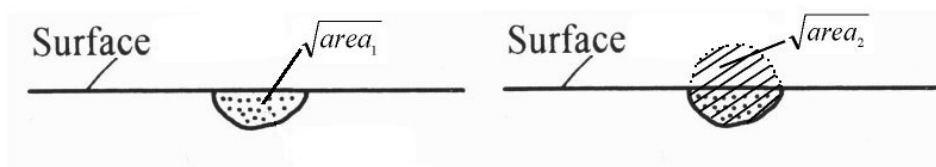


Figure 24. Size parameters $\sqrt{area_1}$ and $\sqrt{area_2}$ for surface inclusions.

SEM and EDS investigations were also made for the polished microsections cut from the fatigue test specimens to find out the possible chemical composition differences between the inclusions on the polished microsections and the inclusions at the fatigue crack initiation sites.

3.8 Statistics of extreme value evaluation and application of the Murakami-Endo model

An inclusion analysis based on the statistics of extreme value (SEV) theory was performed. The statistics of extreme value method can be used to estimate the maximum defect, e.g., inclusion size in a large volume by extrapolating from the results of inclusion size investigations of the smaller areas or volumes.

A microsection perpendicular to the maximum principal stress was cut from the 12 mm diameter sections of the fatigue test specimens and it was polished with emery paper and mirror-finished. Nikon Epiphot microscope with a digital imaging system was used for the investigation. The size of the standard inspection area S_0 was 113 mm^2 ($\pi \cdot (12 \text{ mm})^2 / 4$) and 20 areas of S_0 were examined for each charge. The data of $\sqrt{area_{\max}}$, i.e., the size of the maximum inclusion in each standard inspection area was plotted on a statistics of extreme graph and the maximum inclusion sizes for different numbers of fatigue specimens were estimated. A schematic view of SEV method is presented in section 1.11 and the thorough procedure is described by Murakami et al. (1994).

Statistics of extreme value evaluation was also performed on inclusions at fracture origin sites, i.e., the fatigue crack initiating inclusions. This data was named

$\sqrt{area_{init.}}$ and it was also plotted on a statistics of extreme graph. The data of $\sqrt{area_{max}}$ and $\sqrt{area_{init.}}$ were plotted on the same statistics of extreme graph by using equation 31 to compare the distributions of maximum inclusion sizes on the polished microsections and of inclusions at the fatigue crack initiation sites.

4 RESULTS

4.1 Fatigue tests

The mean fatigue strength with the standard deviation, relationship between the fatigue strength and the ultimate tensile strength and the number of fatigue specimens where an inclusion had originated the fatigue crack of all fatigue failures are presented in Table 5.

Table 5. Fatigue test results of the materials.

Cast code	σ_w (MPa)	σ_w/R_m	Inclusion failures	Total no. failures	Total no. specimens
A1	421 ± 39	0,54	6	14	30
A2	421 ± 16	0,53	12	14	28
A3	395 ± 33	0,50	11	16	30
A4	410 ± 18	0,52	5	12	26
A5	434 ± 38	0,54	5	15	30
A6	404 ± 59	0,51	12	15	30
A7	414 ± 25	0,52	10	15	30
A8	417 ± 14	0,52	3	14	29
A9	421 ± 13	0,52	4	12	24
A10	400 ± 13	0,51	10	13	26
A11	405 ± 27	0,53	14	15	29
A12	453 ± 23	0,56	3	14	27
A13	429 ± 17	0,54	5	14	25
A14	424 ± 17	0,53	10	13	26
A15	423 ± 17	0,53	9	15	29
A16	414 ± 23	0,52	2	13	27
A17	444 ± 13	0,54	5	13	25
A18	429 ± 13	0,54	2	12	25
B1	465 ± 38	0,56	3	12	24
B2	453 ± 19	0,54	2	12	24
B3	421 ± 19	0,53	0	11	20
B4	443 ± 43	0,53	4	14	29

In Figure 25 fatigue test graph for cast A7 is presented. The horizontal line in Figure 25 stands for the fatigue limit with 50 % failure probability. The arrows in Figure 25 stand for the ran-out specimens. Fatigue test graphs for the other casts are presented in Appendix 1.

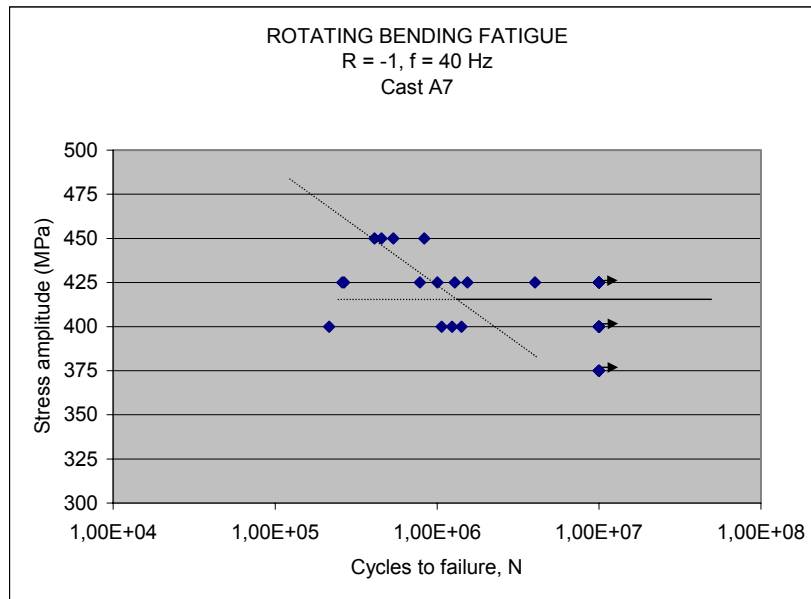


Figure 25. Fatigue test graph for Cast A7, $\sigma_w = 414 \pm 25$ MPa.

4.2 Residual stress measurements

A compressive residual stress of approximately 150-250 MPa longitudinal to the fatigue specimen axis (σ_x) on the surface of the fatigue test specimens was measured. The longitudinal residual stress component, i.e., the residual stress component having the major effect on the fatigue test results, decreased to 40-60 MPa after electropolishing the surface layer of approximately 50 μm and the residual stress distribution remained on the same level after electropolishing at least 250 μm from the surface. The residual stresses were, thus, assumed to be distributed linearly from the surface to the interior of 50 μm in depth and to stay at the same level deeper under the surface.

Table 6. Some examples of the results of the residual stress (MPa) measurements for specimens from different casts.

A11						
Measurement point	Section A		Section B		Section C	
	σ_x	σ_t	σ_x	σ_t	σ_x	σ_t
1	-217 ± 8	-301 ± 52	-232 ± 11	-311 ± 54	-209 ± 2	-313 ± 45
2	-202 ± 16	-305 ± 48	-220 ± 9	-306 ± 57	-238 ± 8	-311 ± 56
3	-210 ± 15	-303 ± 41	-215 ± 4	-299 ± 42	-238 ± 17	-346 ± 51
4	-257 ± 7	-328 ± 53	-238 ± 5	-323 ± 63	-201 ± 11	-334 ± 42
A13						
Measurement point	Section A		Section B		Section C	
	σ_x	σ_t	σ_x	σ_t	σ_x	σ_t
1	-179 ± 5	-330 ± 66	-179 ± 10	-338 ± 26	-184 ± 5	-359 ± 22
2	-199 ± 11	-333 ± 52	-169 ± 7	-345 ± 14	-176 ± 4	-336 ± 20
3	-175 ± 6	-326 ± 59	-161 ± 12	-331 ± 35	-194 ± 10	-349 ± 27
4	-152 ± 8	-338 ± 66	-162 ± 18	-340 ± 31	-200 ± 10	-369 ± 24

B1						
Measurement point	Section A		Section B		Section C	
	σ_x	σ_t	σ_x	σ_t	σ_x	σ_t
1	-205 ± 3	-324 ± 29	-204 ± 6	-338 ± 30	-155 ± 20	-333 ± 29
2	-219 ± 16	-356 ± 38	-204 ± 9	-338 ± 23	-209 ± 6	-347 ± 20
3	-201 ± 7	-365 ± 31	-185 ± 10	-343 ± 21	-157 ± 7	-326 ± 18
4	-193 ± 29	-353 ± 17	-185 ± 12	-349 ± 29	-154 ± 5	-282 ± 21
A11 (ran-out specimen, same specimen as above after 10^7 cycles)						
Measurement point	σ_x					
1	-207 ± 16					
2	-203 ± 14					
3	-194 ± 17					
4	-219 ± 13					

The residual stress measurements on ran out specimens indicated that there did not occur any notable residual stress relaxation resulting from the fatigue tests. It was, thus, assumed that the compressive residual stresses remained the same during the fatigue tests.

4.3 Surface roughness measurements

The measured surface roughness values of the specimens were approximately as follows:

$$R_a \approx 0,1 \dots 0,3 \mu\text{m},$$

$$R_z \approx 0,5 \dots 3 \mu\text{m}, \text{ and}$$

$$R_{\text{max}} \approx 1 \dots 6 \mu\text{m}.$$

Table 7 presents the results of the surface roughness measurements for some specimens of different casts.

Table 7. An example of the results of the surface roughness measurements for specimens of different casts.

A14	1	2	3	4	5	6	7	8	9	10	Mean	St. dev.
R _a	0,14	0,14	0,13	0,17	0,16	0,17	0,15	0,14	0,14	0,14	0,148	0,013
R _z	1,59	1,17	1,36	1,74	1,76	1,97	1,38	1,74	1,70	1,48	1,589	0,227
R _{max}	2,54	1,58	1,64	2,66	2,96	2,84	2,40	2,46	3,20	2,24	2,452	0,499
A15	1	2	3	4	5	6	7	8	9	10	Mean	St. dev.
R _a	0,12	0,16	0,17	0,11	0,16	0,17	0,10	0,13	0,18	0,13	0,143	0,027
R _z	1,30	1,66	2,31	1,05	1,87	2,42	1,24	1,58	2,18	1,38	1,699	0,454
R _{max}	1,75	2,60	2,78	1,62	2,78	3,36	2,14	2,24	2,72	2,04	2,403	0,511
A17	1	2	3	4	5	6	7	8	9	10	Mean	St. dev.
R _a	0,12	0,12	0,14	0,11	0,11	0,12	0,14	0,15	0,18	0,19	0,138	0,027
R _z	1,22	1,04	1,17	1,22	1,03	1,50	0,99	1,04	1,66	1,56	1,243	0,232
R _{max}	1,78	1,49	1,41	2,18	1,19	2,78	1,35	1,76	3,08	2,28	1,930	0,602
B1	1	2	3	4	5	6	7	8	9	10	Mean	St. dev.
R _a	0,08	0,12	0,12	0,08	0,10	0,11	0,10	0,08	0,11	0,10	0,100	0,015
R _z	0,57	1,16	1,24	0,69	0,71	1,40	1,74	0,77	1,28	0,84	1,040	0,360
R _{max}	0,67	1,66	1,78	0,83	0,75	3,12	5,52	1,10	1,76	1,00	1,819	1,416

The \sqrt{area} parameter model can also be applied with the surface roughness values of the fatigue specimens (e.g., Murakami, 2002). The equivalent defect size for the surface roughness, $\sqrt{area_R}$, when the stress intensity factor for a periodical surface crack with a depth of a and a pitch, i.e., width, of $2b$ is equal to the maximum value of the stress intensity factor along the crack front of a small surface crack:

$$\sqrt{area_R} / 2b \cong 2,97(a/2b) - 3,51(a/2b)^2 - 9,74(a/2b)^3 \text{ for } a/2b < 0,195 \quad (33)$$

$$\sqrt{area_R} / 2b \cong 0,38 \text{ for } a/2b > 0,195 \quad (34)$$

where $2b$ is the pitch of the surface roughness profile and a is the depth of the surface roughness profile, i.e., either the average roughness, R_a , or the maximum roughness of the surface profile, R_{max} . The pitch $2b$ has an effect on the fatigue crack initiation by the interference effect between the notches. In this study the values of the maximum roughness of the surface profile, R_{max} , were used as the depth a of the surface roughness profile. The definitions of the surface roughness parameters are shown in Figure 26.

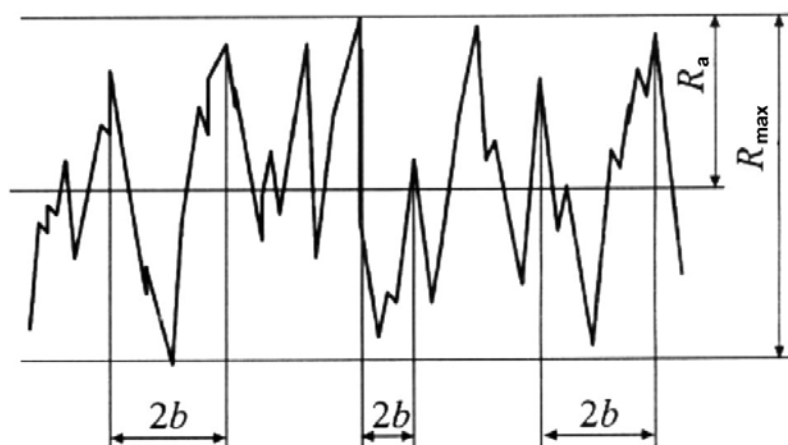


Figure 26. Definitions of the surface roughness parameters.

In the studied steels the measured surface roughness parameters were as follows: $2b \approx 40 \dots 120 \mu\text{m}$, a (i.e., R_{max}) $\approx 1 \dots 6 \mu\text{m}$. With $a = 6 \mu\text{m}$ that results in $\sqrt{\text{area}_R} \approx 13 \dots 17 \mu\text{m}$ and with the average value of the pitch, $2b = 80 \mu\text{m}$, we get $\sqrt{\text{area}_R} \approx 16 \mu\text{m}$. Parameter $2b$ was determined from the optical microscope images of the fatigue test specimen surfaces.

4.4 Inclusion analyses

Results of the inclusion analyses according to DIN 50 602 and SFS-ENV 10247 methods are presented in Table 8.

Table 8. Results of the inclusion analyses according to DIN 50 602 and SFS-ENV 10247 methods.

Cast code	SFS-ENV 10247						DIN 50 602	
	3...5,5 (μm)	...11 (μm)	...22 (μm)	...44 (μm)	...88 (μm)	...176 (μm)	K ₀₃	K ₀₄
A1	1063	530	168	25	1	-	115	77
A2	1189	616	111	12	-	-	41,7	23,2
A3	1501	610	23	2	-	-	43	23
A4	1360	722	112	23	-	-	36,7	16,7
A5	1317	660	93	8	-	1	72	60
A6	1390	351	32	-	-	-	48	23
A7	1297	365	36	2	-	-	18	13
A8	1115	597	121	13	-	-	38,3	28,3
A9	1163	594	54	-	-	-	28,3	13,3
A10	1203	558	164	1	1	-	75	53
A11	526	161	13	1	-	-	40	20
A12	1515	680	32	1	-	-	38,3	10
A13	827	131	12	-	-	-	28,3	6,7
A14	1335	490	77	4	-	-	83,3	26,7
A15	944	262	23	-	-	-	43,3	16,7
A16	1295	676	55	-	-	-	33,3	20
A17	2012	836	59	2	-	-	30	10
A18	1972	584	24	-	-	-	20	0
B1	954	19	-	1	-	-	0	0
B2	964	559	40	-	-	-	26,7	13,3
B3	839	413	54	-	-	-	11,7	3
B4	1432	272	-	-	-	-	0	0

4.5 Ultrasonic testing in immersion

Results of the ultrasonic testing in immersion are presented in Table 9.

Table 9. Results of the ultrasonic testing in immersion.

Cast code	Side	Number of defects				Specimen volume (dm ³)	Defects (n)
		C1 (40-100 μm)	C2 (100-200 μm)	C3 (> 200 μm)	Long (length > 3 mm)		
A1	1	4				0,78141	47
	2	19					
	3	3					
	4	20			1		
A2	1	7				0,80724	20
	2	4					
	3	4					
	4	5					
A3	1	55	2	2	1	0,78141	132
	2	5					
	3	53	5	2			
	4	8					
A4	1	20				0,83349	53
	2	4			1		
	3	21		1			
	4	7			1		
A5	1	1				0,80724	6
	2						
	3	2					
	4	3					

A6	1						
	2						
	3						
	4						
A7	1	10				0,83349	20
	2						
	3	10					
	4						
A8	1	1				0,83349	3
	2	1					
	3	1					
	4						
A9	1	5	1			0,756	11
	2	0					
	3	3					
	4	2					
A10	1	13				0,80724	33
	2						
	3	18					
	4	2					
A11	1	14			1	0,83349	41
	2	1					
	3	15		2			
	4	7			1		
A12	1	4			2	0,80724	19
	2	2					
	3	1			1		
	4	7			2		
A13	1					0,83349	3
	2	2					
	3						
	4	1					
A14	1	28				0,80724	79
	2	5					
	3	38					
	4	8					
A15	1	3				0,83349	6
	2	1					
	3	1					
	4	1					
A16	1						
	2						
	3						
	4						
A17	1					0,83349	4
	2	1					
	3	1					
	4	2					
A18	1	2				0,829521	3
	2						
	3						
	4	1					
B1	1	1				0,83349	7
	2	1					
	3	1					
	4	4					
B2	1					0,80724	3
	2	1					
	3						
	4	2					
B3	1	1				0,80724	1
	2						
	3						
	4						
B4	1	1				0,837459	7
	2	2					
	3	3					
	4	1					

4.6 SEM and EDS investigations

In the casts with large calcium treatment, the fatigue cracks initiated mostly from the surface inclusions and the inclusions near the surface of the fatigue specimen. In the casts with small calcium treatment, the fatigue cracks initiated mostly at surface discontinuities, i.e., at the bottom of the scratch marks, but also from the surface inclusions and inclusions near the surface of the fatigue specimen. According to the EDS analyses, the fatigue crack initiating inclusions were mainly globular calcium aluminates encapsulated in calcium sulfides and contained small amounts of silicon and/or magnesium. A few fatigue crack initiating inclusions contained also carbon together with silicon, and in a few cases a pure aluminium oxide had originated the fatigue crack, see Figure 27. Fatigue cracks initiated either from the interface between the inclusion and the matrix or through cracking of the inclusion, see Figures 28 and 29.

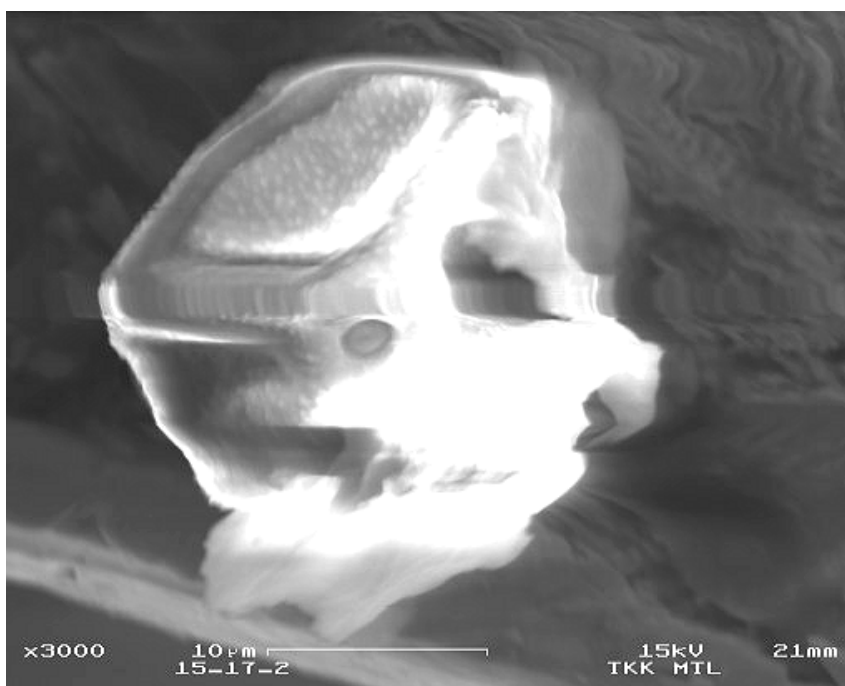


Figure 27. A SEM image of a fatigue crack initiating aluminium oxide inclusion on the fracture surface of a fatigue specimen of Cast A2. $\sqrt{area} = 23 \mu\text{m}$, $h = 20 \mu\text{m}$. Rotating bending, $R = -1$, $\sigma = 425 \text{ MPa}$, $N_f = 7,37 \times 10^5$.

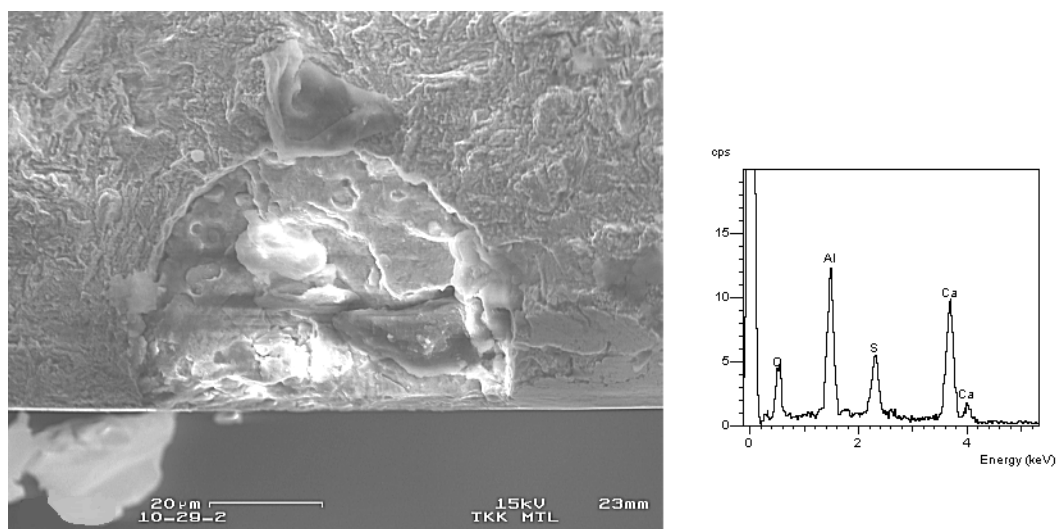


Figure 28. A SEM image of a typical cracked globular calcium aluminate inclusion on the fracture surface of a fatigue specimen of Cast A1. $\sqrt{area} = 52 \mu\text{m}$, composition: Ca-S-Al-O. Rotating bending, $R = -1$, $\sigma = 450 \text{ MPa}$, $N_f = 6,13 \times 10^5$.

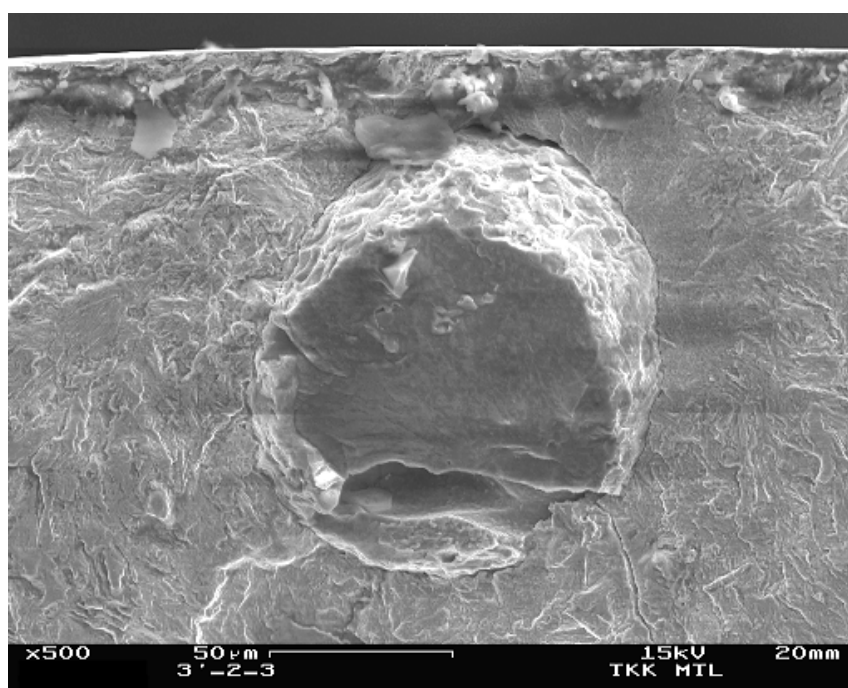


Figure 29. A SEM image of a typical large cracked globular calcium aluminate inclusion on the fracture surface of a fatigue specimen of Cast B1. $\sqrt{area} = 104 \mu\text{m}$, $h = 120 \mu\text{m}$, composition: Ca-S-Al-O-Mg-Si. Rotating bending, $R = -1$, $\sigma = 450 \text{ MPa}$, $N_f = 6,71 \times 10^5$.

Cracks which had initiated from surface inclusions and stopped propagating after growing some distance, i.e., non-propagating cracks, were observed on the surfaces of the fatigue test specimens, see Figure 30.

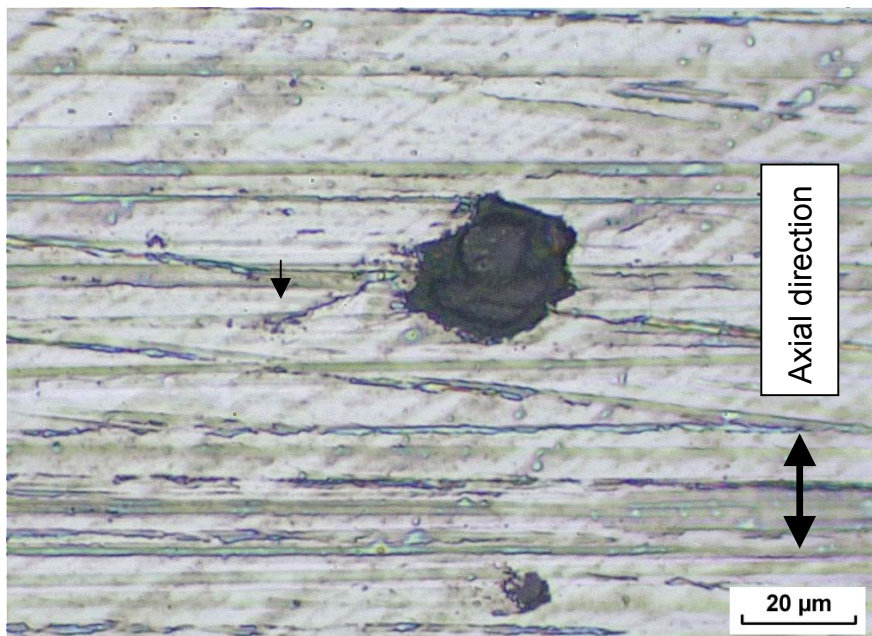


Figure 30. Crack initiation from a surface inclusion, and non-propagation behaviour, Cast A11, fatigue test specimen no 2.

In Figure 31 a SEM image and the chemical composition mapping images of a typical calcium aluminate inclusion with magnesium encapsulated in calcium sulfide on the fracture surface of a fatigue specimen of Cast A11 are presented. It can be seen that the fatigue crack has initiated from the interface between the inclusion and the matrix, and a part of the calcium sulfide shell has detached exposing the inner core which consists of aluminium, oxygen, calcium and magnesium, being possibly $\text{CaO-Al}_2\text{O}_3\text{-MgO}$.

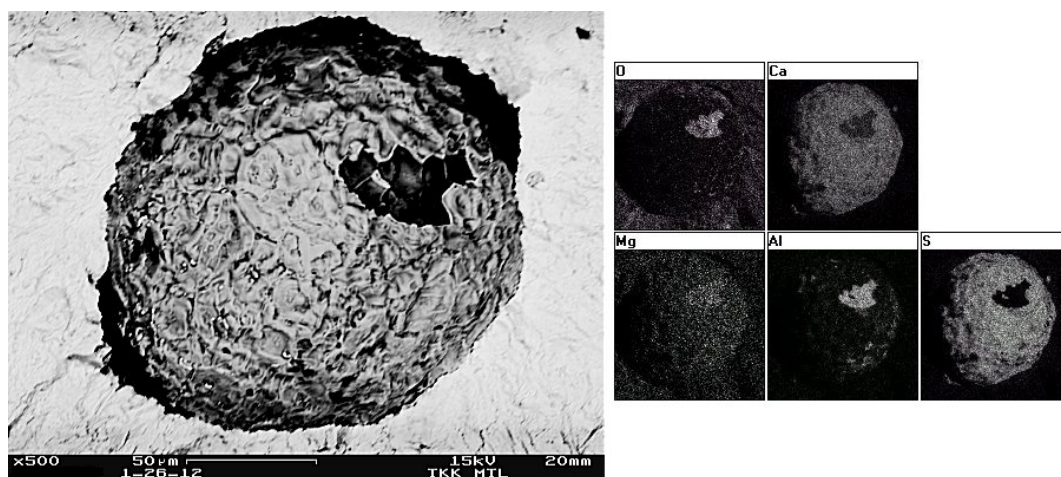


Figure 31. A backscattering SEM image of a typical large globular calcium aluminate inclusion with magnesia encapsulated in calcium sulfide on the fracture surface of a fatigue specimen of Cast A11. $\sqrt{area} = 144 \mu\text{m}$, $h = 160 \mu\text{m}$. Rotating bending, $R = -1$, $\sigma = 400 \text{ MPa}$, $N_f = 4,72 \times 10^6$.

In Figure 32 a SEM image of typical fatigue crack initiation from the bottom of a surface scratch on the surface of a fatigue specimen of Cast A2 is presented.

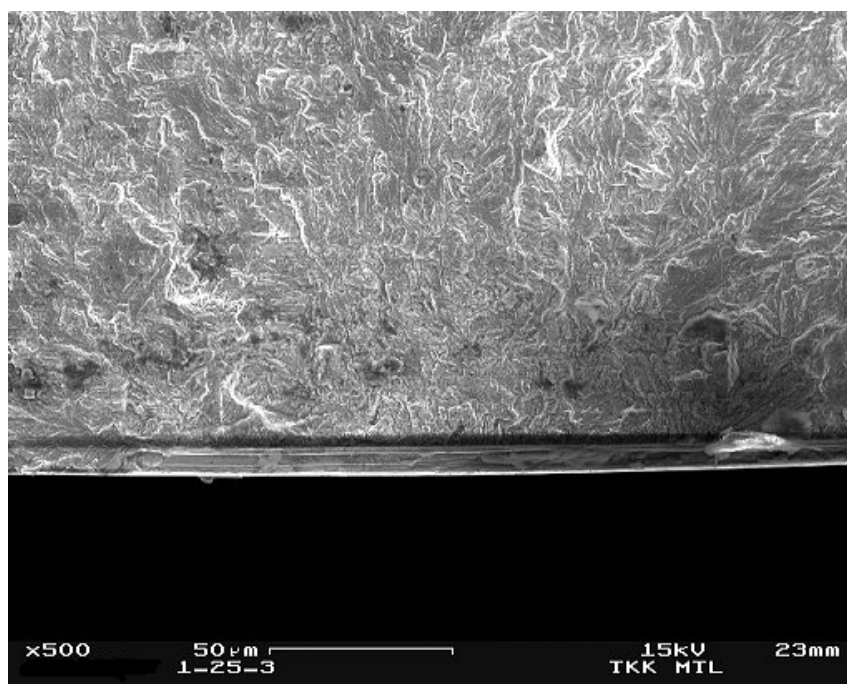


Figure 32. Fatigue crack initiation from the bottom of a surface scratch on the surface of a fatigue specimen of Cast A11. Rotating bending, $R = -1$, $\sigma = 425 \text{ MPa}$, $N_f = 1,98 \times 10^6$.

In Figure 33 a SEM image of a typical globular calcium aluminate inclusion with magnesia encapsulated in calcium sulfide on a polished microsection of Cast A2 is presented.

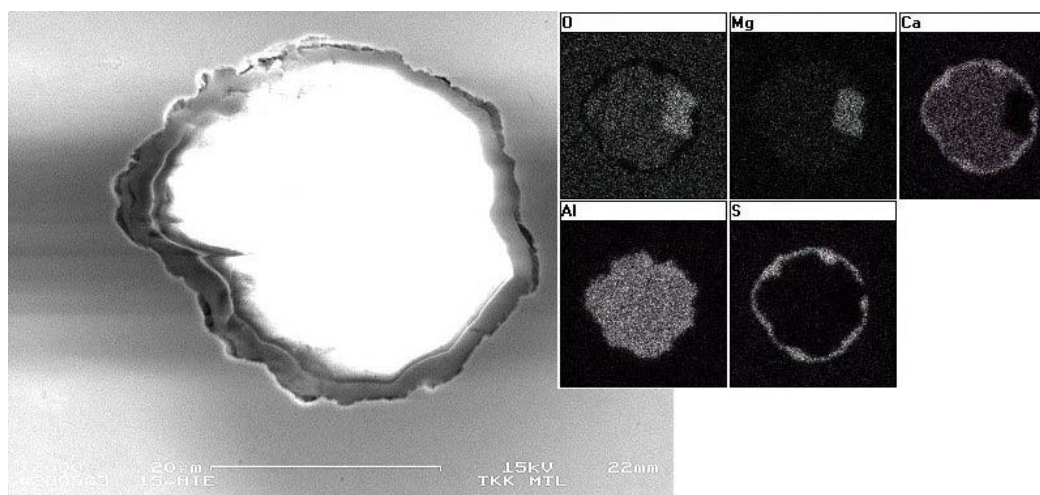


Figure 33. A globular calcium aluminate inclusion with magnesia encapsulated in calcium sulfide, polished microsection of Cast A2, $\sqrt{area} = 30,9 \mu\text{m}$.

The fatigue crack initiating inclusion data, i.e., the type, size (\sqrt{area}), location and chemical composition of the inclusions which originated fatigue cracks and fatigue limit predicted by equation 20 of Murakami et al. (1990) versus the stress at the fatigue crack initiation site are presented in Table 10 for Cast A11. It has to be noted, that for surface inclusions the $\sqrt{area_1}$ values have been used to represent the values of \sqrt{area} , see Figure 24. In the calculations by equation 20 it was assumed that there was a compressive residual stress of 200 MPa present at the surface of the fatigue specimens.

Table 10. Size, location and chemical composition of inclusions and fatigue limit predicted by equation 20 of Murakami et al. (1990) for Cast A11.

σ	N_f	HV	\sqrt{area}	h	Composition	R	σ'	σ_w	σ'/σ_w	ΔK	Cracking type of inclusion	Shape of inclusion
450	6,11E+05	256	44,9	0	Ca-S-Al-O-Mg-Si	-2,60	450	330	1,362	6,9	cracked	globular
425	7,45E+05	290	39,9	25*	Ca-S-Al-O-Mg-Si	-1,83	422	342	1,236	6,1	non-cracked	globular
450	3,23E+05	314	45,6	0	Ca-S-Al-O-Si	-2,60	450	382	1,178	7,0	non-cracked	globular
425	4,05E+05	261	37,6	0	Ca-S-Al-O-Mg-Si	-2,78	425	349	1,216	6,0	non-cracked	globular
425	3,51E+06	294	55,8	0	Ca-S-Al-O-Mg-Si	-2,78	425	357	1,192	7,3	cracked	globular
425	1,01E+06	278	34,6	0	Ca-S-Al-O-Mg-Si	-2,78	425	370	1,148	5,8	cracked	globular
425	6,40E+05	281	35,1	0	Ca-S-Al-O-Si	-2,78	425	373	1,140	5,8	non-cracked	globular
400	1,35E+06	279	31,7	0	Ca-S-Al-O-Si	-3,00	400	383	1,045	5,2	non-cracked	globular
400	1,18E+06	274	27,4	15*	Ca-S-Al-O-Mg-Si	-2,27	398	362	1,100	4,8	non-cracked	globular
375	2,13E+06	292	82,9	70	Ca-S-Al-O-Si	-1,31	368	320	1,151	5,9	non-cracked	globular
400	6,94E+05	323	101,3	0	Ca-S-Al-O-Si	-3,00	400	351	1,140	9,3	non-cracked	globular
425	6,97E+05	314	51,3	20*	Ca-S-Al-O-Mg	-1,98	423	352	1,200	7,0	non-cracked	angular
400	4,72E+06	296	144,4	160	Ca-S-Al-O-Mg	-1,29	383	293	1,305	8,2	non-cracked	globular
425	6,33E+05	275	36,9	0	Ca-S-Al-O-Mg-Si	-2,78	425	364	1,167	5,9	non-cracked	globular

σ = Nominal stress at specimen surface;

N_f = Cycles to failure;

HV = Vickers microhardness near the inclusion;

\sqrt{area} = Square root of projection area of inclusion (μm);

h = Distance from surface (μm);

*: Inclusion is located just below specimen surface;

R = Stress ratio at inclusion;

σ' = Stress at inclusion;

σ_w = Fatigue limit at inclusion calc. by equation 20.

ΔK = Stress intensity factor range at inclusion ($\text{MPa}\cdot\text{m}^{1/2}$), calculated by equations 5 and 6, where $\sigma_0 = 2 \cdot \sigma'$

In Figure 34 a modified S-N diagram, i.e., the relationship between the ratio of stress at inclusion, σ' , to estimated fatigue limit at inclusion, σ_w , and cycles to failure, N, for all 22 casts are presented.

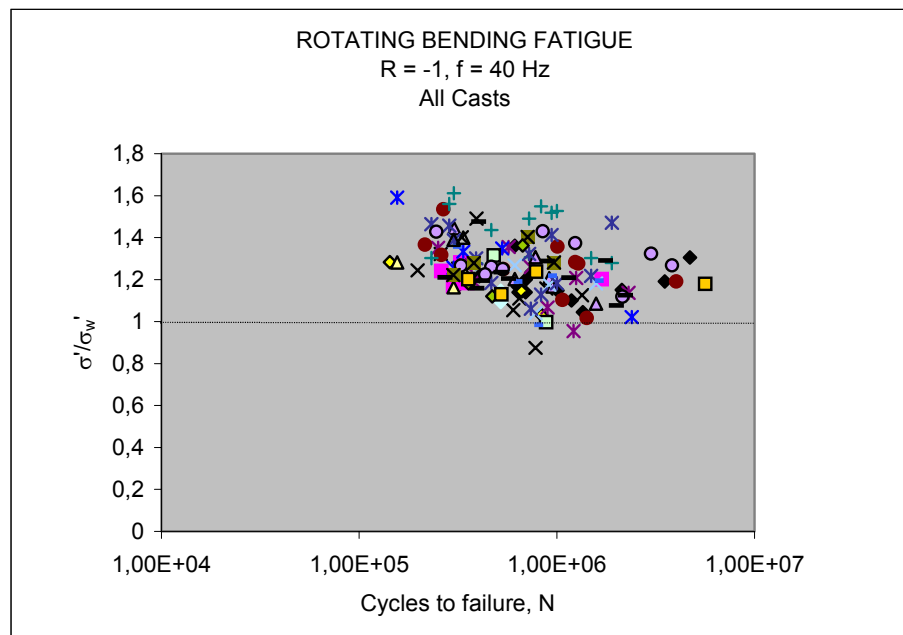


Figure 34. A modified S-N diagram for all 22 casts. The relationship between the ratio of stress at inclusion, σ' , to estimated fatigue limit at inclusion, σ_w , and cycles to failure, N.

Figure 34 shows a trend where greater values of σ'/σ_w' result in shorter fatigue lives, which sounds reasonable. Only two data points are located below the line where $\sigma'/\sigma_w' < 1$, showing the accuracy and conservativeness of the predictions obtained by equation 20. The data of all inclusions which initiated the fatigue cracks and the calculations which were used for Figure 34 are presented in Appendix 2.

4.7 Statistics of extreme value evaluation and application of the Murakami-Endo model

Inclusions at polished microsections were analyzed by the SEV method. In Figure 35 optical microscope images of typical largest inclusions at standard inspection area are presented.

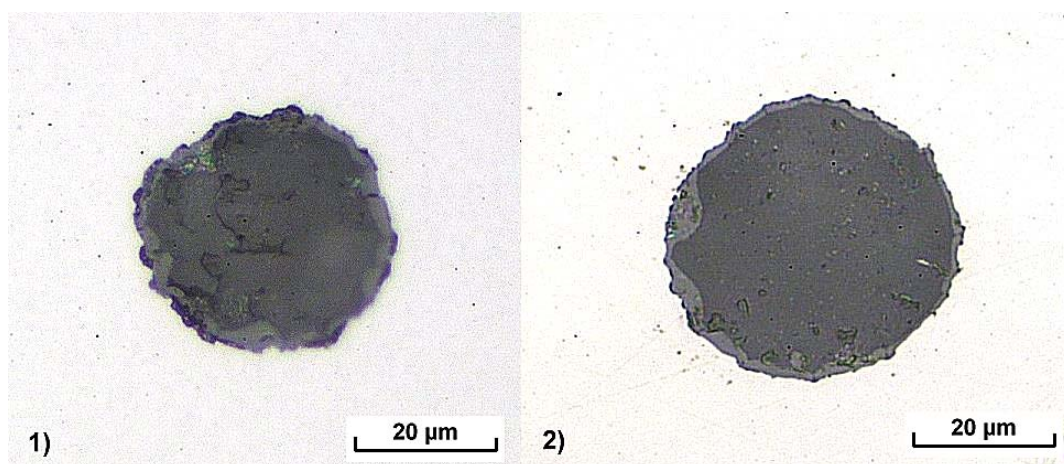


Figure 35. Optical microscope images of 1) the same inclusion as in Figure 33 and of 2) another inclusion in the same cast; $\sqrt{area} = 30,9 \mu\text{m}$ and $35,3 \mu\text{m}$, respectively.

The maximum inclusion size, $\sqrt{area_{max}}$, present in a definite number of specimens was predicted for each cast. In the rotating bending fatigue loading, the initiation of the fatigue cracks takes most likely place at the surface and in the vicinity of the surface. In Murakami et al. (1994) it was considered that in the rotating bending fatigue loading the critical part of the specimen is that where $\sigma \geq 0,9\sigma_0$, σ_0 being the nominal stress, i.e., $h_s \leq 0,05d$, h_s being the control depth for the prospective fatigue failure. The control volume for the prospective fatigue failure, V_s , can, thus, be calculated from equation 35:

$$V_s = 0,05\pi d^2 l \text{ (mm}^3\text{)} \quad (35)$$

where d = diameter of the round bar (mm) and
 l = length of the round bar.

Thus, the control depth for the prospective fatigue failure was $h_s = 0,05 \cdot 7,52 \text{ mm} = 376 \text{ }\mu\text{m}$. The control volume for the prospective fatigue failure in one specimen was $V_s = 0,05 \cdot \pi \cdot (7,52)^2 \cdot 70 = 621,8 \text{ mm}^3$ and in a fatigue test set of 30 specimens it was $30 \cdot 621,8 \text{ mm}^3 = 18654,1 \text{ mm}^3$. When the locations of the fatigue crack initiation sites in all fatigue test specimens were investigated, the control volume for prospective fatigue failure calculated by equation 35 can be considered reasonable, see Figure 36.

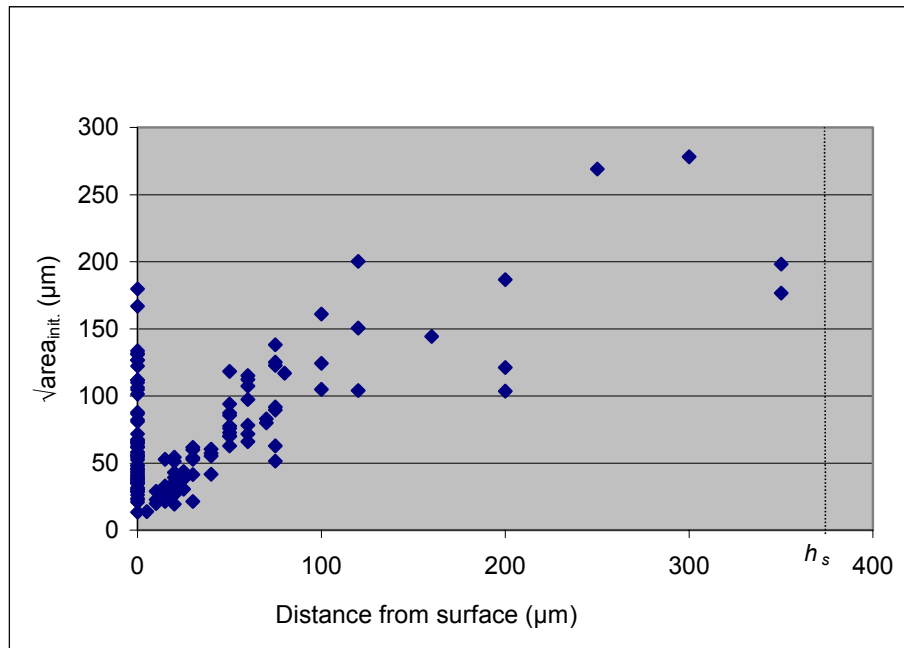


Figure 36. The location of the fatigue crack initiating inclusions versus inclusion size ($\sqrt{area_{init.}}$).

The maximum inclusion sizes for each cast predicted by the SEV method ($\sqrt{area_{max}}$) and the real maximum inclusion sizes, i.e., the sizes of the largest inclusions at the fracture surfaces ($\sqrt{area_{init.max}}$) are presented in Table 11. The R-squared values of the linear trendlines for $\sqrt{area_{max}}$ calculated by Excel program are also presented in Table 11. The linear trendlines calculated by Excel program differ only slightly from the trendlines which are presented in Figure 37 and Appendix 3 and which are calculated by the equations presented in Section 1.11. Value R^2 describes the linearity of the data points of $\sqrt{area_{max}}$, i.e., how well these data points follow the statistical distribution of the extreme values.

Figure 37 shows plots of cumulative probability of $\sqrt{area_{max}}$ versus $\sqrt{area_{init.}}$ in the probability graph of extreme value for Cast A13. Extreme value distribution of inclusions at the fatigue crack initiation sites is drawn into the same graph with the inclusions at the standard inspection areas, S_0 , by converting the data to standard

control volume $V_0 = h_0 \times S_0$ by using equation 30. It has to be noted, that for globular surface inclusions the $\sqrt{area_2}$ values have been used to represent the values of $\sqrt{area_{init}}$ in these combined probability graphs, see Figure 24, to express the real maximum inclusion sizes in the control volume of the fatigue specimens. Probability graphs for the other casts are shown in Appendix 3.

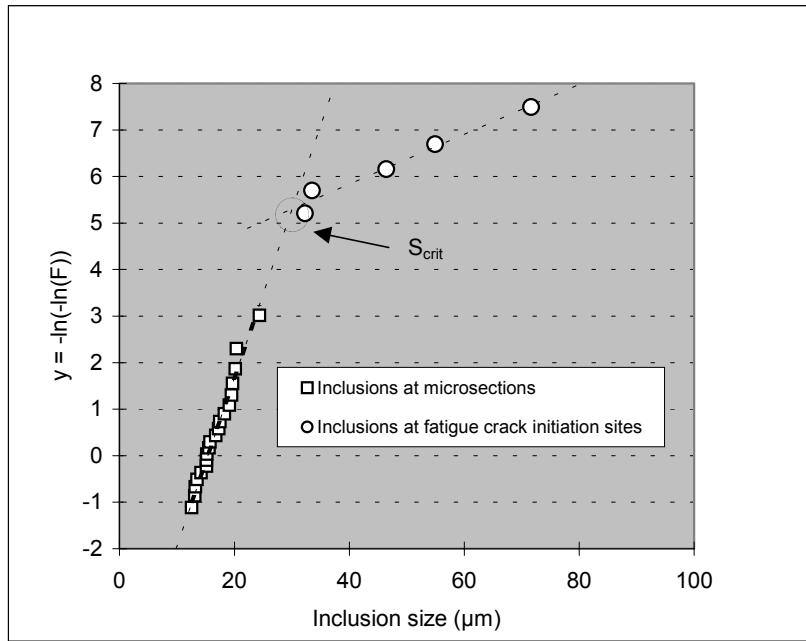


Figure 37. Plots of cumulative probability of $\sqrt{area_{max}}$ versus $\sqrt{area_{init}}$ in the probability graph of extreme value for Cast A13. $S_0 = 113 \text{ mm}^2$, $n = 20$.

The minimum control area, S_{crit} , needed for detecting the second type of defects (inclusions responsible for fatigue failure) was estimated by the intersection of the two lines corresponding to the extreme value distributions of $\sqrt{area_{max}}$ and $\sqrt{area_{init}}$. S_{crit} was calculated from equation 36:

$$S_{crit} = T \cdot S_0 \quad (36)$$

From equation 24 we get:

$$T = \frac{1}{1 - e^{-e^{-y}}}, \text{ y being the value of y at the intersection of the two lines.}$$

Thus, we get: $S_{crit} = 201 \cdot S_0 = 201 \cdot 113 \text{ mm}^2 = 22695 \text{ mm}^2$. The S_{crit} values for all casts are presented in Table 11.

Table 11. The maximum inclusion sizes predicted by the SEV method and the largest inclusions at the fracture surfaces. S_{crit} is the critical control area estimated by the intersection of the lines corresponding to the extreme value distributions of $\sqrt{area_{max}}$ and $\sqrt{area_{init.}}$. R^2 describes how well the data points of $\sqrt{area_{max}}$ follow the statistical distribution of the extreme values.

Cast code	$\sqrt{area_{max}}$ (μm)	$\sqrt{area_{init.}}$ (μm)	R^2	S_{crit} (mm^2)
A1	64	87	0,9588	16827*
A2	128	187	0,8959	33829*
A3	65	298	0,8745	19541*
A4	56	92	0,9554	37380*
A5	65	70	0,985	41306*
A6	92	200	0,9715	8385
A7	76	269	0,9706	27707*
A8	76	71	0,8353	68065*
A9	43	150	0,9681	27707*
A10	94	227	0,7341	8812
A11	80	144	0,9487	45644*
A12	45	72	0,928	41306*
A13	41	72	0,9744	22695
A14	51	127	0,941	30615*
A15	46	111	0,9506	21591*
A16	52	79	0,9723	33829*
A17	35	161	0,9679	37380*
A18	53	24	0,9306	**
B1	48	158	0,8829	16827
B2	43	126	0,9346	39294
B3	27	-	0,9609	***
B4	40	57	0,9694	23855

* The distributions of inclusions at microsections and inclusions at the fatigue crack initiation sites overlapped partly each other

** All inclusions at fatigue crack initiation sites were smaller than inclusions at microsections

*** No inclusion originated fatigue failures were detected

The upper and lower bounds of fatigue strength were predicted for each cast by equations 14 and 20, respectively. Figure 38 shows the predictions of the upper and lower bounds of the fatigue strength for 30 specimens of cast A11 (see Appendix 4 for predictions for the other casts) calculated by equation 20 ($C = 1,41$) and the experimental results. For ran-out specimens the hardness values presented in Table 4 were used.

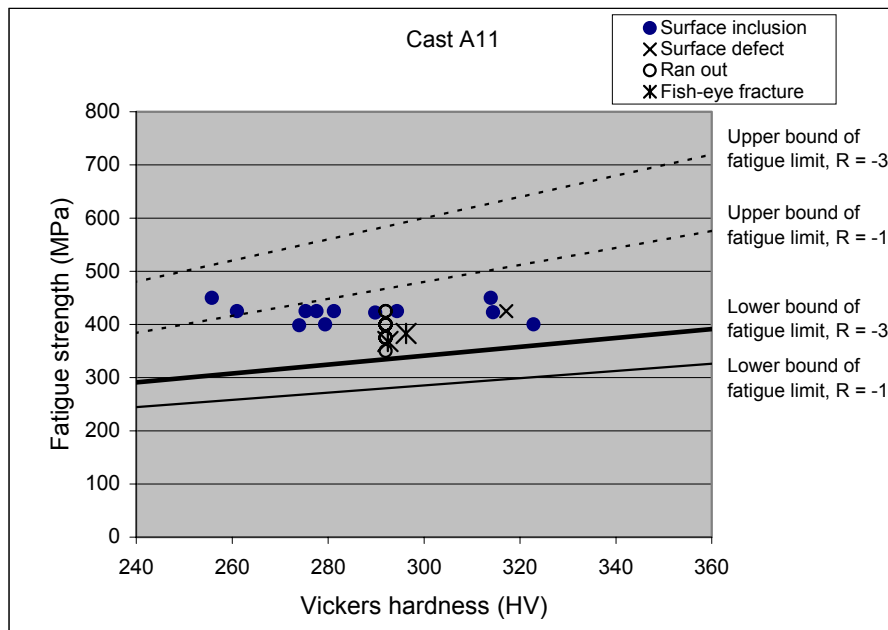


Figure 38. Predictions of the upper and lower bounds of the fatigue strength for 30 specimens of Cast A11.

The lower bound of fatigue strength is the nominal stress amplitude when the largest inclusion to be expected to exist in 30 fatigue test specimens is located in the critical site, i.e., just under the fatigue test specimen surface. Since the value of the residual stress at the fatigue crack initiation site of each specimen is not always the same, the stress ratio, R , is a variable which affects the predictions of the lower bound of the fatigue strength. According to the calculations of the lower bound of the fatigue limit, the stress ratio $R \sim -3$ at the lowest because of the compressive residual stresses when the fatigue crack initiating inclusion was located in the specimen surface. When the fatigue crack initiating inclusion was located under the surface, the stress ratio $R \sim -1$ at the highest because the compressive residual stresses exist only until $50 \mu\text{m}$ in depth, see Section 4.2 and Appendix 2. Thus, the lower bounds of fatigue strength for the stress ratios $R = -1$ and $R = -3$ between which the stress ratios for all cases are situated are presented in Figure 38. Since the stress ratio has also an effect on the upper bound of fatigue strength, the Goodman relation (e.g., Hertzberg, 1996) is applied in the calculation of the upper bound of the fatigue strength:

$$\sigma_{w0, R \neq -1} = \sigma_{w0} \left(1 - \frac{\sigma_m}{R_m}\right) \quad (37)$$

where $\sigma_{w0, R \neq -1}$ = fatigue strength when $R \neq -1$

σ_m = mean stress

σ_{w0} = ideal fatigue strength when $R = -1$, i.e., 1,6HV

R_m = tensile strength

4.8 Multiple linear regression

Multiple linear regression enables the solving of fitting problems involving more than one independent variable. In multiple linear regression the least square method is used in estimating the regression coefficients of the independent variables. The equations obtained from multiple linear regression analyses are of type $y = a + b_1x_1 + \dots + b_{n-1}x_{n-1} + b_nx_n$, where y is the value of the dependent variable, a is constant, $x_1 \dots x_n$ are the values of the independent variables and $b_1 \dots b_n$ are the regression coefficients. The squared correlation coefficient, R^2 , describes the “goodness of fit” of the trendline drawn by the equation. To find out if the model, i.e., equation as a whole and the single values of the regression coefficients have statistically significant predictive capabilities, an analysis of variance of the data has to be performed. As a rule of thumb it can be stated that usually when the number of independent variables in the multiple linear regression analysis increases, also the value of R^2 increases, but the statistical significance of the whole model and the single regression coefficients decreases. This effect is emphasized especially in the cases when the number of data samples is small and the variance between the data samples is small. The details of the multiple linear regression method may be found, e.g., in Miller et al. (1990).

Multiple linear regression calculations were performed to clarify if any correlations could be found between the chemical composition and the inclusion analysis results (by DIN 50 602 and SFS-ENV 10247 methods and ultrasonic testing in immersion) and the fatigue properties and the machinability of the casts. Special attention was paid to particular alloying elements, which have an important role in the calcium treatment of steel, i.e., sulfur, aluminium, oxygen and calcium. $\sqrt{area_{init.max}}$, $\sqrt{area_{init.mean}}$ (the arithmetic mean of the sizes of the inclusions at fatigue crack initiation sites), v_{15} and σ_w/R_m ratio were used as the dependent variables in the multiple linear regression calculations. The best fitting results of the multiple linear regression analyses are presented in Figures 39-43.

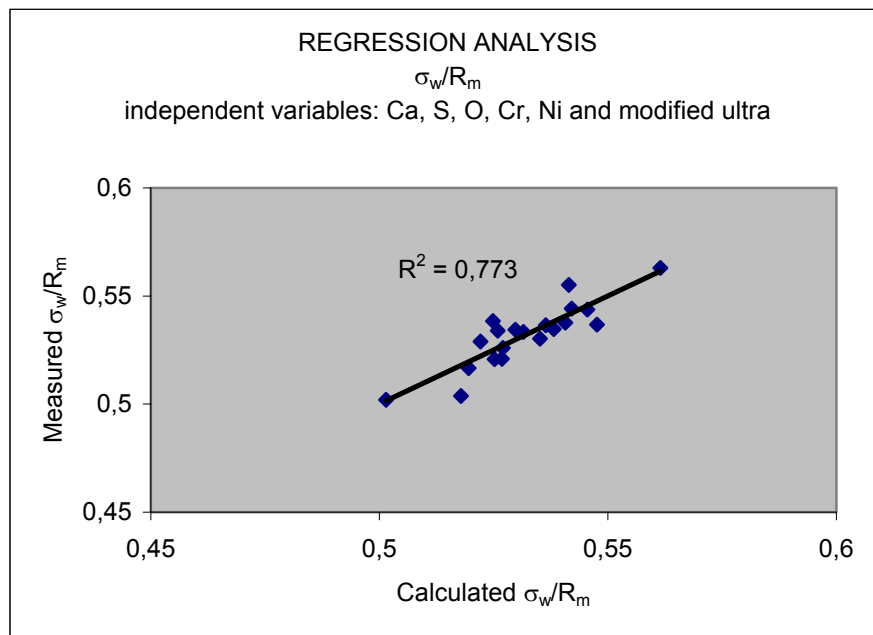


Figure 39. The correlation between particular alloying elements (calcium, sulfur, oxygen, chromium and nickel) combined with the modified results of the ultrasonic testing in immersion (inclusions larger than 200 μm are not taken into account) and σ_w/R_m ratio calculated by multiple linear regression.

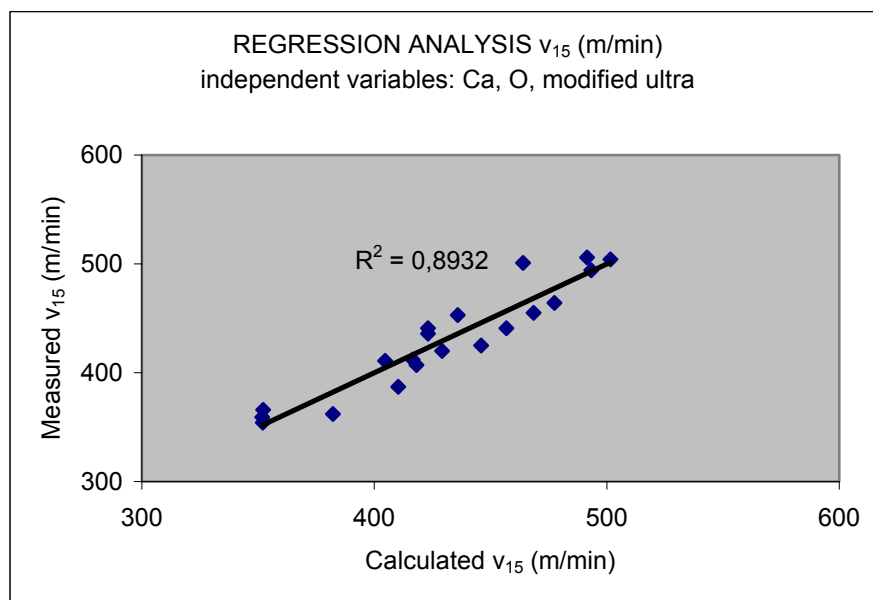


Figure 40. The correlation between particular alloying elements (calcium and oxygen) combined with the modified results of the ultrasonic testing in immersion (inclusions larger than 200 μm are not taken into account) and v_{15} calculated by multiple linear regression.

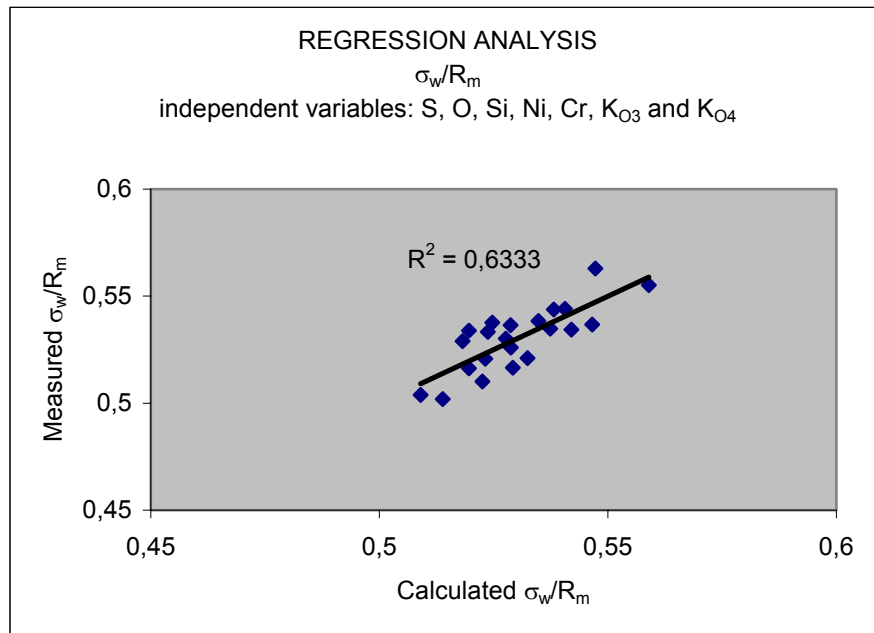


Figure 41. The correlation between particular alloying elements (sulfur, oxygen, silicon, nickel and chromium) combined with the SEP results and σ_w/R_m ratio calculated by multiple linear regression.

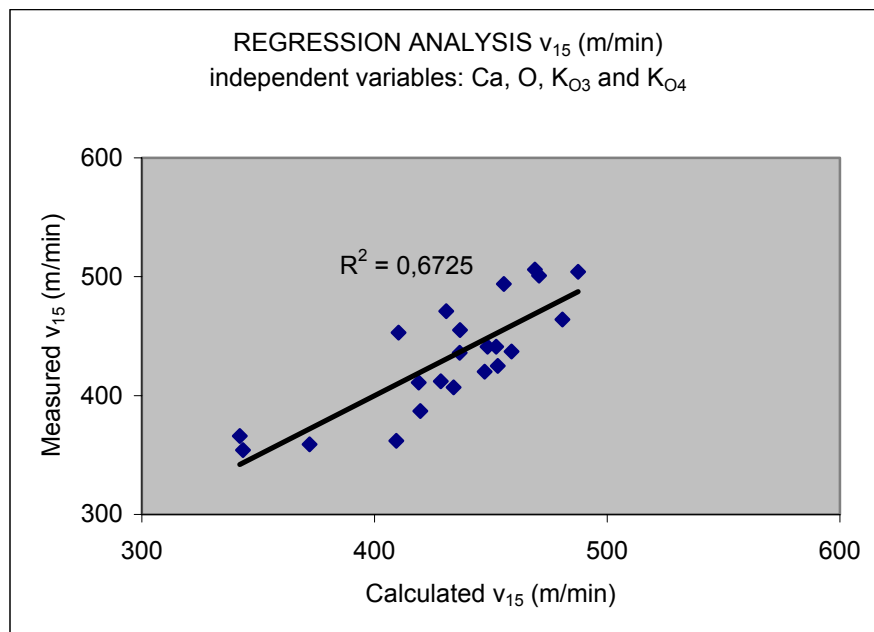


Figure 42. The correlation between particular alloying elements (calcium and oxygen) combined with the SEP results and v_{15} calculated by multiple linear regression.

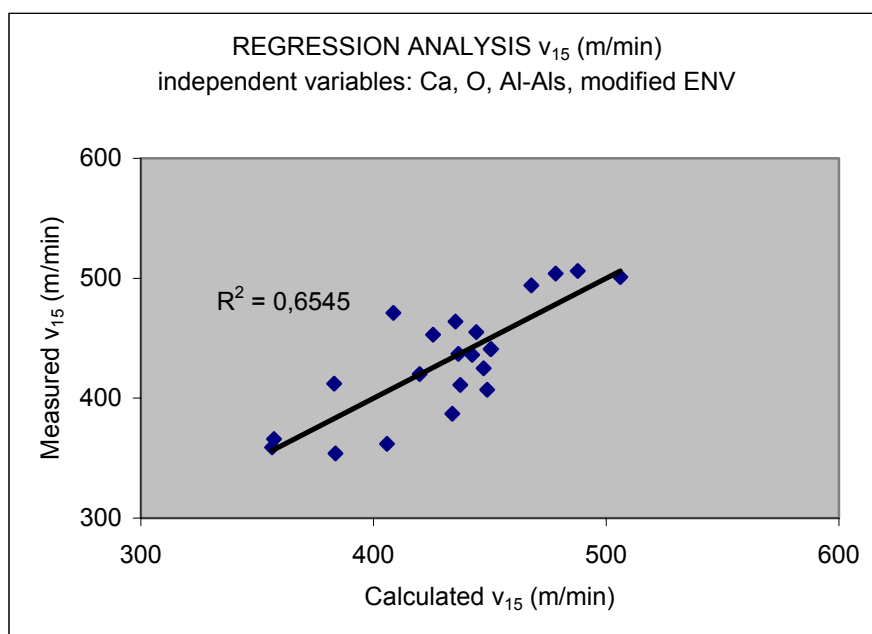


Figure 43. The correlation between particular alloying elements (calcium, oxygen and insoluble aluminium) combined with the modified ENV results (inclusions larger than $22\ \mu\text{m}$ not taken into account) and v_{15} calculated by multiple linear regression.

5 DISCUSSION

5.1 Fatigue tests

There were no significant differences between the relations between the average fatigue strength and the tensile strength values of the casts with the large amount of calcium injection and the casts with the small amount of calcium injection, even though the range of σ_w/R_m ratios of the casts with the large amount of calcium injection was larger than that with the casts with the small amount of calcium injection. The σ_w/R_m ratios of the calcium treated casts with the large amount of calcium injection were between 0,50...0,56 and the σ_w/R_m ratios of the calcium treated casts with the small amount of calcium injection were between 0,53...0,56. The relationship between the average fatigue strength and the tensile strength is presented in Figure 44.

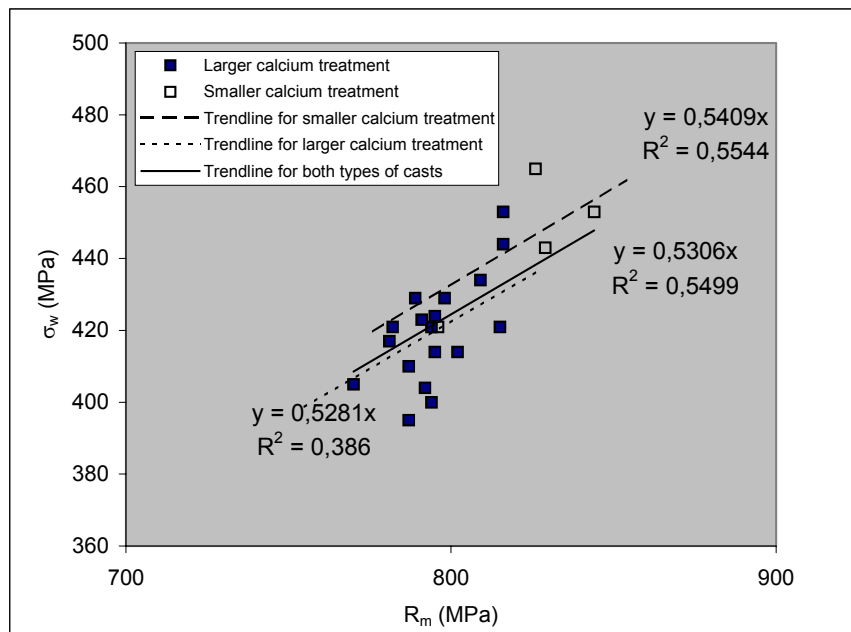


Figure 44. The relationship between the average fatigue strength and the tensile strength of all casts.

In Figure 45 the relationship between the average defect size, i.e., the arithmetic mean of the sizes of the inclusions at fatigue crack initiation sites ($\sqrt{area_{init.mean}}$) and the σ_w/R_m ratio is presented. The trend of the data in Figure 45 indicates that the σ_w/R_m ratio appears almost independent of defect size in the region where the average fatigue crack initiating inclusion size is less than $\sim 70-90 \mu\text{m}$. In the region where the average defect size is larger than $\sim 70-90 \mu\text{m}$ the σ_w/R_m ratio tends to decrease as the average defect size increases. It has to be noted that because of the small variance between the casts the estimated defect size determining the average fatigue limit is only an estimate.

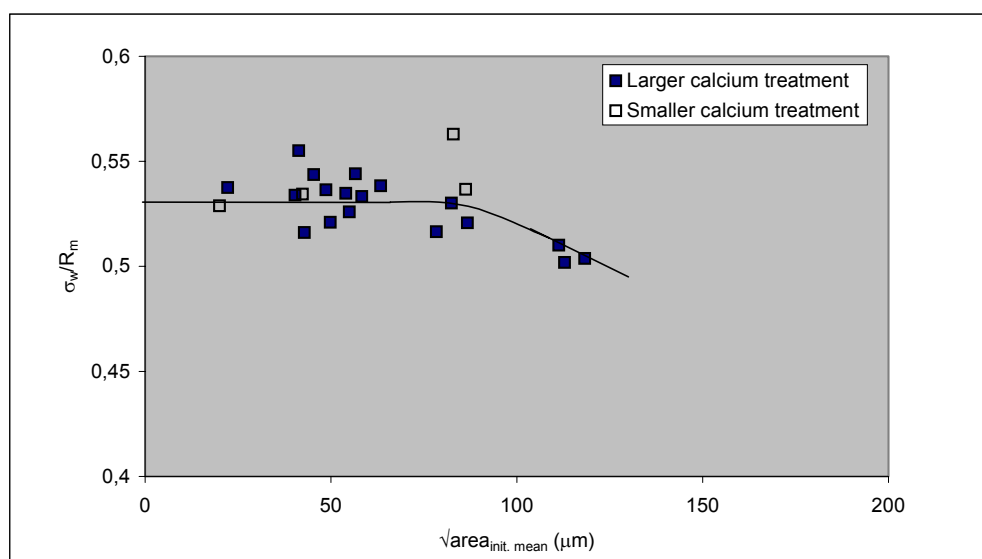


Figure 45. Dependence of σ_w/R_m ratio on $\sqrt{area_{init.mean}}$, i.e., the average crack initiating inclusion size.

It is well known that an uncontrolled calcium treatment may result in unwanted, large globular inclusions, which result in degraded fatigue strength and increase in the scatter of the fatigue strength. In some casts the average fatigue strength had a considerable scatter when compared with the other casts. This may indicate that there were differences between the inclusion distributions between the casts.

5.2 Residual stress measurements

A compressive residual stress of approximately 150-250 MPa on the surface of the fatigue test specimens was measured. The residual stresses decreased to 40-60 MPa after electropolishing the surface layer of approximately 50 μm and the residual stress distribution remained on the same level after electropolishing at least 250 μm from the surface. It was, thus, assumed, that in the surface of the fatigue specimens there exists an average compressive residual stress of 200 MPa, and the residual stresses decrease linearly from the surface to the interior of 50 μm in depth. A compressive residual stress of 50 MPa was assumed to exist deeper under the surface in the control volume of the fatigue test specimens.

It was anticipated that the fatigue cracks most likely initiate from a site on the fatigue test specimen surface, where the compressive residual stresses have the lowest value. However, the compressive residual stresses on the fatigue specimen surface are randomly distributed, and the largest inclusions in the control volume for the prospective fatigue failure are also randomly distributed, i.e., the fatigue cracks do not necessarily initiate from the site where the residual stresses have the lowest value or from the site where the largest inclusion is located. Thus, in the “worst case” the largest inclusion in the control volume is located just under the

fatigue specimen surface in the site where the compressive residual stresses have the lowest value.

5.3 Surface roughness measurements

According to the \sqrt{area} parameter model for surface roughness values, see section 4.3, the surface roughness of the fatigue test specimens corresponds to a surface defect of the size $\sqrt{area_R} \approx 13...17 \mu\text{m}$, depending on the value of the pitch $2b$ used. This sounds reasonable, because the smallest fatigue crack initiating surface inclusions discovered in the SEM investigations were of the size $\sqrt{area} < 20 \mu\text{m}$, thus, being quite near the calculated $\sqrt{area_R}$. It is possible that the measured values of R_{max} may be smaller than the real maximum depth in the surface roughness of the fatigue specimen, i.e., the calculated value for $\sqrt{area_R} \approx 13...17 \mu\text{m}$ may be too small. For example, the surface scratch which caused fatigue crack initiation presented in Figure 32 seems to have a depth a of approximately $10 \mu\text{m}$. Thus, with the average value of the pitch, $2b = 80 \mu\text{m}$, we get $\sqrt{area_R} \approx 24 \mu\text{m}$ from equation 32 for the surface scratch presented in Figure 32.

5.4 Inclusion analyses

In the inclusion analyses according to DIN 50 602 and SFS-ENV 10247 a total inspection area of 300 mm^2 ($20 \times 15 \text{ mm}$) was examined. Only in three casts globular inclusions larger than $44 \mu\text{m}$ in diameter were found. The fracture surfaces of the fatigue specimens revealed much larger inclusions in almost every cast. The multiple linear regression analysis method gave no good correlation with $\sqrt{area_{\text{init.max}}}$ or $\sqrt{area_{\text{init.mean}}}$ when the results of DIN 50 602 and SFS-ENV 10247 inclusion analysis methods were used as the independent variables. The fitting results were improved when certain alloying elements were added to the regression equations, but the fitting results were still poor. It can be concluded that neither the results of DIN 50 602 nor SFS-ENV 10247 inclusion analysis methods are useful in estimating the size of the largest inclusion expected to exist in a larger volume, i.e., the inspection area of 300 mm^2 is too small to provide realistic information about the inclusion distribution and, most importantly, about the largest inclusions, in the studied steels.

The multiple linear regression analysis method gave a moderate correlation with σ_w/R_m ratio when DIN 50 602 inclusion rating method results were combined with the contents of oxygen, sulfur, chromium, silicon and nickel of the casts, see Table 12.

Table 12. Coefficients of the multiple linear regression analysis for σ_w/R_m ratio (see Figure 41).

		Independent variable	Correlation coefficient	p
R ²	0,63329	a	1,47603	0,00049
F-test	p = 0,02309	S	-3,70824	0,03208
		CR	-0,31101	0,24484
		SI	0,54902	0,00824
		NI	-1,83727	0,00279
		O	-8,59765	0,01117
		K _{O3}	0,00074	0,02238
		K _{O4}	-0,00062	0,08097

The value of R² was 0,63 and according to the F-test the result was statistically nearly significant, i.e., $p < 0,05$. Sulfur and oxygen had negative and statistically nearly significant effects on the σ_w/R_m ratio. On the other hand, the value of K_{O3} seemed to have a small positive correlation with the σ_w/R_m ratio and the value of K_{O4} seemed to have a small negative correlation. A moderate correlation was achieved with v_{15} when DIN 50 602 inclusion rating method results were combined with the contents of oxygen and calcium of the casts. The value of R² was 0,67 and according to the F-test the result was statistically very significant, i.e., $p < 0,001$. A moderate correlation was achieved with v_{15} also when SFS-ENV 10247 inclusion rating method results were combined with the contents of oxygen, calcium and undissolved aluminium of the casts. The value of R² was 0,65 and according to the F-test the result was statistically significant, i.e., $p < 0,01$. It can, thus, be stated that DIN 50 602 and SFS-ENV 10247 inclusion rating method results basically give information about the overall number of inclusions or the overall “cleanliness” of the steel, rather than about the largest and possible fatigue crack initiating inclusions in the steel, but they may have some use in estimating the fatigue properties and machinability of these steels, when combined with the contents of certain alloying elements.

It must be remembered, that the equations obtained by the multiple linear regression analyses were derived from a very narrow range of chemical compositions, i.e., the variance between the casts was small. The equations may, thus, not be used to estimate the properties of materials with different alloying contents. It is also most probable, that the effects of the independent variables on the dependent variables used in these analyses are not linear in the range of the independent variables. The independent variables may also have synergistic effects, which can not be accurately estimated by linear equations. It may also be questionable to combine the contents of alloying elements with the inclusion analysis results on regression analyses, because the former naturally have an effect on the latter, i.e., the inclusion analysis results are not totally independent variables.

5.5 Ultrasonic testing in immersion

The inspection volumes in ultrasonic tests in immersion were between 781410...833490 mm³. In most casts only defects/inclusions in the size category

C1 (40-100 μm) were found. Only in four casts defects/inclusions in the size categories C2 (>100 μm) and C3 (>200 μm) were found. A couple of elongated defects/inclusions (>3 mm in length) were detected in three casts, but they are not the inclusions which are responsible for fatigue crack initiation in these steels under the loading conditions in rotating bending fatigue. Thus, these inclusions were not taken into account in this study.

The results of the ultrasonic testing in immersion alone are not reliable considering the fact that in most casts inclusions over 100 μm in $\sqrt{\text{area}}$ were detected at the fatigue crack initiation sites of fatigue specimens, even though the control volume for prospective fatigue failure in a fatigue test set of 30 specimens was only 18654,1 mm^3 , thus, being around 40 times smaller than the inspection volume of the sample in the ultrasonic testing in immersion. Possible reasons for this are that the ultrasonic testing in immersion does not detect all the large globular inclusions in these steels or that the inclusion distribution in the ultrasonic testing samples is different from that of the fatigue test specimens. Both reasons sound possible. The latter reason sounds probable considering the fact that the fatigue test specimens and ultrasonic testing samples were cut from different parts of the 90 mm diameter bars, see Figures 20 and 23. However, in the steelmaking, according to Kiessling (1980), the lower central part of the steel ingot is usually richer in inclusions than other parts, and this uneven distribution pattern is retained throughout the subsequent steps in the steelmaking from ingot to finished product. Thus, this explanation is controversial, considering the fact that the fatigue test specimens were cut near the surface of the 90 mm diameter bars while the central parts of the bars were scanned in the ultrasonic testing in immersion.

The multiple linear regression analyses confirmed the observed comparison between the ultrasonic tests in immersion and the fatigue crack initiating inclusions, i.e., the results of the ultrasonic testing in immersion did not give any good correlation in the multiple linear regression analyses with either $\sqrt{\text{area}_{\text{mit.max}}}$, $\sqrt{\text{area}_{\text{mit.mean}}}$, or σ_w/R_m ratio. The multiple linear regression analysis method gave a moderate correlation with σ_w/R_m ratio when the modified results of the ultrasonic tests (inclusions larger than 200 μm were not taken into account) were combined with the contents of oxygen, sulfur, calcium, chromium and nickel of the casts, see Table 13.

Table 13. Coefficients of the multiple linear regression analysis for σ_w/R_m ratio (see Figure 39).

	Independent variable	Correlation coefficient	p
R^2		0,77300	
F-test		p = 0,00398	
	a	2,28480	0,00010
	S	-5,05877	0,00725
	CR	-1,60758	0,00131
	NI	-1,67997	0,00248
	CA	9,75454	0,02554
	O	-7,19202	0,01869
	ultra (40-100 μm)	0,00018	0,22141
	ultra (100-200 μm)	-0,01483	0,00078

The value of R^2 was 0,77 and according to the F-test the result was statistically significant ($p < 0,01$). According to the t-test, the negative effects of sulfur, chromium and nickel were statistically significant ($p < 0,01$) and the negative effect of oxygen was statistically nearly significant ($p < 0,05$). Inclusions in the size category 100-200 μm had a statistically very significant ($p < 0,001$) negative effect on the σ_w/R_m ratio. The effect of the inclusions in the size category 40-100 μm seemed to have a small positive effect, but it was not statistically significant ($p > 0,05$). This may be in accordance with the result that the average size of fatigue crack initiation inclusions had an effect on the σ_w/R_m ratio only on inclusion sizes larger than $\sim 70\text{-}90 \mu\text{m}$, see Figure 45. A moderate correlation was achieved with v_{15} when the modified results of the ultrasonic tests in immersion were used as the independent variables. The value of R^2 was 0,56 and according to the F-test the result was statistically very significant ($p < 0,001$). The result was improved when the contents of oxygen and calcium of the casts were added to the regression analysis. The value of R^2 was 0,89 and according to the F-test the result was statistically very significant, i.e., $p < 0,001$. Inclusions in the size category 100-200 μm had a statistically significant ($p < 0,001$) negative effect on the machinability, whereas inclusions in the size category 40-100 μm had a statistically very significant ($p < 0,001$) positive effect. It can, thus, be stated, that the results of the ultrasonic testing in immersion combined with the contents of certain alloying elements may provide estimates of the fatigue properties and the machinability of these steels, and the effects of these independent variables on these properties are partly the opposite. Small calcium aluminate inclusions seem to have a positive effect on the machinability of these steels and they seem not to have a significant effect on the σ_w/R_m ratio of these steels. Large calcium aluminate inclusions seem to have a negative effect both on the σ_w/R_m ratio and the machinability of these steels.

The limitations of the multiple linear regression analyses mentioned in Section 5.4 must be remembered also with the results of the ultrasonic tests in immersion.

5.6 SEM and EDS investigations

In the casts with the large amount of calcium injection, the fatigue cracks initiated mostly from the surface and interior inclusions. In the casts with the small amount of calcium injection the fatigue cracks initiated mostly from the surface discontinuities.

The chemical composition of the inclusions was similar to the typical inclusions in steels which have been calcium treated for improved machinability, i.e., calcium aluminates encapsulated in calcium sulfides. Also small amounts of magnesia and silica were detected in most of the inclusions. In a few cases fatigue crack initiating inclusions contained also carbon together with silicon. Also Gustafsson & Mellberg (1981) detected magnesia and silica in the calcium aluminates observed in the microsection analyses of calcium treated steels. In their

observations the calcium aluminates which contained magnesia and silica were larger in size than calcium aluminates which did not contain magnesia and silica. In this study such consistency was not observed. Magnesia and silica were detected also in the inclusions at microsections and in the smallest fatigue crack initiating inclusions, and larger inclusions without magnesia and silica were found at the fatigue crack initiation sites. In three cases, a pure aluminium oxide in the fatigue test specimen surface or near the surface had initiated the fatigue crack. These aluminium oxides were much smaller in size, $\sqrt{area} \approx 14..23 \mu\text{m}$, than the calcium aluminates encapsulated in calcium sulfides, the size of which varied from $\sim 20 \mu\text{m}$ to almost $300 \mu\text{m}$.

Fatigue crack initiation took place in two different ways: initiating from the interface between the inclusion and the matrix and initiating through cracking of the inclusion. The (Ca, Al, Mg, Si)O-CaS-inclusions could be divided into two groups: those of a globular shape and those of an irregular shape. Noticeably most of the (Ca, Al, Mg, Si)O-CaS-inclusions (93 %) were of the globular type. In the case of inclusions of globular shapes, the percentage contribution of cracked and non-cracked initiation types was 50 % and 50 %. The average sizes (\sqrt{area}) of cracked and non-cracked globular inclusions were $78,3 \mu\text{m}$ and $73,5 \mu\text{m}$, respectively. In the case of inclusions of irregular shapes, initiation took place through cracking of the inclusion in every case. The average size (\sqrt{area}) of irregular inclusions was $61,1 \mu\text{m}$. It is noteworthy that the largest inclusions found at the fatigue fracture initiation sites were of the globular type, i.e., of the same morphology with the inclusions detected at polished microsections, and they had similar chemical composition, even though the inclusions at the fatigue fracture initiation sites were much larger than the inclusions at the microsections. Figures 46-49 present the relationship between the fatigue life and the stress intensity factor range, ΔK , and the maximum value of the stress intensity factor, $K_{I\text{max}}$, which were calculated by equations 5 and 6, i.e., assuming the fatigue crack initiating inclusions as cracks and using the stress at fatigue crack initiation sites.

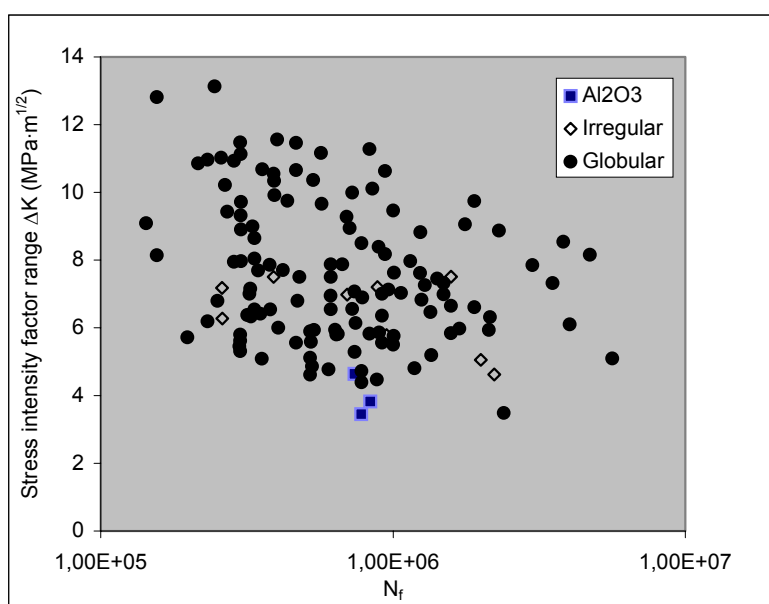


Figure 46. Relationship between the fatigue life and the stress intensity factor range, ΔK , for fatigue crack initiating inclusions of different types.

Estimating from the data in Figure 46, the fatigue failure takes place at the calcium aluminates with irregular shapes generally at lower ΔK levels than in the case of globular calcium aluminates. However, at the same ΔK level, there is no difference between the fatigue lives of calcium aluminates with irregular shapes and globular calcium aluminates. Although the average sizes of the two calcium aluminate types are almost equal, there is a significant difference between the size distributions of calcium aluminates with irregular shapes and calcium aluminates with globular shapes, i.e., the largest calcium aluminates are of the globular type, which results in smaller ΔK values for the calcium aluminates with irregular shapes. The alumina inclusions are much smaller than calcium aluminates, which results in smaller ΔK values.

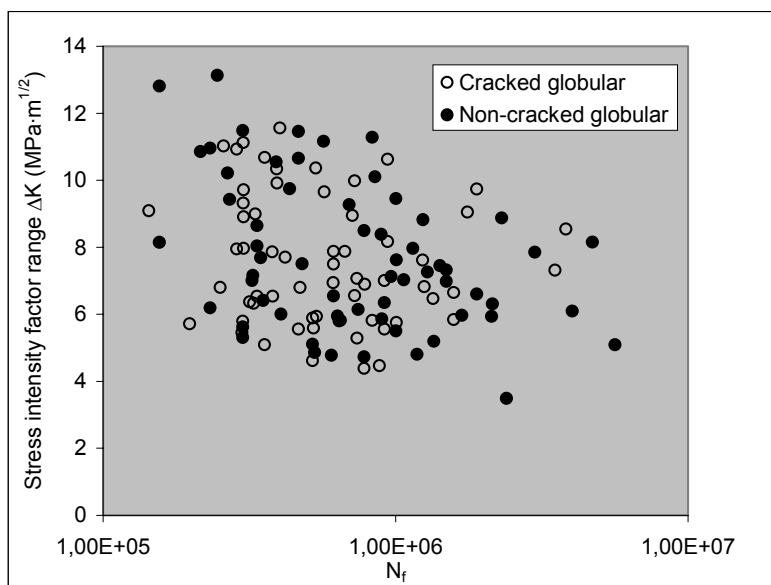


Figure 47. Relationship between the fatigue life and the stress intensity factor range, ΔK , for globular fatigue crack initiating inclusions of cracked and non-cracked types.

Figure 47 shows that at the same ΔK level the fatigue crack initiation mode, i.e., initiation either from the interface between the inclusion and the matrix or through cracking of the inclusion, makes no difference in the fatigue life. Considering the fact that the average size of both types of globular fatigue crack initiating inclusions are almost identical, this suggests that the driving forces of short cracks in both cases are the same. This is controversial with the observations of Melander and Ölund (1999), where the fatigue life of a steel which showed cracked alumina inclusions on the fracture surfaces was significantly shorter than that of a steel which showed non-cracked alumina inclusions on the fracture surfaces. This may suggest that the debonding between duplex inclusions, such as calcium aluminates surrounded by a sulfide shell, and the matrix takes place more easily than between alumina inclusions and the matrix. Possible reasons for this may be different coefficient of friction on the interface between inclusion and matrix and the differences between the stress fields around duplex inclusions and alumina inclusions.

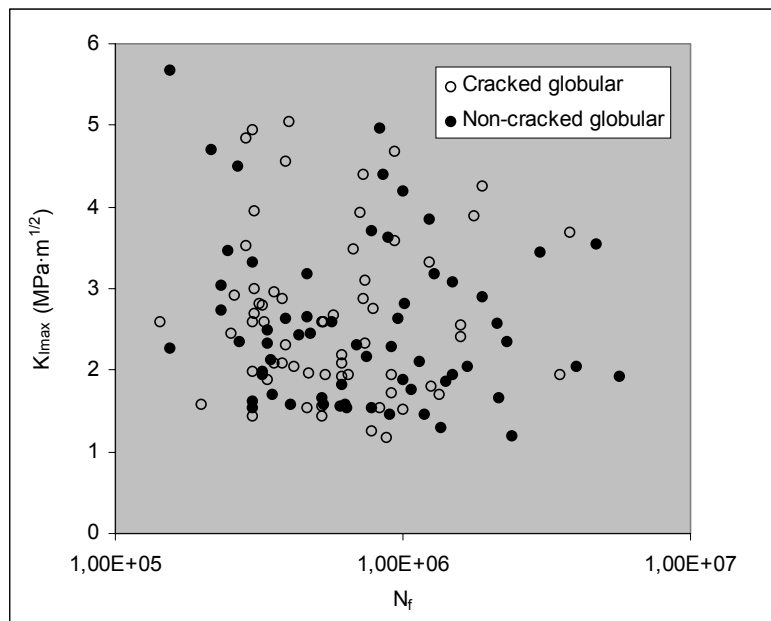


Figure 48. Relationship between the fatigue life and the maximum value of the stress intensity factor, $K_{I\max}$, for globular fatigue crack initiating inclusions of cracked and non-cracked types.

In Figure 48 a modification of Figure 47 is presented by substituting ΔK by the maximum value of the stress intensity factor, $K_{I\max}$, at the fatigue crack initiating inclusion, i.e., only the tensile portion of the cyclic stress and the residual stresses are taken into account. When compared with Figure 47, no difference is observed, i.e., the fatigue crack initiation mode seems to make no difference on the fatigue life.

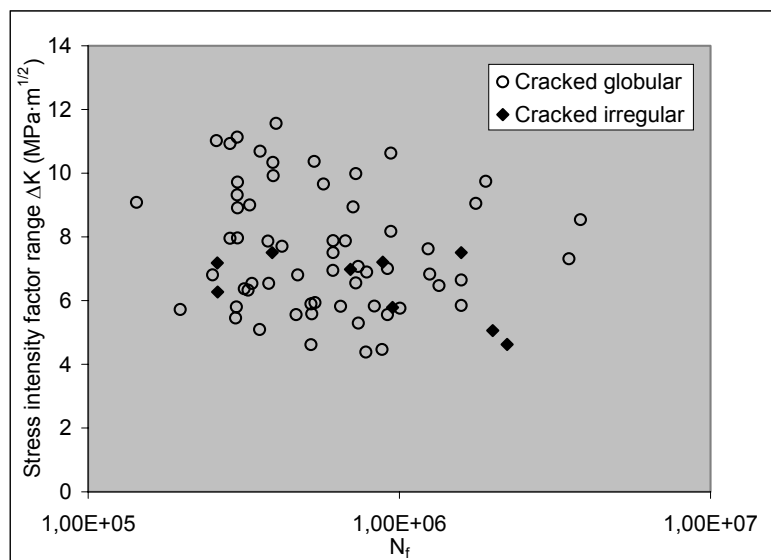


Figure 49. Relationship between the fatigue life and the stress intensity factor range, ΔK , for cracked fatigue crack initiating inclusions of different shapes.

Estimating from the data in Figure 49, the fatigue failure takes place at the cracked calcium aluminates with irregular shapes at lower ΔK levels than in the case of cracked calcium aluminates with globular shapes. Smaller ΔK values for the calcium aluminates with irregular shapes result from the differences between the inclusion size distributions of the two cases. From the stress concentration point of view verified by numerous researchers (e.g., Duckworth & Ineson, 1963; Murakami, 2002), inclusions with irregular shapes produce a higher stress concentration around the inclusion and hence a larger driving force for the crack initiation, resulting in easier fatigue crack initiation and shorter fatigue lives at higher stress levels, and, thus, at higher ΔK levels, but at lower stress levels the shape of inclusion has no significance. Estimating from the data in Figure 49, at the same ΔK levels, there is no difference between the fatigue lives of fatigue failures initiating from cracked calcium aluminates with irregular shapes or cracked calcium aluminates with globular shapes.

5.7 Statistics of extreme value evaluation and application of the Murakami-Endo model

It can be seen that in some casts there are a few inclusions which are located far from the trendlines, i.e., these data points do not follow the statistical distribution of the extreme values. This may be caused by the fact that there were too few inspections or the standard inspection area was not sufficiently large. However, the standard inspection area used in this study, 113 mm², was relatively large when compared with the standard inspection areas of the earlier studies. For example, in Murakami & Usuki (1989), Murakami et al. (1998) and Beretta & Murakami (2001) standard inspection areas of 0,482 mm², 0,384 mm² and 66,37 mm² were used.

In Beretta & Murakami (2001) two different distributions of inclusions having different chemical composition, i.e., inclusions containing sulfur, silicon and potassium and inclusions containing calcium and aluminium, were detected when two different standard inspection areas (0,384 mm² and 66,37 mm², respectively) were used. In Zhou et al. (2002) it was discovered that inclusions, which have the same chemical composition can have a different 3D structure. In such a case these inclusions should be treated as two different inclusion types, because they have a different statistics of extreme value distribution. The statistics of extreme value distribution for these multiple types of inclusions can be described by a bilinear graph on the probability plot. When the size of the inclusions at the fatigue crack initiation sites is predicted by a 2D standard inspection area method the standard inspection area S_0 should be larger than a certain critical value S_{crit} . Otherwise the type of inclusions that are responsible for the fatigue failure may not be detected.

The predicted $\sqrt{area_{max}}$ values were in most casts much smaller than the size of the inclusions found at the fatigue crack initiation sites of the fatigue specimens. Figure 37 and Appendix 3 show clearly the bilinear probability plot pattern of the

casts, which explains the reason why the sizes of the predicted extreme inclusions in almost every cast are much smaller than the inclusions at the fatigue crack initiation sites. When compared with the investigations of Beretta & Murakami (2001) and Zhou et al. (2002), it is interesting that the bilinear inclusion distribution detected in this study consists of inclusions having the same morphology and similar chemical composition but different maximum size. According to Murakami (2002), the size (\sqrt{area}), e.g., of inclusions containing calcium originating from refractories does not obey the statistics of extreme values. The critical standard inspection area, S_{crit} , for these steels was approximately 8400 mm² at least. In most of the casts, the distributions of inclusions at microsections and inclusions at the fatigue crack initiation sites overlapped partly each other, i.e., the smallest inclusions at the fatigue crack initiation sites could be fit also with the distribution of inclusions at microsections. In such cases the S_{crit} values calculated from the intersection points of the two distributions may be considered overly conservative, and the required size of the standard inspection area lies somewhere between $S_0 = 113$ mm² and the S_{crit} calculated from the intersection point. In a few cases, e.g., in Cast A5 and A8, the predicted $\sqrt{area_{max}}$ values were very near or even larger than the sizes of the inclusions found at the fatigue crack initiation sites of the fatigue specimens.

In Figure 38 and Appendix 4 it can be seen that the experimental fatigue test results lie between the predicted upper and lower bounds of the fatigue strength, i.e., the Murakami-Endo model gives a conservative estimate for the lower bound of the fatigue limit of these steels with the stress ratio $R = -3$. With the stress ratio $R = -1$ the Murakami-Endo model gives an overly conservative estimate for the lower bound of the fatigue limit. The reason for this is the compressive residual stresses in the fatigue test specimen surfaces, and these residual stresses are therefore taken into account by using the stress ratio $R = -3$.

6 CONCLUSIONS

The main objective of this study was to examine the fatigue properties of a calcium treated carburizing steel with two different calcium treatment levels with industrial test charges in a full scale and to examine the applicability of different inclusion rating methods in estimating the fatigue properties and machinability of these steels.

The following conclusions can be drawn from the studies:

- There were no significant differences between the values of σ_w/R_m ratio of the casts with the large amount of calcium injection and the casts with the small amount of calcium injection. The fatigue strength scatter was larger in the casts with the large amount of calcium injection. The average fatigue crack initiating inclusion size had an effect on the σ_w/R_m ratio only on average fatigue crack initiating inclusion sizes larger than ~ 70 -90 μm .

- In the casts with the large amount of calcium injection, the fatigue cracks initiated mostly from the surface and interior inclusions. In the casts with the small amount of calcium injection, the fatigue cracks initiated mostly from the surface discontinuities. In both types of casts the inclusions responsible for fatigue crack initiation were in most cases calcium aluminates encapsulated in calcium sulfide containing small amounts of magnesia and/or silica. There was no difference between the fatigue lives of fatigue failures originated from cracked and non-cracked inclusions of the same size. Fatigue crack initiation took place at the cracked calcium aluminates with irregular shapes at lower ΔK levels than in the case of cracked calcium aluminates with globular shapes. However, at the same ΔK levels, no difference between the fatigue lives of the two cases was observed.
- Neither the results of the traditional inclusion rating methods nor the results of the ultrasonic testing in immersion correlated with the sizes of the inclusions that were responsible for fatigue failure in these steels. The results of the inclusion analysis methods combined with certain alloying elements, especially calcium, oxygen, sulfur and insoluble aluminium, however, showed statistically significant correlation with v_{15} and the σ_w/R_m ratio despite the small variance between the data samples, i.e., the casts. The information provided by the results of the ultrasonic tests in immersion is more relevant than that of the conventional inclusion rating methods when the effect of inclusions on the fatigue properties and machinability of these steels is considered, but its resolution capability still needs improvement.
- In most casts the predicted $\sqrt{area_{max}}$ values by the statistics of extreme value evaluation method were much smaller than the size of the inclusions found at the fatigue crack initiation sites of the fatigue specimens, i.e., the standard inspection area was too small to catch the population of inclusions which initiated the fatigue cracks.
- The studied steels seemed to have two different inclusion size distributions, i.e., the inclusions detected at the polished microsections and the inclusions at the fatigue crack initiation sites, and these inclusion distributions overlapped partly each other when they were examined in the statistics of extreme value distribution chart.
- The bilinear inclusion distribution detected in this study consisted of inclusions having the same morphology and similar chemical composition but different maximum size, which was contrary to the earlier findings of the bilinear nature of inclusion distribution in some steels, where either the morphology or the chemical composition of the inclusions was different from each other.
- For successful application of the Murakami-Endo model, the inspection area or volume has to be above a certain critical value, which for these steels was 8400 mm² at least, to make it possible to detect the population of the largest inclusions, which are responsible for fatigue failure. The Murakami-Endo model gives a conservative estimate for the lower bound of the fatigue limit for these steels.

REFERENCES

- Anderson, C.W., Shi, G., Atkinson, H.V. & Sellars, C.M. 2000. The precision of methods using the statistics of extremes for the estimation of the maximum size of inclusions in clean steels. *Acta Materialia*, 48 (17), pp. 4235-4246.
- Atkinson, H.V., Shi, G., Sellars, C.M. & Anderson, C.W. 2000. Statistical prediction of inclusion sizes in clean steels. *Materials Science and Technology*, 16 (10), pp. 1175-1180.
- Beretta, S., Blarasin, A., Endo, M., Giunti, T. & Murakami, Y. 1997. Defect tolerant design of automotive components. *International Journal of Fatigue*, 19 (4), pp. 319-333.
- Beretta, S. & Murakami, Y. 1998. Statistical analysis of defects for fatigue strength prediction and quality control of materials. *Fatigue & Fracture of Engineering Materials & Structures*, 21 (9), pp. 1049-1065.
- Beretta, S. & Murakami, Y. 2001. Largest-extreme-value distribution analysis of multiple inclusion types in determining steel cleanliness. *Metallurgical and Materials Transactions B*, 32B (3), pp. 517-523.
- Brooksbank, D. & Andrews, K.W. 1968. Thermal expansion of some inclusions found in steels and relation to tessellated stresses. *Journal of the Iron and Steel Institute*, 206 (6), pp. 595-599.
- Brooksbank, D. & Andrews, K.W. 1969. Tessellated stresses associated with some inclusions in steel. *Journal of the Iron and Steel Institute*, 207 (4), pp. 474-483.
- Brooksbank, D. 1970. Thermal expansion of calcium aluminate inclusions and relation to tessellated stresses. *Journal of the Iron and Steel Institute*, 208 (5), pp. 495-499.
- Brooksbank, D. & Andrews, K.W. 1972. Stress fields around inclusions and their relation to mechanical properties. *Journal of the Iron and Steel Institute*, 210 (4), pp. 246-255.
- Carlsson, G. & Helle, L.W. 1985. Multicomponent injection - development of the technology and results of trials at MEFOS. *Scandinavian Journal of Metallurgy*, 14 (1), pp. 18-24.
- Chalant, G. & Suyitno, B.M. 1991. Effects of microstructure on low and high cycle fatigue behaviour of a micro-alloyed steel. In: *Proc. 6th Int. Conf. Mechanical Behav. Materials*, vol. 2, Kyoto, Japan, 29 July – 2 Aug., pp. 511-516.
- Cheng, J., Eriksson, R. & Jönsson, P. 2003. Determination of macroinclusions during clean steel production. *Ironmaking & Steelmaking*, 30 (1), pp. 66-72.

Cogne, J.Y., Heritier, B. & Monnot, J. 1987. Cleanness and fatigue life of bearing steels. In: Clean Steel 3, Balatonfured, Hungary, 2-4 June 1986, The Institute of Metals, pp. 26-31.

Collins, J.A. 1981. Failure of materials in mechanical design: analysis, prediction, prevention. John Wiley & Sons, Inc., New York. 629 p. ISBN 0-471-05024-5.

Collins, S.R. & Michal, G.M. 1994. Effects of steelmaking on the transverse fatigue properties of AISI 4140 steel. 36th Mechanical Working and Steel Processing Conference, Baltimore, Maryland, USA, 16-19 Oct. 1994, ASTM, pp. 231-239.

DIN 50 602. 1985. Mikroskopische Prüfung von Edelstählen auf nichtmetallische Einschlüsse mit Bildreihen.

Duckworth, W.E. & Ineson, E. 1963. The effects of externally introduced alumina particles on the fatigue life of En24 steel. Clean Steel, Iron Steel Inst. Sp. Rep., 77, pp. 87-103.

Elber, W. 1971. The significance of fatigue crack closure. In: Damage Tolerance in Aircraft Structures, Toronto, Ontario, Canada, 21-26 June 1970, ASTM, pp. 230-242.

Ellyin, F. 1997. Fatigue damage, crack growth and life prediction. Chapman & Hall, London. 469 p. ISBN 0-412-59600-8.

Frost, N.E. & Dugdale, D.S. 1957. Fatigue tests on notched mild steel plates with measurements of fatigue cracks. Journal of the Mechanics and Physics of Solids, 5, pp. 182-192.

Frost, N.E. 1960. Notch effects and the critical alternating stress required to propagate a crack in an aluminium alloy subject to fatigue loading. Journal of Mechanical Engineering Science, 2, pp. 109-119.

Frost, N.E. & Dixon, J.R. 1967. A theory of fatigue-crack growth. International Journal of Fracture Mechanics, 3 (4), pp. 301-316.

Frost, N.E., Marsh, K.J. & Pook, L.P. 1974. Metal fatigue. Oxford University Press, London. 499 p. ISBN 0-19-856114-8.

Garwood, M.F., Zurburg, H.H. & Erickson, M.A. 1951. Correlation of laboratory tests and service performance, interpretation of tests and correlation with service. ASM, pp. 1-77.

Gumbel, E.J. 1958. Statistics of extremes. Columbia University Press, New York. 375 p.

Gustafsson, S. & Mellberg, P.O. 1981. Inclusion picture and inclusion origin in a calcium treated steel. In: Swedish Symposium on Non-Metallic Inclusions in Steel, Södertälje, Sweden, 27-29 April, Uddeholms AB, pp. 35-68.

Helle, A., Väinölä, R. & Pietikäinen, J. 1993. The effect of non-metallic inclusions on the machinability of steel. Helsinki University of Technology, Report TKK-V-B85. 52 p. ISBN 951-22-1536-5.

Hertzberg, R.W. 1996. Deformation and fracture mechanics of materials. John Wiley & Sons, Inc., New York. 786 p. ISBN 0-471-01214-9.

Hetzner, D. W. & Pint, B. A. 1988. Sulfur content, inclusion chemistry, and inclusion size distribution in calcium treated 4140 steel. In: Inclusions and Their Influence on Material Behavior, Chicago, Illinois, USA, 24-30 Sept., ASM International, pp. 35-48.

ISO 4287. 1997. Geometrical Product Specifications (GPS) - Surface texture: Profile method - Terms, definitions and surface texture parameters.

Itoya, H., Tokaji, K., Nakajima, M. & Ko, H.-N. 2003. Effect of surface roughness on step-wise S-N characteristics in high strength steel. International Journal of Fatigue, 25 (5), pp. 379-385.

Kiessling, R. 1978. Non-metallic inclusions in steel, Parts I-IV. The Metals Society. 450 p. ISBN 0-904357-18-X.

Kiessling, R. 1980. Clean steel: a debatable concept. Metal Science, 14 (5), pp. 161-172.

Kiessling, R. 1989. Non-metallic inclusions in steel, Part V. The Institute of Metals. 194 p. ISBN 0-901462-40-3.

Kitagawa, H. & Takahashi, S. 1976. Applicability of fracture mechanics to very small cracks or the cracks in the early stage. In: Second International Conference on Mechanical Behavior of Materials, ASM, Metals Park, Ohio, pp. 627-631.

Kuguel, R. 1961. A relation between theoretical stress concentration factor and fatigue notch factor deduced from the concept of highly stressed volume. In: Proceedings of the American Society for Testing and Materials, vol 61, ASTM, pp. 732-748.

Lu, D-Z, Irons, G.A. & Lu, W-K. 1994. Kinetics and mechanisms of calcium dissolution and modification of oxide and sulphide inclusions in steel. Ironmaking & Steelmaking, 21 (5), pp. 362-371.

Lund, T. & Akesson, J. 1988. Oxygen content, oxidic microinclusions, and fatigue properties of rolling bearing steels. In: Effect of Steel Manufacturing Processes on the Quality of Bearing Steels, Phoenix, Arizona, USA, 4-6 Nov. 1986, ASTM, pp. 308-330.

Makkonen, M. 1999. Size effect and notch size effect in metal fatigue. Doctor of Technology thesis. Acta Universitatis Lappeenrantaensis, 83. 93 p. ISBN 951-764-349-7.

Melander, A. & Gustavsson, A. 1996. An FEM study of driving forces of short cracks at inclusions in hard steels. International Journal of Fatigue, 18 (6), pp. 389-399.

Melander, A. & Ölund, P. 1999. Detrimental effect of nitride and aluminium oxide inclusions on fatigue life in rotating bending of bearing steels. Materials Science and Technology, 15 (5), pp. 555-562.

Meredith, J.G. & Moore, W. 1981. Development and use of lime-base products for injection metallurgy. Scandinavian Journal of Metallurgy, 10 (2), pp. 73-79.

Miller, I., Freund, J. F. & Johnson, R. A. 1990. Probability and statistics for engineers. Prentice-Hall Inc., New Jersey. 612 p.

Monnot, J., Heritier, B. & Cogne, J.Y. 1988. Relationship of melting practice, inclusion type, and size with fatigue resistance of bearing steels. In: Effect of Steel Manufacturing Processes on the Quality of Bearing Steels, Phoenix, Arizona, USA, 4-6 Nov. 1986, ASTM, pp. 149-165.

Murakami, Y. & Endo, T. 1981. The effects of small defects on the fatigue strength of hard steels. In: Materials, Experimentation and Design in Fatigue, Warwick University, England, 24-27 March, IPC Science and Technology Press Ltd., Guildford, pp. 431-440.

Murakami, Y. & Endo, M. 1983. Quantitative evaluation of fatigue strength of metals containing various small defects or cracks. Engineering Fracture Mechanics, 17 (1), pp. 1-15.

Murakami, Y. & Endo, M. 1986. Effects of hardness and crack geometries on ΔK_{th} of small cracks emanating from small defects. In: The behaviour of short fatigue cracks. Mechanical Engineering Publications, London, pp. 275-293. ISBN 0-85298-615-7.

Murakami, Y. (ed.). 1987. Stress intensity factors handbook, Vol. 1-2. Pergamon Press, Oxford, 1456 p. ISBN 0-08-034809-2.

Murakami, Y., Kodama, S. & Konuma, S. 1989. Quantitative evaluation of effects of non-metallic inclusions on fatigue strength of high strength steels. I: Basic fatigue mechanism and evaluation of correlation between the fatigue stress and the size and location of non-metallic inclusions. *International Journal of Fatigue*, 11 (5), pp. 291-298.

Murakami, Y. & Usuki, H. 1989. Quantitative evaluation of effects of non-metallic inclusions on fatigue strength of high strength steels. II: Fatigue limit evaluation based on statistics for extreme values of inclusion size. *International Journal of Fatigue*, 11 (5), pp. 299-307.

Murakami, Y., Uemura, Y., Natsume, Y. & Miyakawa, S. 1990. Effect of mean stress on the fatigue strength of high-strength steels containing small defects or nonmetallic inclusions. *Transactions of the JSME (A)*, 56 (525), pp. 1074-1081.

Murakami, Y., Kawakami, K. & Duckworth, W. E. 1991. Quantitative evaluation of effects of shape and size of artificially introduced alumina particles on the fatigue strength of 1.5Ni-Cr-Mo (En24) steel. *International Journal of Fatigue*, 13 (6), pp. 489-499.

Murakami, Y. & Endo, M. 1994. Effects of defects, inclusions and inhomogeneities on fatigue strength. *International Journal of Fatigue*, 16 (3), pp. 163-182.

Murakami, Y., Toriyama, T. & Coudert, E. M. 1994. Instructions for a new method of inclusion rating and correlations with the fatigue limit. *Journal of Testing and Evaluation*, 22 (4), pp. 318-326.

Murakami, Y. 1996. Effects of small defects and inhomogeneities on fatigue strength: experiments, model and applications to industry. In: *ECF 11 - Mechanisms and Mechanics of Damage and Failure*, vol. I, Poitiers-Futuroscope, France, 3-6 Sept. pp. 31-42.

Murakami, Y., Takada, M. & Toriyama, T. 1998. Super-long life tension-compression fatigue properties of quenched and tempered 0.46% carbon steel. *International Journal of Fatigue*, 20 (9), pp. 661-667.

Murakami, Y. 2002. *Metal fatigue: effects of small defects and nonmetallic inclusions*. Elsevier Science Ltd., Oxford. 369 p. ISBN 0-08-044064-9.

Nishijima, S., Tanaka, K. & Sumiyoshi, H. 1984. The defect size determining the fatigue limits of steels. In: *Advances in Fracture Research (Fracture 84)*, vol. 3, New Delhi, India, 4-10 Dec. 1984, Pergamon Press Ltd., Oxford, pp. 1719-1726.

Nordberg, H. 1981. The effect of notches and non-metallic inclusions on the fatigue properties of high-strength steel. In: *Swedish Symposium on Non-metallic Inclusions in Steel*, Södertälje, Sweden, 27-29 April, Uddeholms AB, pp. 395-428.

Pearson, S. 1975. Initiation of fatigue cracks in commercial aluminum alloys and subsequent propagation of very short cracks. *Engineering Fracture Mechanics*, 7 (2), pp. 235-247.

Peterson, R.E. 1959. Notch-sensitivity. In: *Metal Fatigue*. McGraw-Hill, New York, pp. 293-306.

Peterson, R.E. 1974. *Stress concentration factors*. John Wiley & Sons, Inc., New York. 317 p. ISBN 0-471-68329-9.

Pickett, M.L., Naylor, D.J. & Cristinacce, M. 1985. Development and application of improved machinable engineering steels. In: *High Productivity Machining: Materials and Processes*, New Orleans, Louisiana, USA, 7-9 May, American Society for Metals, pp. 253-264.

Pilkey, W.D. 1997. *Peterson's stress concentration factors*. John Wiley & Sons, Inc., New York. 508 p. ISBN 0-471-53849-3.

Saleil, J., Leroy, F., Gaye, H. & Gatellier, C. 1989. Inclusion control in calcium treated steels. In: *Residual and Unspecified Elements in Steel*, Bal Harbour, Florida, USA, 11-13 Nov. 1987, ASTM, pp. 69-79.

Schijve, J. 1984. The practical and theoretical significance of small cracks. An evaluation. In: *Fatigue '84, Proceedings of the 2nd International Conference on Fatigue*, Birmingham, UK, 3-7 Sept. 1984, Warley, EMAS, 2, pp. 751-771.

SFS-ENV 10247. 1998. Micrographic examination of the nonmetallic inclusion content of steels using standard pictures. 104 p.

Shi, G., Atkinson, H.V., Sellars, C.M. & Anderson, C.W. 2000. Application of the generalized Pareto distribution to the estimation of the size of the maximum inclusion in clean steels. *Acta Materialia*, 47, pp. 1455-1468.

Shigley, J.E. & Mischke, C.R. 1986. *Standard Handbook of Machine Design*. McGraw-Hill, Inc., New York. 1632 p. ISBN 0-07-056892-8.

Stahl-Eisen-Prüfblatt 1570. 1971. Mikroskopische Prüfung von Edelstählen auf schmale langgestreckte nichtmetallische Einschlüsse.

Suresh, S. & Ritchie, R.O. 1984. Propagation of short fatigue cracks. *International Metal Reviews*, 29, pp. 445-476.

Suresh, S. 1992. *Fatigue of materials*. Cambridge Solid State Science Series. Cambridge University Press. 617 p. ISBN 0-521-437-63-6.

Taylor, D. & Knott, J.F. 1981. Fatigue crack propagation behavior of short cracks: the effect of microstructure. *Fatigue & Fracture of Engineering Materials & Structures*, 4 (2), pp. 147-155.

Taylor, D. 1986. Fatigue of short cracks: the limitations of fracture mechanics. In: *The behaviour of short fatigue cracks*. Mechanical Engineering Publications, London, pp. 479-490. ISBN 0-85298-615-7.

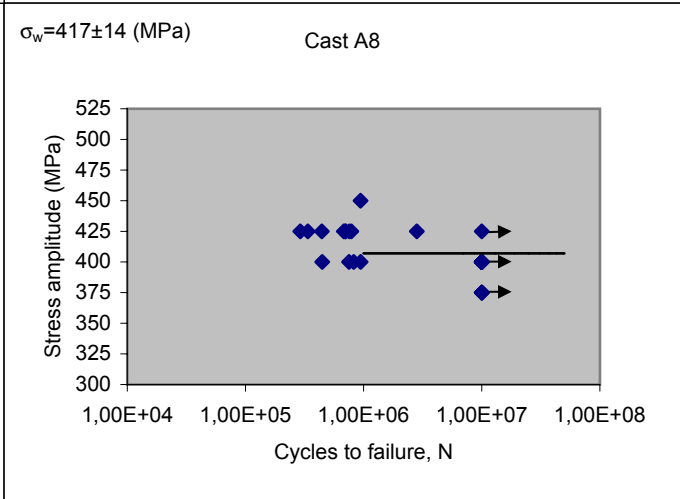
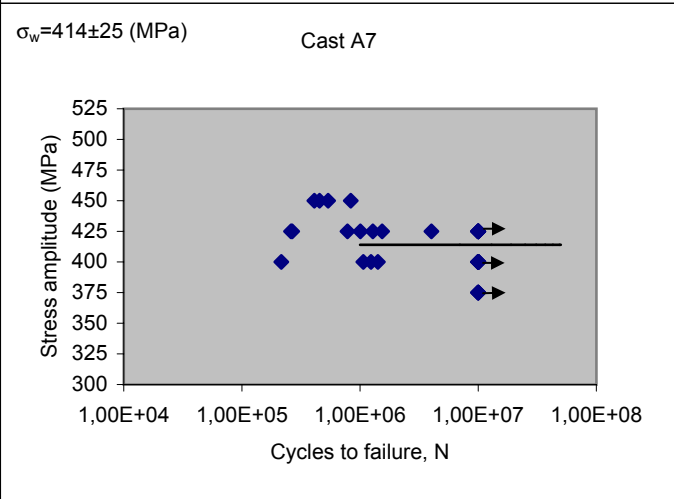
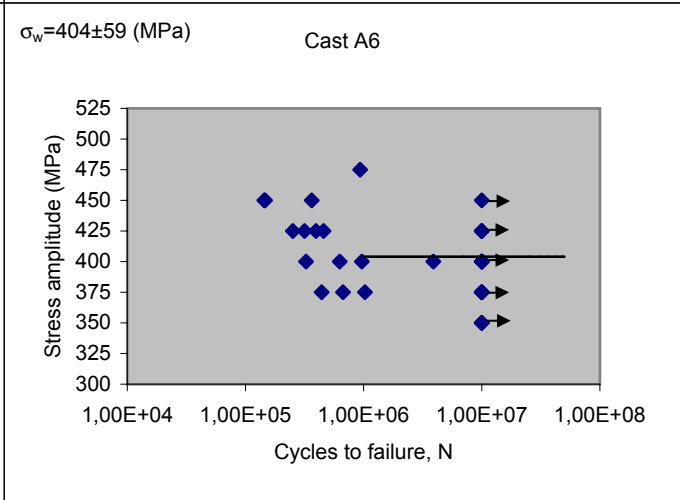
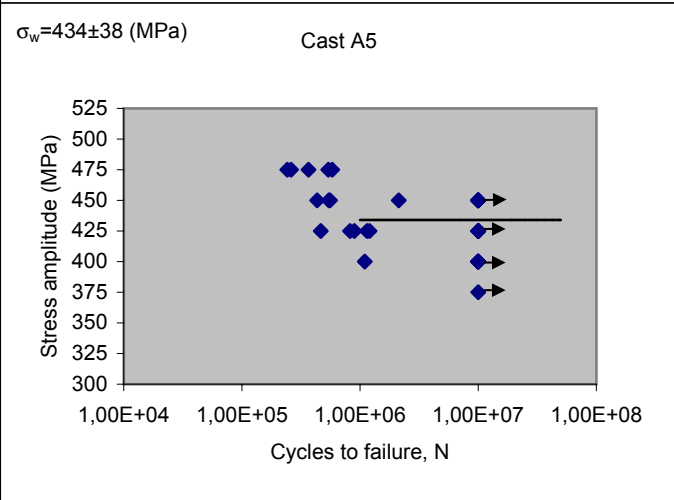
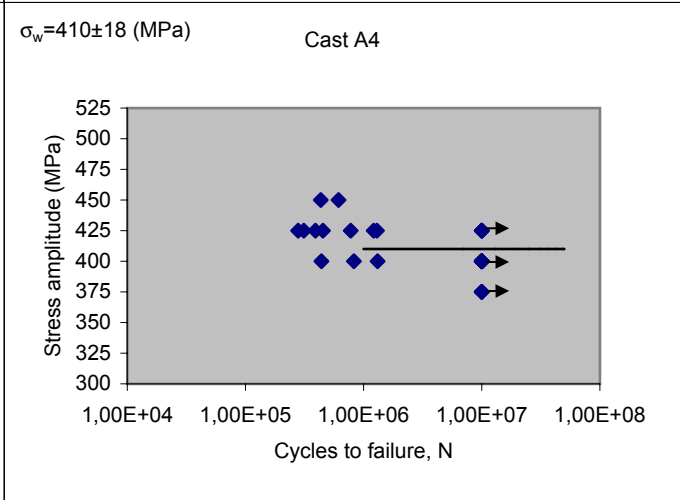
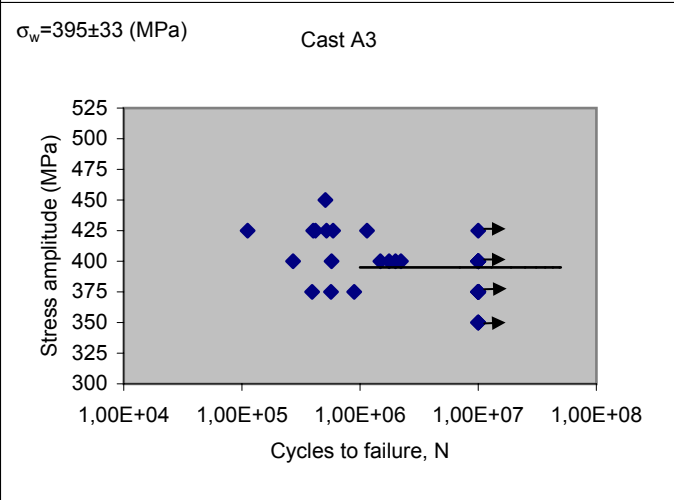
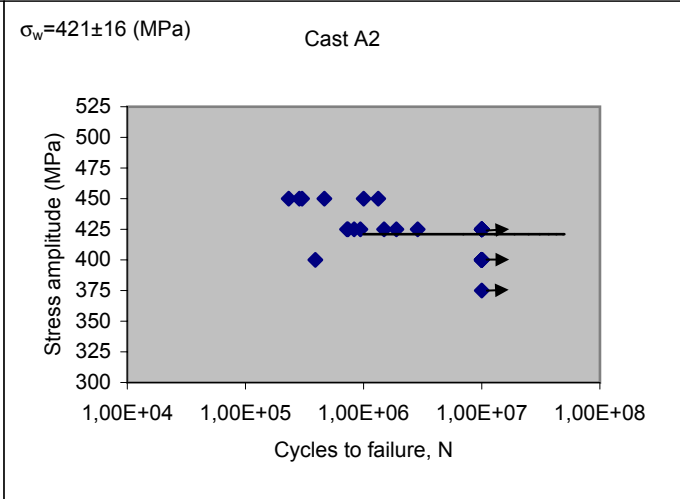
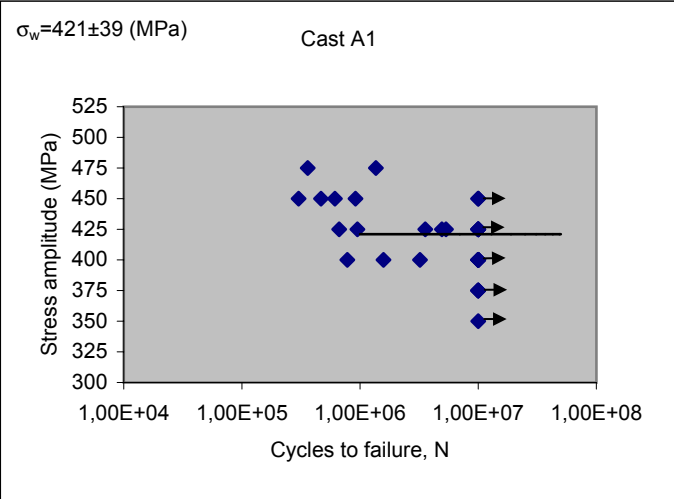
Wilson, A. D. 1982. Effect of calcium treatment on inclusions in constructional steels. *Metal Progress*, 121 (5), pp. 41-46.

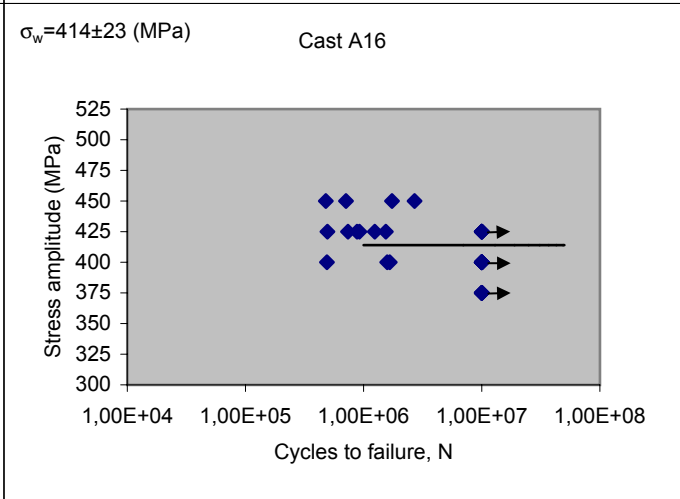
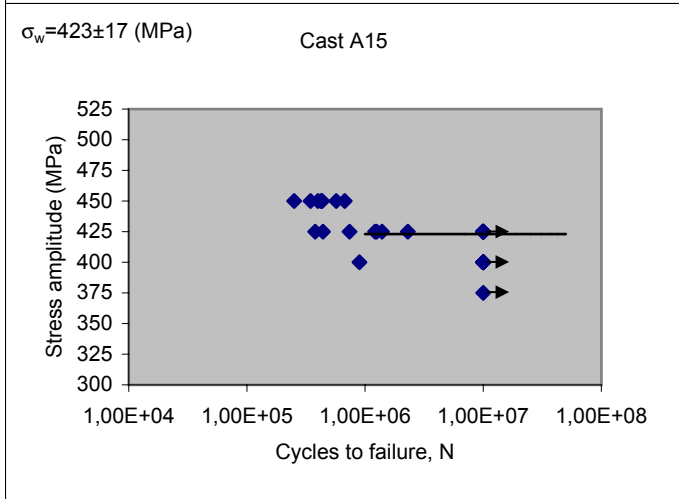
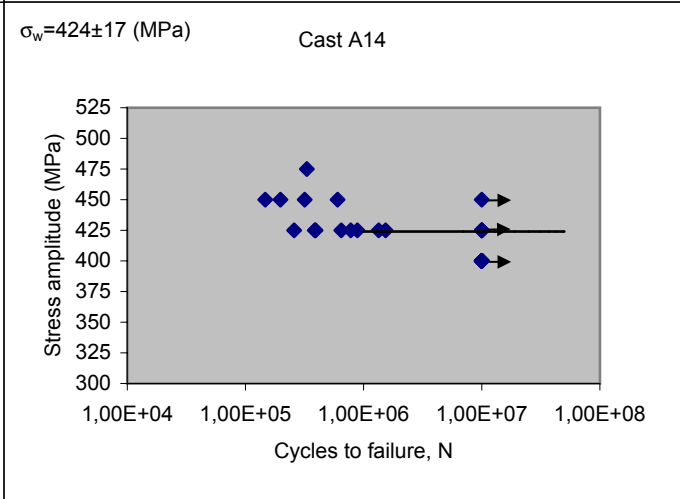
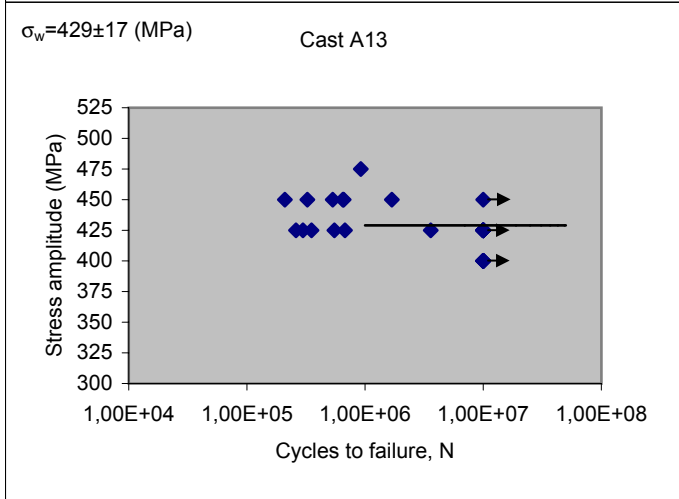
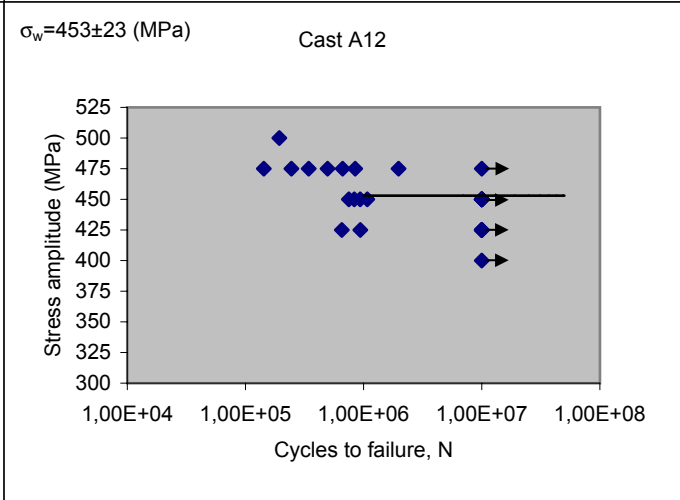
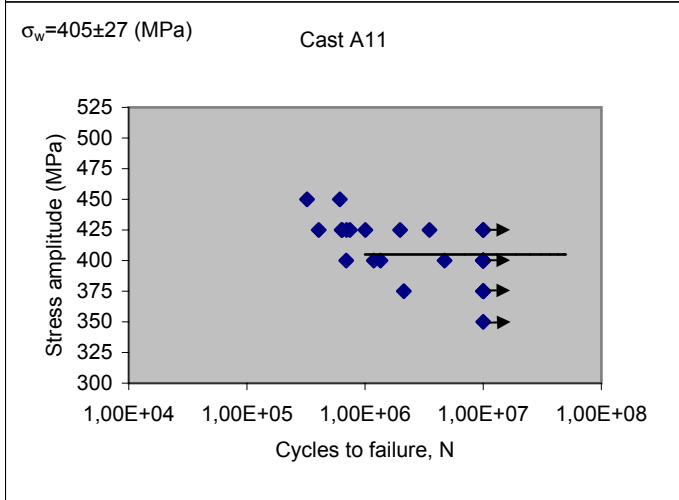
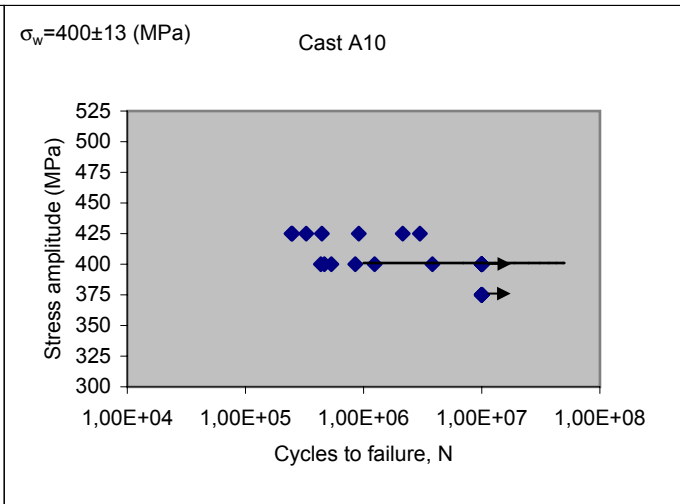
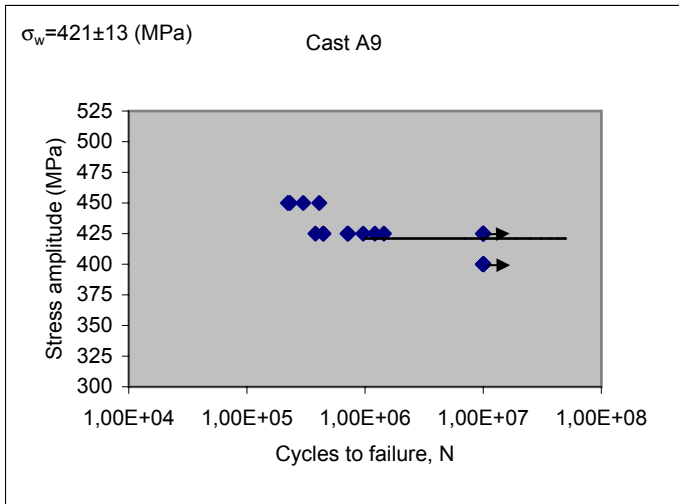
Zhou, S., Murakami, Y., Beretta, S. & Fukushima, Y. 2002. Experimental investigation on statistics of extremes for three-dimensional distribution of non-metallic inclusions. *Materials Science and Technology*, 18 (12), pp. 1535-1543.

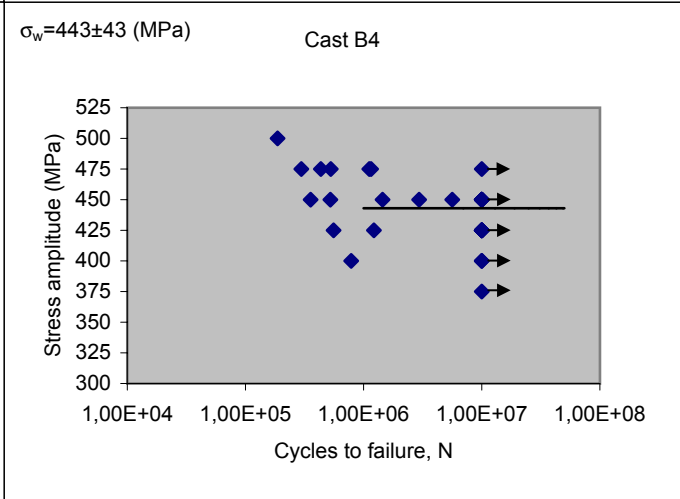
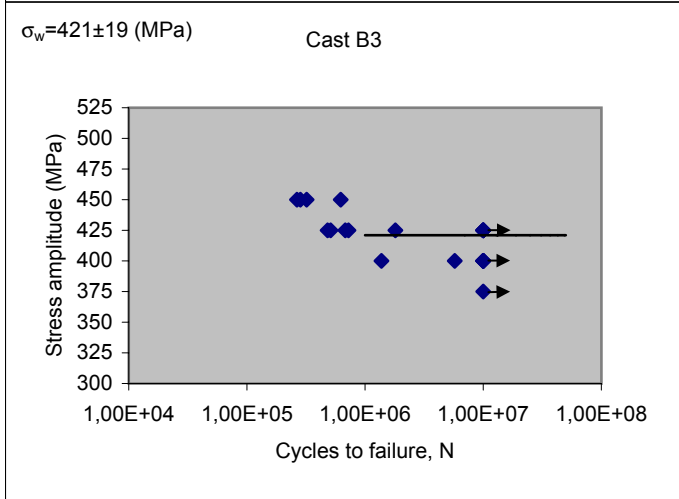
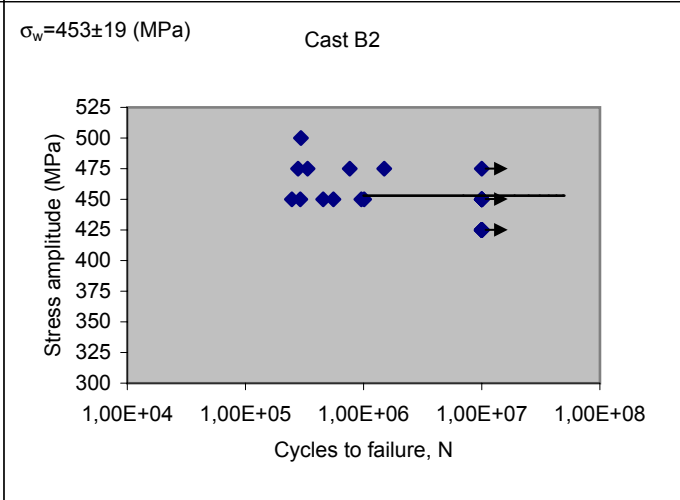
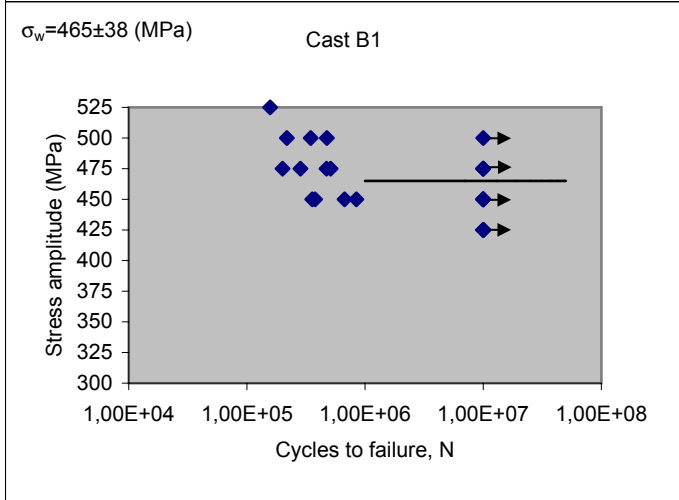
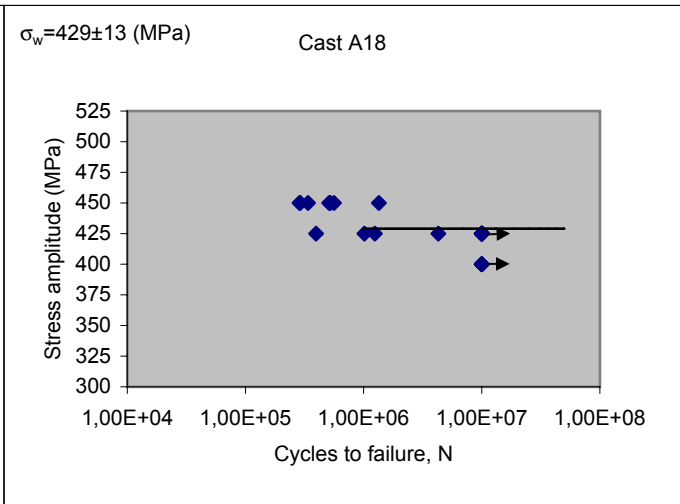
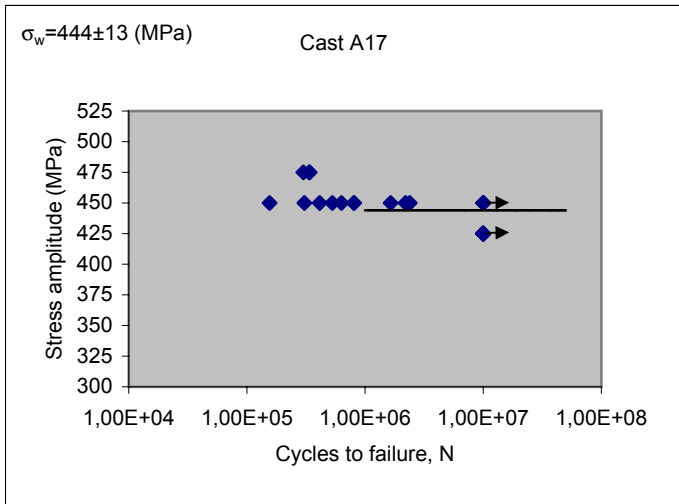
APPENDIX 1. Fatigue test graphs

Rotating bending fatigue, R = -1, f = 40 Hz

Parallel lines stand for fatigue limits with 50% failure probability, σ_w (MPa)







APPENDIX 2. FATIGUE CRACK INITIATING INCLUSION DATA

σ = Nominal stress at specimen surface

N_f = Cycles to failure

HV = Vickers microhardness (200 g) of the material near the fatigue crack initiation site

$\sqrt{\text{area}}$ = Square root of projection area of inclusion

h = Distance from surface (μm)

* = Inclusion is located just under specimen surface

R = Stress ratio at inclusion

σ' = Stress at inclusion

σ'_w = Fatigue limit at inclusion calculated by Equation 20

detached = inclusion detached from fracture surface and, thus, not present for chemical analysis

ΔK = Stress intensity factor range

A1

Specimen no	σ	N_f	HV	$\sqrt{\text{area}}$	h	Composition	R	σ'	σ'_w	σ'/σ'_w	ΔK	Initiation type	Shape
9	450	3,02E+05	315	75,8	50*	Ca-S-Al-O-Mg-Si	-1,25	444	307	1,44	8,9	cracked	globular
11	450	9,16E+05	323	38,0	25*	Ca-S-Al-O-Mg-Si	-1,77	447	370	1,21	6,4	non-cracked	globular
19	400	7,81E+05	316	87,2	50*	Ca-S-Al-O-Mg-Si	-1,29	395	302	1,31	8,5	non-cracked	globular
25	400	1,58E+06	314	66,3	0	Ca-S-Al-O-Mg-Si	-3,00	400	369	1,08	7,5	cracked	irregular
29	450	6,13E+05	315	52,4	0	Ca-S-Al-O-Si	-2,60	450	374	1,20	7,5	cracked	globular
30	425	9,50E+05	313	60,3	40	Ca-Al-O	-1,46	420	360	1,17	5,8	cracked	irregular

A2

Specimen no	σ	N_f	HV	$\sqrt{\text{area}}$	h	Composition	R	σ'	σ'_w	σ'/σ'_w	ΔK	Initiation type	Shape
4	450	1,00E+06	343	28,5	20*	Ca-S-Al-O-Si	-1,90	450	436	1,03	5,5	non-cracked	globular
5	425	1,90E+06	344	186,6	200	Ca-S-Al-O-Mg-Si	-1,27	402	313	1,29	9,7	cracked	globular
8	450	3,01E+05	291	80,8	0	Ca-S-Al-O	-2,60	450	328	1,37	9,3	cracked	globular
9	425	9,40E+05	285	124,2	100	Ca-S-Al-O-Mg-Si	-1,27	414	292	1,42	8,2	cracked	globular
11	425	1,49E+06	316	55,9	0	detached	-2,78	425	375	1,13	7,3	non-cracked	globular
16	450	2,32E+05	316	111,7	0	detached	-2,60	450	331	1,36	11,0	non-cracked	globular
17	425	7,37E+05	299	22,7	20*	Al-O	-1,98	425	413	1,03	4,6	non-cracked	al2o3
18	400	3,91E+05	284	131,0	0	Ca-S-Al-O-Mg	-3,00	400	306	1,31	10,6	non-cracked	globular
22	450	2,86E+05	311	104,9	100	Ca-S-Al-O-Si	-1,25	438	319	1,37	8,0	cracked	globular
24	450	4,66E+05	337	28,8	25*	Ca-S-Al-O-Si	-2,60	450	429	1,05	5,6	cracked	globular
25	425	8,31E+05	287	35,4	0	Ca-S-Al-O-Mg-Si	-2,78	425	378	1,12	5,8	cracked	globular
27	425	7,25E+05	324	78,2	60	Ca-S-Al-O-Mg-Si	-1,27	418	346	1,21	6,6	cracked	globular

A3

Specimen no	σ	N_f	HV	$\sqrt{\text{area}}$	h	Composition	R	σ'	σ'_w	σ'/σ'_w	ΔK	Initiation type	Shape
2	400	2,00E+06	335	30,5	25*	Ca-S-Al-O-Mg-Si-C	-1,91	397	400	0,99	5,1	cracked	irregular
3	375	5,67E+05	299	166,9	0	detached	-3,29	375	310	1,21	11,2	non-cracked	globular
11	425	1,15E+06	307	66,2	0	detached	-2,78	425	357	1,19	8,0	non-cracked	globular
13	425	5,21E+05	297	62,8	50	Ca-S-Al-O	-1,27	419	337	1,24	5,9	cracked	globular
15	375	8,93E+05	339	97,3	60*	detached	-1,31	369	313	1,18	8,4	non-cracked	globular
19	425	4,20E+05	297	61,9	0	Ca-S-Al-O-Mg	-2,78	425	353	1,20	7,7	cracked	globular
20	400	2,71E+05	270	104,7	0	detached	-3,00	400	306	1,31	9,4	non-cracked	globular
21	375	3,93E+05	283	131,7	0	Ca-S-Al-O-Mg-Si	-3,29	375	310	1,21	9,9	cracked	globular
26	400	2,22E+06	303	43,0	20*	Ca-S-Al-O-Mg-Si-C	-2,08	398	356	1,12	4,6	cracked	irregular
29	425	4,02E+05	343	278,2	300	Ca-S-Al-O-Mg-Si	-1,27	391	292	1,34	11,6	cracked	globular
30	400	1,76E+06	273	198,1	350	Ca-S-Al-O-Mg	-1,29	363	262	1,38	9,1	cracked	globular

A4

Specimen no	σ	N_f	HV	$\sqrt{\text{area}}$	h	Composition	R	σ'	σ'_w	σ'/σ'_w	ΔK	Initiation type	Shape
2	450	3,02E+05	267	87,8	0	Ca-S-Al-O	-2,60	450	304	1,48	9,7	cracked	globular
4	450	9,16E+05	268	45,6	0	Ca-S-Al-O-Mg	-2,60	450	340	1,32	7,0	cracked	globular
11	400	7,81E+05	323	22,8	10*	Ca-S-Al-O-Si-C	-2,48	399	428	0,93	4,4	cracked	globular
12	400	1,58E+06	282	52,9	30*	Ca-S-Al-O	-1,76	397	318	1,25	6,6	non-cracked	globular
21	450	6,13E+05	266	39,9	0	detached	-2,60	450	347	1,30	6,6	non-cracked	globular

A5

Specimen no	σ	N_f	HV	$\sqrt{\text{area}}$	h	Composition	R	σ'	σ'_w	σ'/σ'_w	ΔK	Initiation type	Shape
1	450	3,02E+05	270	60,0	30*	Ca-S-Al-O-Mg-Si	-1,65	446	298	1,50	8,0	cracked	globular
4	450	9,16E+05	303	28,9	10*	Ca-S-Al-O-Mg-Si	-2,21	449	385	1,17	5,6	cracked	globular
12	400	7,81E+05	274	26,5	20*	Ca-S-Al-O-Mg-Si	-2,08	398	359	1,11	4,7	non-cracked	globular
14	400	1,58E+06	346	69,8	50	Ca-S-Al-O-Mg-Si	-1,29	395	371	1,06	5,8	cracked	globular
23	450	6,13E+05	331	57,7	0	Ca-S-Al-O-Mg-Si	-2,60	450	382	1,18	7,9	cracked	globular

A6

Specimen no	σ	N_f	HV	$\sqrt{\text{area}}$	h	Composition	R	σ'	σ'_w	σ'/σ'_w	ΔK	Initiation type	Shape
2	450	1,00E+06	287	85,5	50*	Ca-S-Al-O-Mg-Si	-1,25	444	282	1,57	9,5	non-cracked	globular
3	425	1,90E+06	315	79,9	70	detached	-1,27	417	338	1,24	6,6	non-cracked	globular
4	450	3,01E+05	299	118,3	50*	Ca-S-Al-O-Mg-Si	-1,25	444	275	1,62	11,1	cracked	globular
5	425	9,40E+05	266	122,7	75*	Ca-S-Al-O-Mg-Si	-1,27	417	252	1,65	10,6	cracked	globular
10	425	1,49E+06	275	89,6	75	detached	-1,27	417	300	1,39	7,0	non-cracked	globular
11	450	2,32E+05	268	62,7	75	detached	-1,25	441	312	1,41	6,2	non-cracked	globular
12	425	7,37E+05	256	91,7	75	Ca-S-Al-O-Mg-Si	-1,27	417	285	1,46	7,1	cracked	globular
16	400	3,91E+05	323	116,9	80	Ca-S-Al-O-Mg	-1,29	391	324	1,21	7,5	cracked	irregular
17	450	2,86E+05	271	200,3	120	Ca-S-Al-O-Mg-Si	-1,25	436	260	1,68	10,9	non-cracked	globular
19	450	4,66E+05	300	122,2	0	detached	-2,60	450	313	1,44	11,5	non-cracked	globular
22	425	8,31E+05	338	138,1	75*	Ca-S-Al-O-Si	-1,27	417	293	1,42	11,3	non-cracked	globular
25	425	7,25E+05	304	107,4	60*	Ca-S-Al-O-Mg-Si	-1,27	418	283	1,48	10,0	cracked	globular

A7

Specimen no	σ	N_f	HV	$\sqrt{\text{area}}$	h	Composition	R	σ'	σ'_w	σ'/σ'_w	ΔK	Initiation type	Shape
1	425	2,66E+05	291	112,3	60*	Ca-S-Al-O-Si	-1,27	418	272	1,54	10,2	non-cracked	globular
1'	425	4,02E+06	299	39,2	20*	Ca-S-Al-O	-1,98	423	355	1,19	6,1	non-cracked	globular
5'	425	1,28E+06	304	103,6	200	Ca-S-Al-O-Mg-Si	-1,27	402	315	1,28	7,3	non-cracked	globular
6	450	5,36E+05	289	33,0	15*	Ca-S-Al-O-Mg-Si	-2,05	448	359	1,25	5,9	cracked	globular
6'	400	1,24E+06	308	70,2	50*	Ca-S-Al-O-Mg-Si	-1,29	395	307	1,28	7,6	cracked	globular
9'	425	1,01E+06	286	61,6	30*	Ca-S-Al-O-Mg-Si	-1,70	422	311	1,36	7,6	non-cracked	globular
10	400	1,07E+06	298	58,2	0	Ca-S-Al-O-Mg-Si	-3,00	400	363	1,10	7,0	non-cracked	globular
12	400	1,42E+06	341	65,4	0	Ca-S-Al-O-Mg-Si	-3,00	400	393	1,02	7,5	non-cracked	globular
13'	425	2,60E+05	280	54,3	20*	Ca-S-Al-O-Mg-Si	-1,98	423	321	1,32	7,2	cracked	irregular
14'	400	2,15E+05	310	269,1	250	Ca-S-Al-O-Mg-Si	-1,29	373	273	1,37	10,9	non-cracked	globular

A8

Specimen no	σ	N_f	HV	$\sqrt{\text{area}}$	h	Composition	R	σ'	σ'_w	σ'/σ'_w	ΔK	Initiation type	Shape
10	475	3,00E+05	255	23,5	0	detached	-2,45	475	363	1,31	5,3	non-cracked	globular
16	475	3,36E+05	302	35,7	0	Ca-S-Al-O-Mg-Si	-2,45	475	383	1,24	6,5	cracked	globular
24	450	1,56E+05	293	61,7	0	detached	-2,60	450	345	1,30	8,1	non-cracked	globular

A9

Specimen no	σ	N_f	HV	$\sqrt{\text{area}}$	h	Composition	R	σ'	σ'_w	σ'/σ'_w	ΔK	Initiation type	Shape
3	425	9,65E+05	307	53,9	30*	detached	-1,70	422	335	1,26	7,1	non-cracked	globular
7	425	7,11E+05	321	150,5	120	Ca-S-Al-O-Mg-Si	-1,27	411	308	1,34	8,9	cracked	globular
17	425	3,80E+05	306	77,4	50	Ca-S-Al-O-Si	-1,27	419	333	1,26	6,5	cracked	globular
24	450	3,00E+05	309	31,6	20*	Ca-S-Al-O-Mg-Si	-1,90	448	374	1,20	5,8	cracked	globular

A10

Specimen no	σ	N_f	HV	$\sqrt{\text{area}}$	h	Composition	R	σ'	σ'_w	σ'/σ'_w	ΔK	Initiation type	Shape
2	400	4,66E+05	281	133,7	0	detached	-3,00	400	303	1,32	10,7	non-cracked	globular
6	400	5,33E+05	300	126,5	0	Ca-S-Al-O-Mg-Si	-3,00	400	320	1,25	10,4	cracked	globular
8	400	1,24E+06	311	94,0	50*	Ca-S-Al-O-Mg-Si	-1,29	395	295	1,34	8,8	non-cracked	globular
11	425	2,45E+05	334	179,8	0	detached	-2,78	425	322	1,32	13,1	non-cracked	globular
12	400	4,35E+05	311	111,9	0	Ca-S-Al-O-Mg-Si	-3,00	400	335	1,19	9,8	non-cracked	globular
15	425	3,00E+06	320	121,2	200	Ca-S-Al-O-Mg-Si	-1,27	402	319	1,26	7,9	non-cracked	globular
19	425	2,14E+06	313	41,5	0	detached	-2,78	425	392	1,08	6,3	non-cracked	globular
20	400	8,50E+05	302	125,1	75*	Ca-S-Al-O-Mg-Si	-1,29	392	276	1,42	10,1	non-cracked	globular
22	400	3,82E+06	310	176,5	350	Ca-S-Al-O-Mg-Si	-1,29	363	293	1,24	8,5	cracked	globular
25	425	3,27E+05	253	72,5	50	Ca-S-Al-O-Mg-Si	-1,27	419	294	1,42	6,3	cracked	globular

A11

Specimen no	σ	N_f	HV	$\sqrt{\text{area}}$	h	Composition	R	σ'	σ'_w	σ'/σ'_w	ΔK	Initiation type	Shape
2	450	6,11E+05	256	44,9	0	Ca-S-Al-O-Mg-Si	-2,60	450	330	1,36	6,9	cracked	globular
3	425	7,45E+05	290	39,9	25*	Ca-S-Al-O-Mg-Si	-1,83	422	342	1,24	6,1	non-cracked	globular
6	450	3,23E+05	314	45,6	0	Ca-S-Al-O-Si	-2,60	450	382	1,18	7,0	non-cracked	globular
7	425	4,05E+05	261	37,6	0	Ca-S-Al-O-Mg-Si	-2,78	425	349	1,22	6,0	non-cracked	globular
9	425	3,51E+06	294	55,8	0	Ca-S-Al-O-Mg-Si	-2,78	425	357	1,19	7,3	cracked	globular
11	425	1,01E+06	278	34,6	0	Ca-S-Al-O-Mg-Si	-2,78	425	370	1,15	5,8	cracked	globular
13	425	6,40E+05	281	35,1	0	Ca-S-Al-O-Si	-2,78	425	373	1,14	5,8	non-cracked	globular
14	400	1,35E+06	279	31,7	0	Ca-S-Al-O-Si	-3,00	400	383	1,05	5,2	non-cracked	globular
16	400	1,18E+06	274	27,4	15*	Ca-S-Al-O-Mg-Si	-2,27	398	362	1,10	4,8	non-cracked	globular
17	375	2,13E+06	292	82,9	70	Ca-S-Al-O-Si	-1,31	368	320	1,15	5,9	non-cracked	globular
20	400	6,94E+05	323	101,3	0	Ca-S-Al-O-Si	-3,00	400	351	1,14	9,3	non-cracked	globular
23	425	6,97E+05	314	51,3	20*	Ca-S-Al-O-Mg	-1,98	423	352	1,20	7,0	cracked	irregular
26	400	4,72E+06	296	144,4	160	Ca-S-Al-O-Mg	-1,29	383	293	1,31	8,2	non-cracked	globular
30	425	6,33E+05	275	36,9	0	Ca-S-Al-O-Mg-Si	-2,78	425	364	1,17	5,9	non-cracked	globular

A12

Specimen no	σ	N_f	HV	$\sqrt{\text{area}}$	h	Composition	R	σ'	σ'_w	σ'/σ'_w	ΔK	Initiation type	Shape
15	475	1,43E+05	329	71,6	0	Al-O-Ca-S-Mg-Si	-2,45	466	363	1,28	9,1	cracked	globular
18	450	8,35E+05	296	13,7	5*	Al-O	-2,40	448	434	1,03	3,8	non-cracked	al2o3

A13

Specimen no	σ	N_f	HV	$\sqrt{\text{area}}$	h	Composition	R	σ'	σ'_w	σ'/σ'_w	ΔK	Initiation type	Shape
6	450	3,25E+05	283	47,6	0	detached	-2,60	450	351	1,28	7,2	non-cracked	globular
7	425	2,60E+05	306	71,6	60	Al-O-Ca-S	-1,27	418	337	1,24	6,3	cracked	irregular
11	425	2,98E+05	264	31,0	0	Al-O-Ca-S	-2,78	425	364	1,17	5,5	cracked	globular
21	425	3,52E+05	280	42,9	0	Ca-S-Al-O	-2,78	425	359	1,18	6,4	non-cracked	globular
24	450	1,69E+06	310	33,5	20*	Al-O-Ca-S	-1,91	448	372	1,20	6,0	non-cracked	globular

A14

Specimen no	σ	N_f	HV	$\sqrt{\text{area}}$	h	Composition	R	σ'	σ'_w	σ'/σ'_w	ΔK	Initiation type	Shape
3	425	6,47E+05	322	35,7	20*	Ca-S-Al-O-Mg-Si	-1,98	423	381	1,11	5,8	cracked	globular
5	425	1,34E+06	301	43,6	0	Ca-S-Al-O-Mg	-2,78	425	378	1,13	6,5	cracked	globular
8	450	6,03E+05	330	21,4	15*	Ca-S-Al-O-Mg-Si	-2,05	448	425	1,05	4,8	non-cracked	globular
11	425	3,93E+05	305	115,1	60*	Ca-S-Al-O-Mg-Si	-1,27	418	281	1,49	10,3	cracked	globular
14	450	1,98E+05	265	30,4	0	Ca-S-Al-O-Mg-Si	-2,60	450	362	1,24	5,7	cracked	globular
19	475	3,31E+05	296	67,6	0	Ca-S-Al-O-Mg-Si	-2,45	475	339	1,40	9,0	cracked	globular
20	450	3,17E+05	322	65,9	60	Ca-S-Al-O-Mg-Si	-1,25	443	354	1,25	6,4	cracked	globular
21	425	8,85E+05	356	55,3	40*	Ca-S-Al-O-Mg	-1,46	420	363	1,16	7,2	cracked	irregular
23	425	2,58E+05	308	126,6	0	Ca-S-Al-O-Mg	-2,78	425	322	1,32	11,0	cracked	globular
25	425	7,79E+05	356	21,4	30	Al-O	-1,70	422	482	0,87	3,5	non-cracked	al2o3

A15

Specimen no	σ	N_f	HV	$\sqrt{\text{area}}$	h	Composition	R	σ'	σ'_w	σ'/σ'_w	ΔK	Initiation type	Shape
4	450	2,51E+05	285	43,6	25*	Ca-S-Al-O-Mg-Si	-1,77	447	331	1,35	6,8	cracked	globular
10	400	8,97E+05	287	40,4	0	detached	-3,00	400	375	1,07	5,9	non-cracked	globular
14	450	3,46E+05	296	55,0	0	detached	-2,60	450	354	1,27	7,7	non-cracked	globular
15	425	2,30E+06	342	82,1	0	Ca-S-Al-O-Mg	-2,78	425	374	1,14	8,9	non-cracked	globular
17	425	3,78E+05	304	64,4	0	Ca-S-Al-O-Si	-2,78	425	356	1,19	7,9	cracked	globular
19	425	7,39E+05	276	51,3	75	Ca-Al-O-Si	-1,27	417	331	1,26	5,3	cracked	globular
22	450	5,70E+05	300	86,7	0	Ca-S-Al-O-Mg-Si	-2,60	450	332	1,36	9,7	cracked	globular
27	425	1,25E+06	280	48,6	0	Ca-S-Al-O	-2,78	425	352	1,21	6,8	cracked	globular

A16

Specimen no	σ	N_f	HV	$\sqrt{\text{area}}$	h	Composition	R	σ'	σ'_w	σ'/σ'_w	ΔK	Initiation type	Shape
22	450	4,79E+05	307	52,8	15*	Ca-S-Al-O	-2,05	448	346	1,29	7,5	non-cracked	globular
27	425	8,80E+05	291	20,8	0	Ca-S-Al-O	-2,78	425	416	1,02	4,5	cracked	globular

A17

Specimen no	σ	N_f	HV	$\sqrt{\text{area}}$	h	Composition	R	σ'	σ'_w	σ'/σ'_w	ΔK	Initiation type	Shape
4	475	3,00E+05	277	26,4	0	Ca-S-Al-O	-2,45	475	378	1,26	5,6	non-cracked	globular
7	450	5,28E+05	275	22,1	15*	detached	-2,05	448	332	1,35	4,9	non-cracked	globular
12	475	3,36E+05	301	53,9	0	Ca-S-Al-O	-2,45	475	356	1,33	8,0	non-cracked	globular
13	450	1,56E+05	322	161,1	100*	Ca-S-Al-O-Si	-1,25	438	275	1,59	12,8	non-cracked	globular
15	450	2,39E+06	336	19,3	20	detached	-1,90	448	438	1,02	3,5	non-cracked	globular

A18

Specimen no	σ	N_f	HV	$\sqrt{\text{area}}$	h	Composition	R	σ'	σ'_w	σ'/σ'_w	ΔK	Initiation type	Shape
14	450	5,20E+05	291	24,5	15*	Ca-S-Al-O	-2,05	448	378	1,18	5,1	non-cracked	globular
18	450	5,20E+05	280	19,9	10*	Ca-S-Al-O	-2,21	449	386	1,16	4,6	cracked	globular

B1

Specimen no	σ	N_f	HV	$\sqrt{\text{area}}$	h	Composition	R	σ'	σ'_w	σ'/σ'_w	ΔK	Initiation type	Shape
2	450	6,71E+05	313	104,1	120	Ca-S-Al-O-Mg-Si	-1,25	436	321	1,36	7,9	cracked	globular
4	450	3,57E+05	356	106,1	0	Ca-S-Al-O-Mg	-2,60	450	365	1,18	10,7	cracked	globular
9	475	4,71E+05	344	38,6	0	Ca-S-Al-O-Si	-2,45	475	416	1,12	6,8	cracked	globular

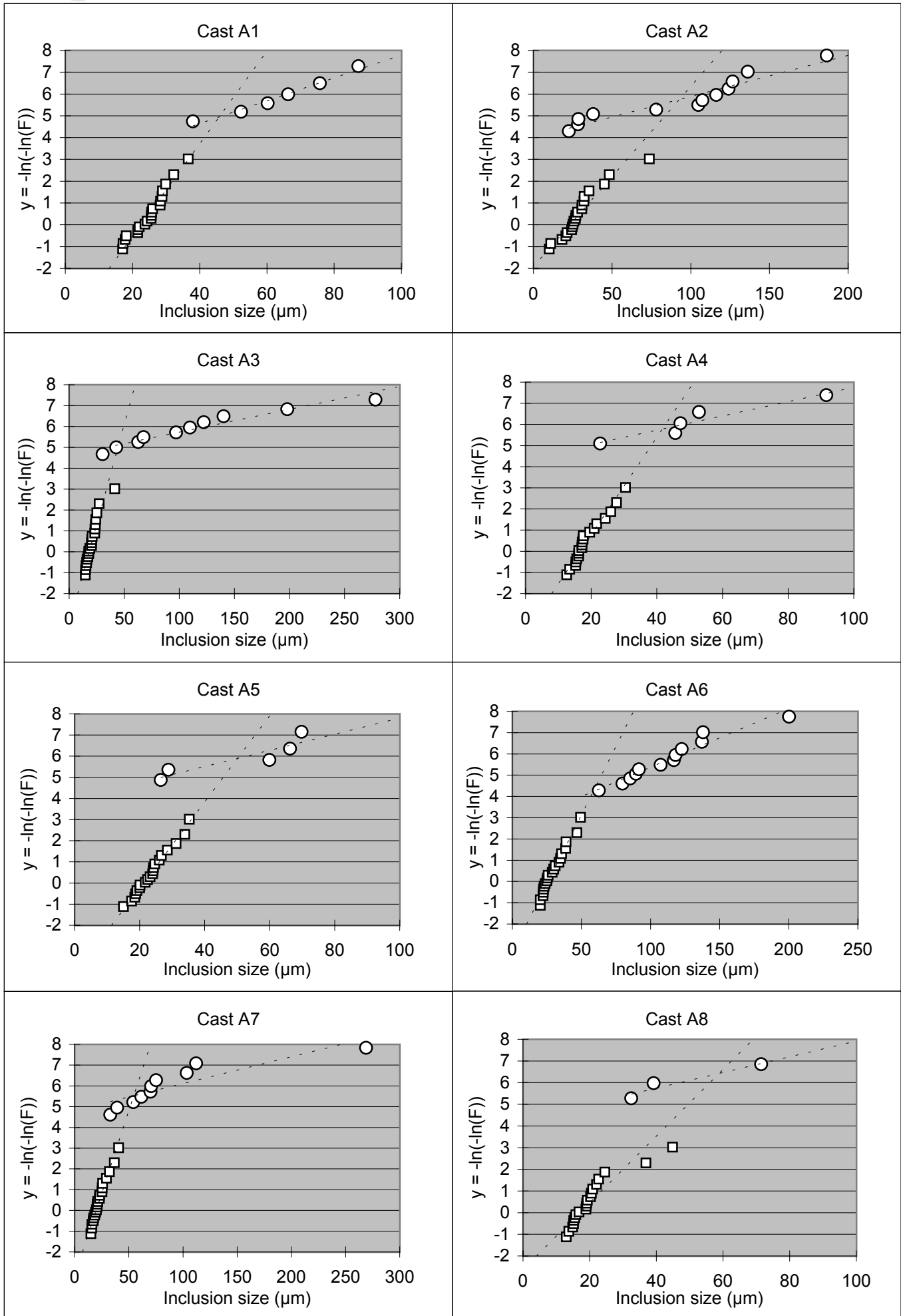
B2

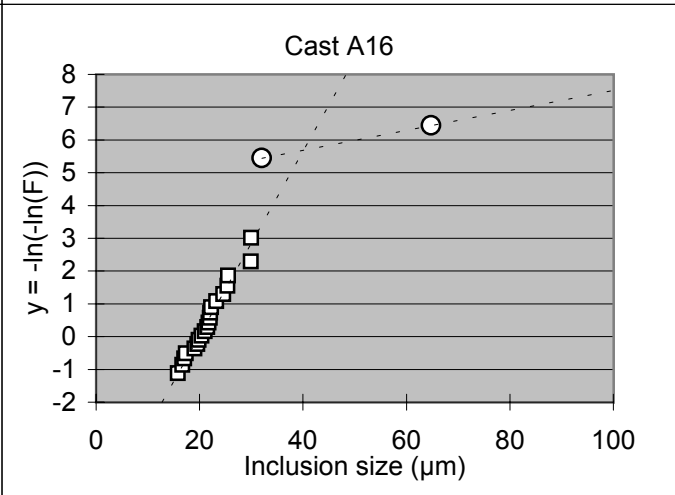
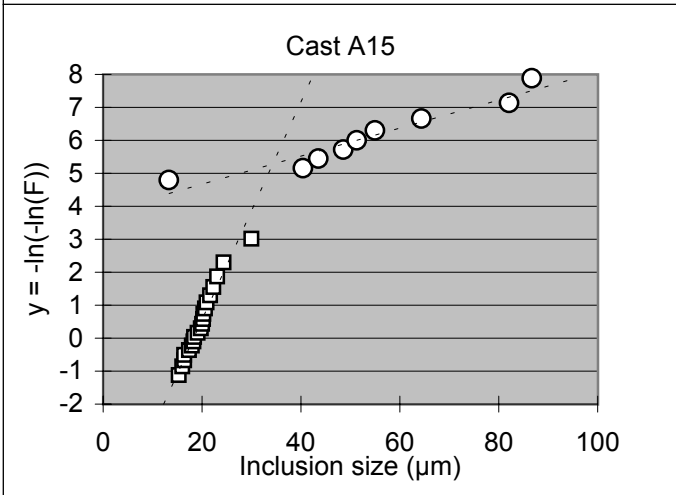
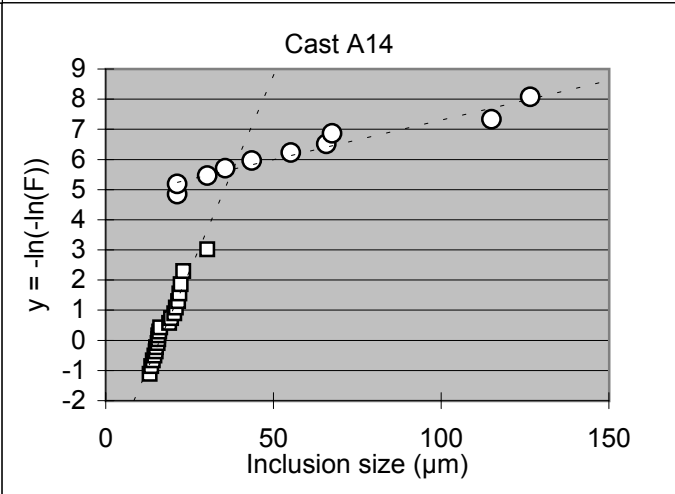
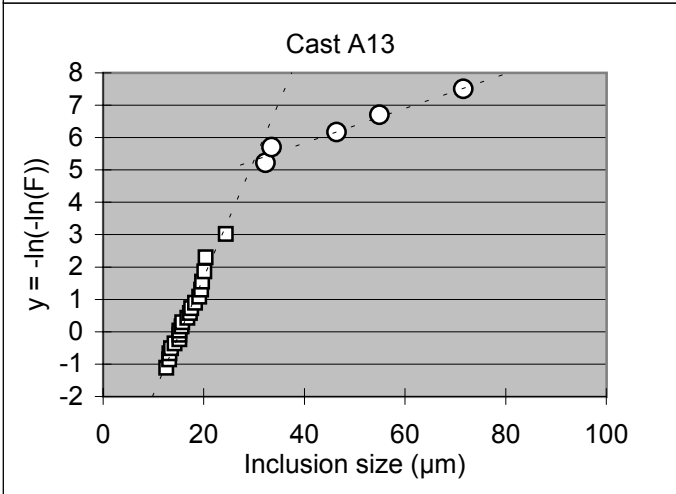
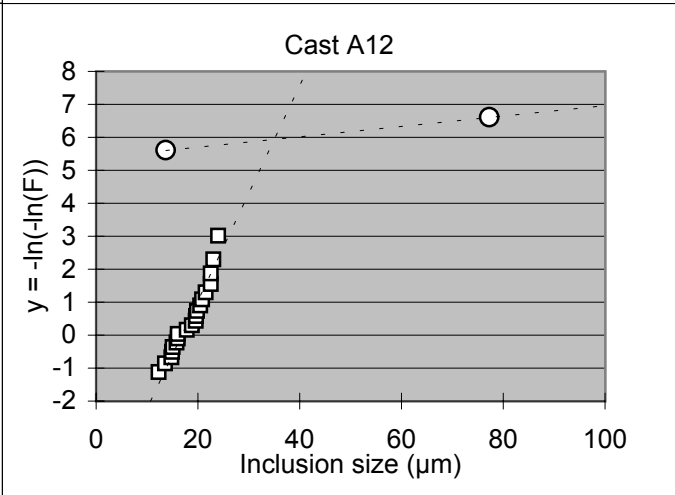
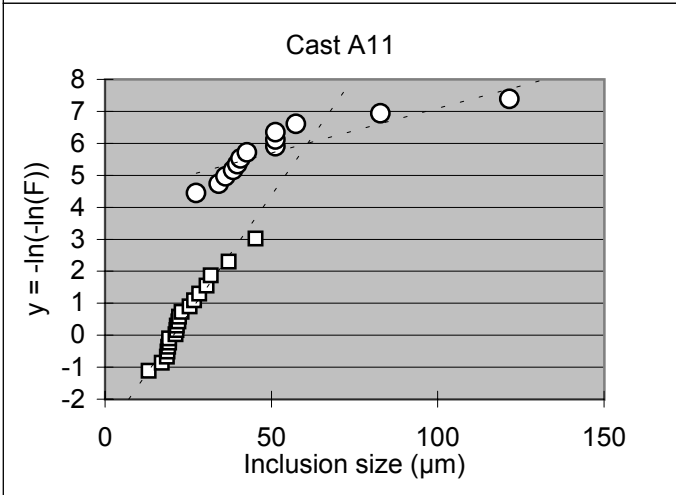
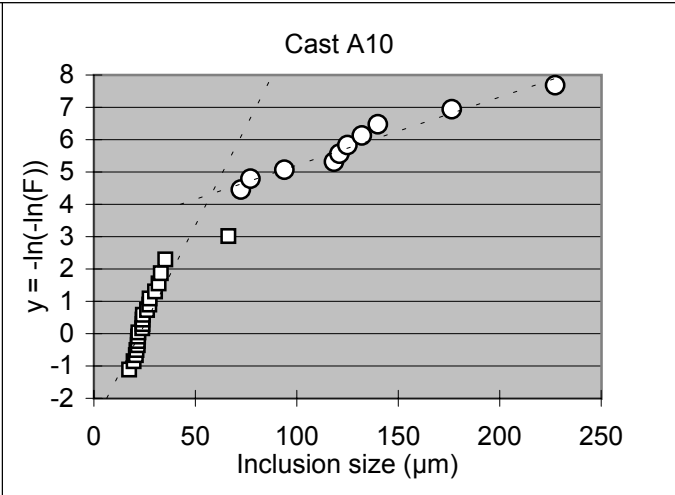
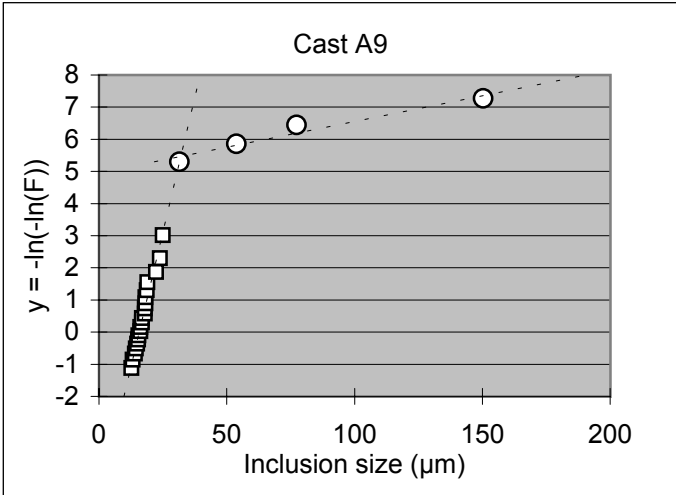
Specimen no	σ	N_f	HV	$\sqrt{\text{area}}$	h	Composition	R	σ'	σ'_w	σ'/σ'_w	ΔK	Initiation type	Shape
2	475	3,00E+05	334	110,0	0	detached	-2,45	475	342	1,39	11,5	non-cracked	globular
4	475	3,36E+05	291	62,4	0	detached	-2,45	475	339	1,40	8,6	non-cracked	globular

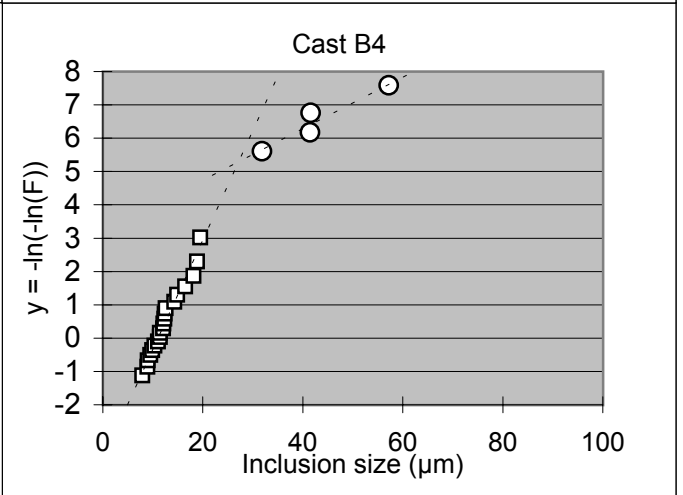
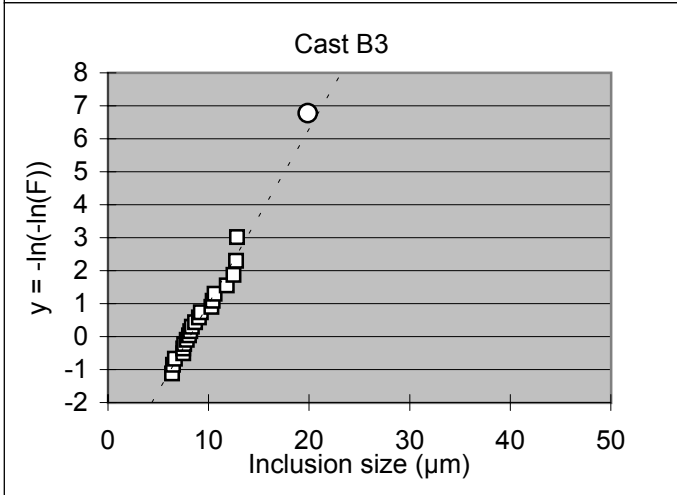
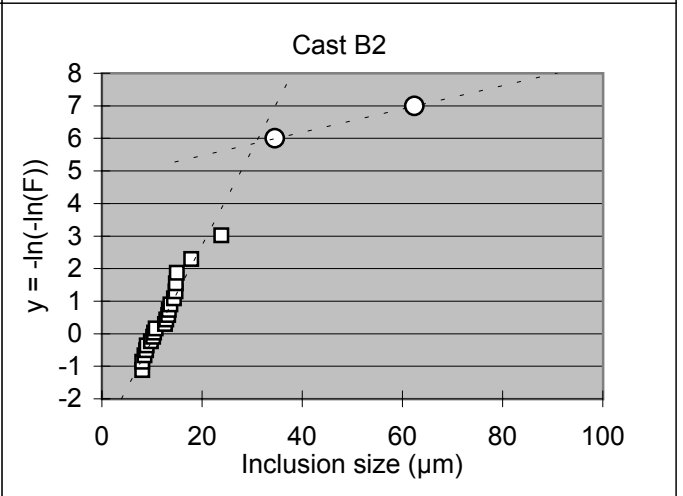
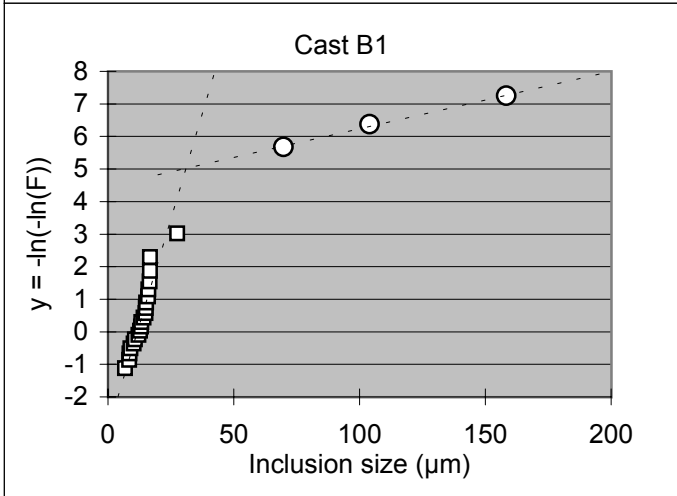
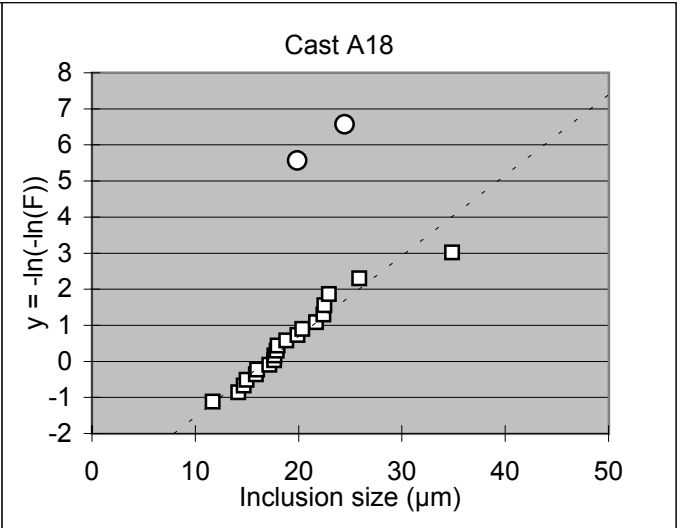
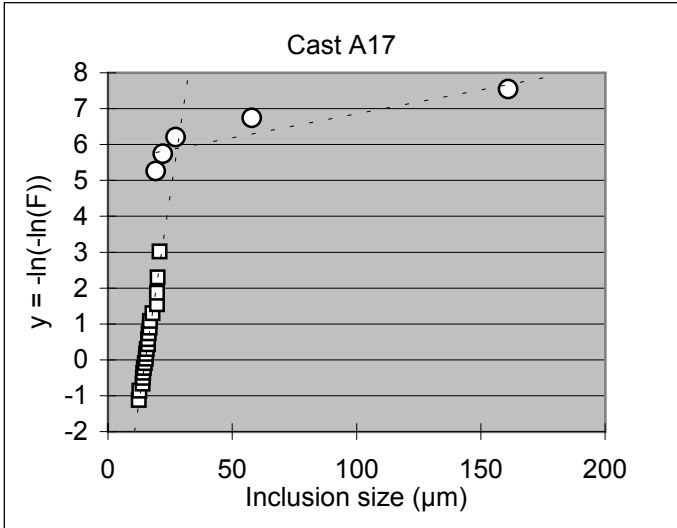
B4

Specimen no	σ	N_f	HV	$\sqrt{\text{area}}$	h	Composition	R	σ'	σ'_w	σ'/σ'_w	ΔK	Initiation type	Shape
4	400	7,85E+05	313	57,2	40*	Ca-S-Al-O-Si-C	-1,50	396	329	1,20	6,9	cracked	globular
10	450	5,63E+06	358	41,5	30	Ca-S-Al-O-Si-C	-1,65	446	431	1,04	5,1	non-cracked	globular
22	450	3,56E+05	283	41,6	40	Ca-S-Al-O-Si-C	-1,43	445	355	1,25	5,1	cracked	globular
26	450	5,24E+05	271	29,0	0	Ca-S-Al-O-Mg	-2,60	450	370	1,22	5,6	cracked	globular

- Inclusions at fatigue crack initiation sites
- Inclusions at microsections







APPENDIX 4. Lower and upper bound estimates of the fatigue strength

- Initiation from surface inclusion
- ⊙ Initiation from inclusion under the surface, i.e., fish-eye fracture
- ✕ Initiation from a surface crack
- Ran out

